Thermo-Osmosis:
Theory and Simulations

Thermo-Osmosis:

Theory and Simulations

A thesis submitted to
Università degli Studi dell'Insubria
in partial fulfilment of the requirements
for the degree of *Philosophiæ Doctor*

by

Zeno Filiberti

Supervisor
Alberto Parola
Full Professor of Physics

December 2020

Contents

1 Introduction

We are used to associate the motion of a fluid placed in a temperature gradient to the convection phenomenon. Here the driving force is an external field, the gravity, while the role of temperature is simply to modify the density of the fluid along the direction of the gradient. Nevertheless, nature is characterized by phenomena where a non-uniform thermal profile can by itself set a fluid in motion, that is where the temperature gradient behaves like an effective force. The first observation of such a phenomenon was reported independently by Ludwig [52], Soret [75, 76, 77] and Fedderesen [26] in the second half of the Nineteenth century. What they osberved is that when a binary mixture is placed in a temperaure gradient, an unbalanced migration of the two species takes place. This phenomenon is known as Ludwig-Soret effect or *thermodiffusion*[1]. In his work of the 1873 Feddersen reported also the first observation of another phenomenon where the temperature gradient behaves like a force: He measured the motion of gases towards the hot side of a tube filled with porous plugs of gypsum or spongy platinum. This phenomenon was named by Lippman [49] as *thermo-osmosis*[2], and it is the stationary mass flow wich develops in a one-component gaseous or liquid system placed in a temperature gradient. Actually, the onset of this flow requires also the presence of a confining surface not perpendicular to the temperature gradient. Indeed

[1] In the same years Dufour [19, 20] observed also the reciprocal effect of thermodiffusion in a mixture of air and hydrogen: A gradient in particles concentration induces a temperature gradient.

[2] In gaseous systems it is known also as thermal creep.

when the fluid placed in the thermal gradient is homogeneous (a bulk fluid), the force balance condition implies mechanical equilibrium, thus the pressure is constant throughout the system. It follows that, in absence of external forces, in the stationary state the fluid is characterized by a space dependent density, a constant heat flux, but not by a mass current. Another phenomenon called *thermophoresis* was discovered in the same years by Tyndall [79]: He observed that dust particles suspended in air are repelled by hot surfaces. Thus, thermophoresis can be defined as the motion induced by a temperature gradient of mesoscopic particles placed in a fluid. This phenomenon is for sure interesting from a technological point of view and it is believed that interfaces play a key role in its onset: When a particle lies in a fluid placed in a temperature gradient, the particle surface induces the motion of the fluid alongside. Due to this flow the particle is subject to a net force and, consequently it drifts.

This brief historical summary highlights the important role that temperature gradients can play in fluid and soft matter systems. Moreover, it is clear that such nonequilibrium phenomena have been known for a long time, but a comprehensive understanding of them is still lacking today. For example, particles thermophoresis in gaseous systems is rather well understood by means of the kinetic theory[3], and in general the particle drift is directed towards the cold side of the system. Instead, when denser fluids are considered, our understanding becomes poorer. Different theoretical models have been developed in order to clarify thermophoresis in liquid systems and the basic strategy is to describe the effect of the thermal gradient as an effective force $\boldsymbol{f}$ acting on the particle. At the stationary state the effective force $\boldsymbol{f}$ is balanced by the frictional one, thus the total force acting in the particle vanishes. Unfortunately these theories are not able to explain features such as the fact that the drift velocity magnitude and direction strongly depend on the surface properties of the particles, but also on external parameters, such as the average temperature of the fluid. Recent reviews [63, 64, 83] deeply deal with this arguments.

Despite the lack of a general satisfactory theory of thermophoresis, it is now clear the crucial role played by the particle-fluid interface and thus the deep link with the less-famous thermo-osmosis phenomenon: The particle motion is due to the thermo-osmotic mass flow that the surface of the particle itself induces in the sorrounding fluid. Therefore thermo-osmosis is the basic mechanism responsible for thermophoresis. Moreover, in the last few years the phenomenon of thermo-osmosis has motivated the interest of Fu *et al.* [29, 30], Frenkel *et al.* [32, 33, 67], Bregulla *et al.* [9] and Farago [25], because, as it will be explained in the following, also this fundamental nonequilibrium effect is characterized by the lack of a satisfactory characterization and theoretical interpretation, especially in the liquid systems. This renewed interest is justified

[3] A review about this topic can be found in [84].

also by possible applications of thermo-osmosis to fuel cells, water recovery and water management [48], but also in desalination of seawater and in power generation from the salinity difference with river water [51]. Being an interface phenomenon, it is interesting (together with thermophoresis) also in nano systems: It could be employed for particle motion and manipulation through hot nanostructures [14]. Furthermore, eukaryotic cells are characterized by large temperature gradients in their structure, thus thermo-osmosis could play a role also in this kind of living systems [12].
These reasons induced us to tackle the problem of thermo-omsosis, both from a theoretical and a numerical point of view and the main results achieved by us are presented in this work. In the remaining of this Chapter we will present the state of the art of the knowledge of thermo-osmosis, reporting the most important results related to rarefied and dense systems. In Chapter 2 our theoretical description of this phenomenon will be discussed. It is an exact microscopic theory, based on linear response theory, generalized to inhomogeneous systems and it shows that this effect originates from two independent physical mechanisms. It provides a unified description of thermo-osmosis and reduces to known expressions in the appropriate density limits. This microscopic approach resolves also a relevant question related to the non unicity of the microscopic pressure tensor. This point will be tackled also from a numerical point of view in Chapter 3, together with the problem in the definition of transport coefficients in two-dimensional fluid systems. In Chapter 4 a large number of nonequilibrium molecular dynamics simulations will be presented. The considered systems are Lennard-Jones two-dimensional confined fluids placed in a non-uniform temperature profile. The purpose of this numerical study is the direct "observation" of the thermo-osmotic mass flow and the evaluation of the relative importance of the two mechanisms underlying this phenomenon in different conditions of both confinements and thermodynamic state of the fluid. Moreover, also the asymptotic behavior of large channels predicted in Chapter 2 will be here numericaly studied.

1.1 STATE OF THE ART

The first observation of thermo-osmosis was performed by Feddersen [26] in gaseous systems and dates back to 1873. The same phenomenon was later observed also in liquids, but in these systems the magnitude of the effect is much smaller than in gases. Probably for this reason, thermo-osmosis was initially studied both theoretically and experimentally only in the rarefied regime and a good grade of understanding was achieved. Instead, the interest on the dense regime arised only in the second half of the Twentieth century and a less satisfactory understanding was obtained. Moreover, also the theoretical tools adopted in the description of this phenomenon in the two density regimes are complitely differents. Thus, following this historical and methodological discrepancy, we will separately review the the main results regarding thermo-

osmosis in gases and in liquids.

1.1.1 Thermo-osmosis in Gases

After the first observations by Feddersen, a strong interest in thermo-osmosis arised due to the invention of the radiometer by Crookes [13] in 1876. The radiometer consist of a glass vial within which a (nearly) vacuum condition is reached. In this environment kept at low pressure a fan is placed on a spike. Each blade of this fan is shiny on one side and blackened on the other, in fact Crookes devised this object in order to detect the pressure of light. When he submitted its work to the Royal Society also the referee, which was Maxwell, agreed with Crookes's interpretation of the phenomenon: The motion of the fan was induced by the the light impinging on the blades. Despite the convictions of Crookes and Maxwell, the origin of the blades motion could not be the radiation pressure, because the the fan rotation was in the wrong direction. Instead, after the experiments led by Schuster [71] and the observations of Reynolds, it became clear that the rotation took place because of an unbalance of pressure of the gas near the two differently heated sides of each blade. The reason of this pressure difference was not clear and a debate between Maxwell and Reynolds began [10]. The solution of this problem is usually ascribed to Maxwell, who in 1879 showed that tangential stress delevelops in the gas near the confining surfaces to which a temperature gradient is applied [53]. This tangential stress is responsible for the thermal creep of the gas, and thus for the radiometer motion. The surprising aspect is that in the case of the radiometer the tangential stress arises just at the edge of the blame, being this the surface to which a temperature gradient is applied. The phenomenon of thermo-osmosis in gases has been clearly shown by a simple experiment recently devised by Sone and Yoshimoto [74].
Let us now give a pictorial description of Maxwell's interpretation of thermal creep. If we consider a confined gas placed in a temperature gradient we can state that, from a statistical point of view, a particle wich comes from the hotter side carries a greater momentum than a particle coming from the colder one. Now, if the particles collisions against the surface are inelastic, than on average particles coming from the hot side transfer to the surface more momentum than particles coming from the cold one. It follows that there is a net momentum transfer from the gas to the surface towards the cold side and, for the action-reaction principle, the surface applies a net momentum to the gas in the opposite direction, thus the gas is set in motion towards the hot side of the system. Therefore, Maxwell understood the fundamental role of the nature of the particle-surface interaction. He formalized his ideas through the kinetic theory and obtained an expression[4] for the creep velocity for an

[4]See for example also the classic book by Kennard [44].

almost ideal gas[5] far from the surface and in absence of pressure gradients:

$$v_\infty = \frac{3}{4}\frac{\eta}{\rho}\frac{\nabla T}{T}\,, \tag{1.1}$$

being ρ the bulk density and η the shear viscosity of the gas, while ∇T is the temperature gradient aligned to the confining surface. Moreover, this asymptotic relation for the slip velocity can be expressed through the mean free path λ,

$$v_\infty = \frac{3}{\sqrt{8\pi}}\lambda\sqrt{\frac{k_\mathrm{B}T}{m}}\frac{\nabla T}{T}\,, \tag{1.2}$$

where m is the gas particle mass. The mean free path, which has been expressed through the standard relation for a hard spheres gas

$$\lambda = \frac{\eta}{\rho}\sqrt{\frac{\pi}{2mk_\mathrm{B}T}}\,, \tag{1.3}$$

is the only relevant length scale in the thermal creep phenomenon.
To our knowledge, also the first numerical evidence of thermo-osmosis is related to a gaseous system: Papadopoulos and Rosner [62] in 1995 employed the direct simulation Monte Carlo technique in order to study the behavior of a hard spheres gas placed in a temperature gradient and confined in a 2D closed channel. They were interested only in the observation of the effect, because it can play a role in microgravity experiments on crystal growth in ampules, and they were able to achieve this objective. Furthermore their results confirm an important feature of thermal creep, already predicted by Maxwell's theory: Gas is characterized by a slip towards the hot side of the system.

1.1.2 Thermo-osmosis in Liquids

The first observation of thermo-osmosis in liquids dates back to 1907 and was performed by Lippmann [49] separating two volumes of water, kept at different temperatures, through a membrane of gelatine. A more systematic study was carried out a few years later by Aubert [3]: He observed that, depending on the kind of membrane, the water mass flow can be directed towards the hot side of the system or the cold one, or can be even absent. After these seminal works, other scientists in the half of the Twentieth century tried to study experimentally thermo-osmosis in liquid systems[6], but these results cannot be considered satisfactory: The experimental observations often

[5] That is a gas of hard spheres, where collisions between particles are allowed, but they do not interact through a space dependent potential.

[6] See for example the experiments performed by Derjaguin and Sidorenkov [16], Hutchinson *et al.* [41] and Haase and Steinert [35].

disagree about the magnitude and even the direction of thermo-osmotic fluxes. To be more precise, the flow is directed towards the cold side of the system when hydrophobic membranes are involved, while the interpretation on the direction of the flux is less cleare when hydophilic membranes are employed[7]. To our knowledge, the last experimental work concerning thermo-omsosis was published in 2016 [9] and the authors present the first microscale observation of the velocity field induced by thermo-osmosis. The experimental set up consist of a glass slit of about 5μm of thickness and filled with water. At the upper surface of the slit a gold nanoparticle of 250nm of diameter is immobilised. A temperature gradient is generated heating this particle with a laser, and the thermo-osmotic flow is monitored tracking the motion of smaller gold nanoparticles. In this way the authors were able to observe a flow directed towards the hot region and with an extrapolated velocity of about 40μm/s. Beyond the importance of the result, this work testifies also a renewed interest in the experimental study of thermo-osmosis in liquid systems and the capability to perform microscopic measures of this phenomenon.
From a theoretical point of view, the most important result was obtained by Derjaguin and Sidorenkov in 1941. Their work is based on the linear nonequilibrium thermodynamics, mainly developed by Onsager [59]. In order to understand Derjaguin's theory[8], let us consider a planar wall along the x direction. Fixed differences of temperature ΔT and pressure Δp are imposed at the ends of the wall and their gradients result to be directed along x. As a consequence heat J_q and mass J_ρ fluxes develop along the x direction. Thus, we can express the rate of entropy production σ across a surface perpendicular to the direction x as

$$\sigma = J_\rho \Delta p + J_q \frac{\Delta T}{T}\,, \tag{1.4}$$

where the two quantities coupled to the fluxes are defined as thermodynamics forces:

$$\mathcal{X}_\rho = \Delta p\,, \quad \mathcal{X}_q = \frac{\Delta T}{T}\,. \tag{1.5}$$

Linear nonequilibrium thermodynamics assumes that the fluxes are linear functions of these forces, thus

$$\begin{aligned} J_\rho &= L_{\rho\rho}\mathcal{X}_\rho + L_{\rho q}\mathcal{X}_q \\ J_q &= L_{qq}\mathcal{X}_q + L_{q\rho}\mathcal{X}_\rho\,, \end{aligned} \tag{1.6}$$

where $L_{\alpha\beta}$ are phenomenological coefficients and the $\alpha = \beta$ ones are easily interpretable: L_{qq} is the coefficient related to the thermal conductivity, and

[7] It is possible to consult also a recent review about the topic of thermo-osmosis in membranes [5] if more details are needed.
[8] More details can be found in Ref. [16] and [15].

describes the heat conduction at constant pressure, while $L_{\rho\rho}$ is related to the fluid mass flow at constant temperature. The heat and mass fluxes are coupled through the cross coefficients $L_{q\rho}$ and $L_{\rho q}$: $L_{q\rho}$, known as mechanocaloric coefficient, represents the mechanical contribution to the heat flux, while $L_{\rho q}$ has the opposite meaning. Onsager, exploiting the microscopic reversibility of the system, showed that these cross coefficients are equal[9] [59]. Note that, if the fluid is homogeneous, heat and mass currents fluctuate independently, thus the cross coefficients vanish[10].
Derjaguin and Sidorenkov applied this linear nonequilibrium thermodynamics formalism in order to describe thermo-osmosis in liquids. They were interested in the description of this phenomenon in an open channel, that is a system characterized by constant pressure, where therefore

$$\begin{aligned} J_\rho &= L_{\rho q}\mathcal{X}_q \\ J_q &= L_{qq}\mathcal{X}_q \,. \end{aligned} \tag{1.7}$$

Thus, they expressed the mechanocaloric coefficient in terms of the local excess (with respect to the bulk value) enthalpy of the fluid, $\Delta h(z)$. Then, exploiting the expression for J_ρ, they where able to obtain an expression for the liquid velocity far from the surface:

$$v_\infty = \frac{1}{\eta}\int_0^\infty \mathrm{d}z\, \Delta h(z)\frac{\nabla T}{T}\,, \tag{1.8}$$

being η the shear viscosity of a bulk fluid[11]. Two important hypoteses underlie this result. The first one is that the viscosity, which should be space-dependent near the confining wall, can be considered constant and equal to its bulk value everywhere: The effect of a non-uniform viscosity on the fluid motion is disregarded. The second hypotesis is that a local enthalpy in the fluid layers in the proximity of the surface can be defined. Two diffuculties arise in this regard: First of all the local enthalpy is not a slowly varying function, as shown for example in Ref. [29]. It follows that the local equilibrium definition employed by Derjaguin and Sidorenkov is in principle not valid. Moreover, as will be better discussed in Chapters 2 and 3, enthalpy (which is strictly related to pressure) cannot be uniquely defined near a surface. Nevertheless, Derjaguin's picture suggests that thermo-osmosis in liquids is rooted in the anisotropy of the pressure tensor, wich develops on a range of the order of the correlation length.
This phenomenon in liquid systems have been studied also from a numerical point of view, in particular through the molecular dynamics techniques. The first observations of thermo-osmosis in dense fluids were reported to our knowledge by Wold and Hafskjold in 1999 [82] and Galliéro *et al.* [31] three

[9] This result is known as Onsager reciprocal relations.
[10] More details can be found in Ref. [47], Sec. 49 or Ref. [4], Sec. 12.5.
[11] In the following we will refer to η simply as *bulk viscosity*.

years later. Both groups were studying thermodiffusion through molecular dynamics nonequilibrium simulations, i. e. generating a temperature gradient in the system, and the thermo-osmotic mass flow was observed as a side effect, interpreted as a Marangoni effect. The main difference in the two works lays in the choice of the simulation cell. Galliéro *et al.* simulated a cell periodic in the temperature gradient direction. This kind of system introduces as an artifact a recirculating velocity field. Instead, Wold and Hafskjold considered a closed channel, where the observed recirculating velocity field is a direct consequence of the mass conservation principle. Despite these works showed the possibility to investigate thermo-osmosis through nonequilibrium molecular dynamics simulations, the first numerical studies focused on this phenomenon in liquid systems are very recent. The group settled in Lyon performed, in its first work related to thermo-osmosis [29],two kind of simulations in order to obtain the mechanocaloric coefficients in liquids confined by Einstein solids[12] differently hydrophilic. In particular, in the *mechanocaloric route* they applied a body force per particle to a fluid placed in an infinite channel (i. e. with periodic boundary condition in the x direction), in order to model a pressure gradient and they measured the resulting heat flux. In this way they were able to compute the mechanocaloric coefficient as the ratio between the heat flux and the pressure drop. Measuring also the excess enthalpy profile and other parameters they computed the value of $L_{q\rho} = L_{\rho q}$ exploiting the result of Derjaguin. In the *thermo-osmotic route* they connected a slit channel to two reservoirs at the same pressure (imposed by two pistons) and different temperatures and they measured the average thermo-osmotic velocity v_s looking at the time evolution of the number of particles in the two reservoirs. Then they computed $L_{q\rho} = L_{\rho q} = v_s/(-\nabla T/T)$. Also in this nonequilibrium simulations the value of $L_{q\rho} = L_{\rho q}$ predicted by Derjaguin's equation was computed through the excess enthalpy profile in the channel. Their result related to the mechanocaloric route shows that, in order to describe thermo-osmosis in this kind of system, Derjaguin's equation must be modified: Hydrodynamic corrections accounting for the presence of slippage or stagnant fluid layers in the proximity of the confining walls must be added. Results related to the thermo-osmotic route are less clear, because of viscous effects induced by the geometry of the simulation system. Anyway the adoption of propers corrections allows to recover the results of the mechanocaloric route. Thus, Derjaguin result cannot by itself correctly describe thermo-osmosis in liquid systems. Furthermore, their results show that weakly attractive wall-fluid interactions enhance the thermo-osmotic flow more than the strong attractive ones and in the first case this mass flux is directed towards the cold side of the channel, while in the second towards the hot one. Moreover, in this paper they also measured a giant thermo-osmotic response of the water-graphene interface, which the authors related to the very low interfacial friction displayed by this system.

[12]That is a solid made of indipendent harmonic oscillators.

This topic was better tackled in a second article [30] published the following year. Also the group in Cambridge published two articles regarding numerical simulations of thermo-osmosis in dense fluids. In the first work [32] the authors compared the slip velocity obtained through three different routes. The first one is the so-called *mechanical route*, which develops in two sets of simulations. First they computed the pressure tensor at different temperautres through equilibrium simulations by use of two different microscopic definitions[13]. Then they exploited these results to evaluate the mechanical force exerted on a fluid placed in a temperature gradient aligned to the surface, which is the derivative of the tangential (to the surface) pressure with respect to temperature. Finally they run isothermal simulations applying these forces to the fluid particles and computed the resulting slip velocity. The second route is the *thermodynamic route*, where the slip velocity is computed from Derjaguin's equation. The enthalpy has been computed as

$$h(z) = u(z) + \frac{p(z)}{\rho(z)}\,, \tag{1.9}$$

where $u(z)$ is the local energy density, $p(z)$ is the tangential component of the virial expression for the local tangential pressure and $\rho(z)$ is the local density. Note that this definition of enthalpy holds only in bulk. The last route exploits the Onsager reciprocal relations and is very similar to the *mechanocaloric route* proposed by Fu *et al.* [29]. Authors concluded this paper stating that the results obtained with the three different methods are in good agreement. Moreover they underlined also the presence of a strong fluid viscosity space dependence. In the second article [33] a special solution to directly compute the force exterted on fluid particles due to the presence of a temperature gradient is devised. A temperature gradient is generated in the x direction and, at a given time, the particle motion in this direction is paralyzed: In this way the effective force exerted by the temperature gradient is not balanced by the viscous forces, and thus it is measurable. Authors compared this exact force with the ones computed as derivative with respect to temperature of two definitions of the tangential pressure and the one computed through enthalpy. They concluded that the last one better predicts the directly computed force. We remark that these kind of comparisons are not fully jutified because of intrinsic ambiguities in the microscopic definition of the pressure tensor [70]. It is interesting to note that in 2019 a numerical study of thermo-osmosis was proposed by Proesmans and Frenkel [67] where molecular dynamics technique was not employed, in fact the authors exploit instead the multiparticle collision dynamic technique, also known as stochastic rotation dynamics.

[13] The question of the non unicity of the pressure tensor will be addressed in the next two Chapters.

2

Thermal forces from a microscopic perspective

The physical understanding of the mechanisms driving thermo-osmosis has been studied in the past by the use of two different theoretical tools for gases and liquids. While in gases the kinetic theory is employed, in liquids it is described through nonequilibrium thermodynamics. As a consequence also the emerging pictures describing thermo-osmosis in these two density regimes are completely different: In the rarefied limit the particle-surface interaction plays a key role, while in the dense one the anisotropy of the pressure tensor near the confining surface holds responsible for the mass flow. Moreover nonequilibrium thermodynamics does not take into account for the non-uniqueness of the pressure tensor, even if Ganti *et al.* showed the importance of this aspect within thermo-osmosis [32, 33].

In order to obtain a unified description of this phenomenon and a deeper understanding of its basic mechanisms, i. e. the thermal forces, we developed an *ab initio* microscopic theory of thermo-osmosis. The starting point is the definition, through the microscopic conservation laws, of the operators related to the desired physical quantities. The link between these microscopic operators and the associated physical observables is provided by the statistical mechanics but, being this a nonequilibrium phenomenon, a proper way to compute the averages must be developed. For this reason the linear response theory, generalized to inhomogeneous and anisotropic environments, is employed. Finally, suitable boundary conditions will be adopted in the resulting equations for the mass transport in open and closed channels and a comparison with the

previous theoretical approaches will be provided.

2.1 MICROSCOPIC CONSERVATION LAWS

The objective of this Section is to provide the local expressions of the fluxes which satisfy the microscopic counterpart of the macroscopic conservation laws of mass, momentum and energy. Let us consider a system of N particles which at a given instant of time are characterized by $dN = M$ (being d the dimensionality of the system) generalized coordinates q_i and M conjugated momenta p_i. This set of variables (q, p) describes any physical observable $A(q, p)$ of the system and their time evolution is determined by the Hamiltonian function $H(q, p)$. In fact the trajectories in the phase space $(q(t), p(t))$ are solutions of the Hamilton's equations

$$\begin{cases} \dot{q}_i = \frac{\partial H}{\partial p_i} \\ \dot{p}_i = -\frac{\partial H}{\partial q_i} \end{cases} \tag{2.1}$$

once the initial condition $q_i(0)$ and $p_i(0)$ are given. This time evolution of q and p is reflected also in any physical observable $A(q, p)$

$$\begin{aligned} \frac{\mathrm{d}A}{\mathrm{d}t} &= \sum_i^M \left[\frac{\partial A}{\partial q_i} \dot{q}_i + \frac{\partial A}{\partial p_i} \dot{p}_i \right] \\ &= \sum_i^M \left[\frac{\partial A}{\partial q_i} \frac{\partial H}{\partial p_i} - \frac{\partial A}{\partial p_i} \frac{\partial H}{\partial q_i} \right] \\ &= -\mathcal{L} A \end{aligned} \tag{2.2}$$

where the Liouville operator $\mathcal{L}$

$$\mathcal{L} \cdot = \sum_i^M \left[\frac{\partial H}{\partial p_i} \frac{\partial}{\partial q_i} - \frac{\partial H}{\partial q_i} \frac{\partial}{\partial p_i} \right] \cdot \tag{2.3}$$

has been introduced and it formally expresses the time evolution of physical observables.

Now let us consider a system of point particles of equal mass m and interacting through a central pair-wise additive potential $\varphi(|\boldsymbol{r}|)$ in the presence of an external potential $V(\boldsymbol{r})$. Let us consider the generalized coordinates and conjugated momenta as the components of the position q_i^α and of the momenta

p_i^α of the particles[1]. Thus the Hamiltonian of the system can be express as

$$\begin{aligned} H\left(\{q_i^\alpha\},\{p_i^\alpha\}\right) &= \sum_i^N \frac{|\boldsymbol{p}_i|^2}{2m} + \frac{1}{2}\sum_{i\neq j}^N \varphi_{ji} + \sum_i^N V(\boldsymbol{q}_i) \\ &= H_K\left(\{p_i^\alpha\}\right) + H_\varphi\left(\{q_i^\alpha\}\right) + H_V\left(\{q_i^\alpha\}\right) \end{aligned} \tag{2.4}$$

being $\varphi_{ji} = \varphi(|\boldsymbol{q}_i - \boldsymbol{q}_j|)$ and where the kinetic, internal potential and external potential contributions to the Hamiltonian have been highlighted. As a consequence also the Liouville operator can be separated into these contributions

$$\begin{aligned} \mathcal{L} &= \mathcal{L}_K + \mathcal{L}_\varphi + \mathcal{L}_V \\ &= -\sum_i^N \frac{\boldsymbol{p}_i}{m}\frac{\partial}{\partial \boldsymbol{q}_i} + \sum_{i\neq j}^N \frac{\partial \varphi_{ji}}{\partial \boldsymbol{q}_i}\left(\frac{\partial}{\partial \boldsymbol{p}_i} - \frac{\partial}{\partial \boldsymbol{p}_j}\right) + \sum_{i\neq j}^N \frac{\partial V(\boldsymbol{q}_i)}{\partial \boldsymbol{q}_i}\frac{\partial}{\partial \boldsymbol{p}_i}\,. \end{aligned} \tag{2.5}$$

This form of the Liouville operator is particularly helpful for the derivation of the microscopic counterpart of the macroscopic conservation laws of mass, momentum and energy, and will be later exploited.
Now let us consider the usual definition for the local mass density

$$\hat{\rho}(\boldsymbol{r}) = m\sum_i^N \delta(\boldsymbol{q}_i - \boldsymbol{r}) \tag{2.6}$$

and the local momentum density

$$\hat{j}^\alpha(\boldsymbol{r}) = \sum_i^N \delta(\boldsymbol{q}_i - \boldsymbol{r}) p_i^\alpha \tag{2.7}$$

and let us define the local energy density operator as

$$\begin{aligned} \hat{\mathcal{H}}(\boldsymbol{r}) &= \sum_i^N \delta(\boldsymbol{q}_i - \boldsymbol{r})\hat{h}_i \\ &= \sum_i^N \delta(\boldsymbol{q}_i - \boldsymbol{r})\left[\frac{p_i^2}{2m} + \frac{1}{2}\sum_{j(\neq i)}^N \varphi_{ji} + V(\boldsymbol{q}_i)\right] \end{aligned} \tag{2.8}$$

where it is important to remark that the the interaction energy φ_{ji} between two particles i and j, located at $\boldsymbol{q}_i$ and $\boldsymbol{q}_j$, is ascribed without justification half to the particle i and half to the particle j. Another admissible definition of the local energy density could ascribe, for example, the whole interaction energy φ_{ji} to the point $(\boldsymbol{q}_i + \boldsymbol{q}_j)/2$. The apparent ambiguity in Equation 2.8

[1] All over ths work Latin indices refer to particles, while Greek ones to vector components.

is related to the non-local nature of the inter-particle interaction potential φ_{ji} [69, 42] and disappears when $\hat{\mathcal{H}}(\boldsymbol{r})$ is integrated over the volume of the system [21]

$$\begin{aligned}\hat{H} &= \int \mathrm{d}\boldsymbol{r}\hat{\mathcal{H}}(\boldsymbol{r}) \\ &= \sum_{i}^{N}\left[\frac{p_i^2}{2m} + \frac{1}{2}\sum_{j(\neq i)}^{N}\varphi_{ji} + V(\boldsymbol{q}_i)\right] .\end{aligned} \tag{2.9}$$

The microscopic conservation laws for the local mass density, local momentum density and local energy density can now be obtained exploiting Equation 2.2.

2.1.1 Mass conservation

The microscopic continuity equation for the mass local density can be easily expressed as

$$\begin{aligned}\frac{\mathrm{d}\hat{\rho}(\boldsymbol{r})}{\mathrm{d}t} &= -\mathcal{L}_K\hat{\rho}(\boldsymbol{r}) \\ &= \sum_{i}^{N}\frac{\partial}{\partial\boldsymbol{q}_i}\delta(\boldsymbol{q}_i-\boldsymbol{r})\boldsymbol{p}_i \\ &= -\partial_\alpha\hat{j}^\alpha(\boldsymbol{r})\end{aligned} \tag{2.10}$$

where ∂_α is the partial derivative w.r.t. q^α. Equation 2.10 has the form of a continuity equation expressing the conservation of the mass at the microscopic level.
It is important to point out that equation 2.10 is fulfilled by any microscopic mass current operator $\hat{j}^\alpha_\rho(\boldsymbol{r})$, defined as

$$\hat{j}^\alpha_\rho(\boldsymbol{r}) = \hat{j}^\alpha(\boldsymbol{r}) + \Gamma^\alpha(\boldsymbol{r})\,, \tag{2.11}$$

where $\Gamma^\alpha(\boldsymbol{r})$ is any vector field characterized by a vanishing divergence:

$$\partial_\alpha\Gamma^\alpha(\boldsymbol{r}) = 0\,. \tag{2.12}$$

This simple argument shows an important feature of continuity equations, that is they define fluxes of conserved quantities only up to zero-divergent vector fields.

2.1.2 Momentum conservation

The same procedure can be exploited to express the local conservation law corresponding to the macroscopic momentum balance equation, i. e. evaluating

the rate of change of the momentum local density $\hat{j^{\alpha}}(\boldsymbol{r})$ applying the Liouville operator:

$$\begin{aligned}\frac{\mathrm{d}\hat{j}^{\alpha}(\boldsymbol{r})}{\mathrm{d}t} &= -\mathcal{L}\hat{j}^{\alpha}(\boldsymbol{r}) \\ &= -\partial_{\beta}\left[\sum_{i}^{N}\frac{p_i^{\alpha}p_i^{\beta}}{m}\delta(\boldsymbol{q}_i-\boldsymbol{r})\right] - \frac{\hat{\rho}(\boldsymbol{r})}{m}\partial_{\alpha}V(\boldsymbol{r}) \\ &\quad -\frac{1}{2}\sum_{i\neq l}^{N}\frac{\partial\varphi_{li}}{\partial q_i^{\alpha}}\left[\delta(\boldsymbol{q}_i-\boldsymbol{r})-\delta(\boldsymbol{q}_l-\boldsymbol{r})\right]\,.\end{aligned} \tag{2.13}$$

In order to obtain the expression of the flux associated to $\hat{j}^{\alpha}(\boldsymbol{r})$ the last term in Equation 2.13 must be written as the divergence of a second-rank tensor and it can be accomplished through the distributional identity [70]:

$$\begin{aligned}\delta(\boldsymbol{q}_i-\boldsymbol{r})-\delta(\boldsymbol{q}_l-\boldsymbol{r}) &= \oint_{\ell_{l\to i}}\mathrm{d}y^{\gamma}\frac{\partial}{\partial y^{\gamma}}\delta(\boldsymbol{y}-\boldsymbol{r}) \\ &= -\partial_{\gamma}\oint_{\ell_{l\to i}}\mathrm{d}y^{\gamma}\delta(\boldsymbol{y}-\boldsymbol{r})\,,\end{aligned} \tag{2.14}$$

where this integral can be taken along any contour $\ell_{l\to i}$ from $\boldsymbol{q}_l$ to $\boldsymbol{q}_i$. Thus this result, together with Equation 2.13, define the microscopic continuity equation for the momentum local density $\hat{j}^{\alpha}(\boldsymbol{r})$

$$\frac{\mathrm{d}\hat{j}^{\alpha}(\boldsymbol{r})}{\mathrm{d}t} = -\partial_{\beta}\hat{J}_j^{\alpha\beta}(\boldsymbol{r}) - \frac{\hat{\rho}(\boldsymbol{r})}{m}\partial_{\alpha}V(\boldsymbol{r})\,, \tag{2.15}$$

where the last term acts as a source contribution when a space dependent external field $V(\boldsymbol{r})$ is present. Moreover in equation 2.15 the microscopic momentum current local density operator $\hat{J}_j^{\alpha\beta}(\boldsymbol{r})$ has been defined as[2]

$$\hat{J}_j^{\alpha\beta}(\boldsymbol{r}) = \sum_{i}^{N}\frac{p_i^{\alpha}p_i^{\beta}}{m}\delta(\boldsymbol{q}_i-\boldsymbol{r}) + \frac{1}{2}\sum_{i\neq l}^{N}\frac{\partial\varphi_{li}}{\partial q_i^{\alpha}}\oint_{\ell_{l\to i}}\mathrm{d}y^{\gamma}\delta(\boldsymbol{y}-\boldsymbol{r})\,. \tag{2.16}$$

and the average value of this operator is the well-known (local) pressure tensor

$$p^{\alpha\beta}(\boldsymbol{r}) = \langle\hat{J}_j^{\alpha\beta}(\boldsymbol{r})\rangle\,. \tag{2.17}$$

Note that the expression for $\hat{J}_j^{\alpha\beta}(\boldsymbol{r})$ in Equation 2.14 can be slightly simplified if referred to systems where particles interact through a central pair-wise

[2]Strictly related to the stress tensor $\hat{\sigma}^{\alpha\beta}(\boldsymbol{r})$: $\hat{\sigma}^{\alpha\beta}(\boldsymbol{r}) = -\hat{J}_j^{\alpha\beta}(\boldsymbol{r})$.

potential:

$$\begin{aligned}\hat{J}_j^{\alpha\beta}(\boldsymbol{r}) = &\sum_i^N \frac{p_i^\alpha p_i^\beta}{m}\delta(\boldsymbol{q}_i - \boldsymbol{r}) \\ &- \frac{1}{2}\sum_{i\neq l}^N \frac{q^\alpha}{|\boldsymbol{q}_{li}|}\frac{\mathrm{d}\varphi(q)}{\mathrm{d}q}\bigg|_{q=|\boldsymbol{q}_{li}|}\oint_{\ell_{l\to i}} \mathrm{d}y^\beta \delta(\boldsymbol{y}-\boldsymbol{r})\,.\end{aligned} \tag{2.18}$$

Comment on the microscopic momentum current local density operator

Equation 2.14 shows how the momentum current local density can not be defined without ambiguity: Different contours in 2.14 lead to different expressions for $\hat{J}_j^{\alpha\beta}(\boldsymbol{r})$, and the same considerations also apply to the pressure tensor defined in equation 2.17. For example, if a system where particles interact through a central pair-wise additive potential is considered, the local pressure tensor reads [70]

$$\begin{aligned}p^{\alpha\beta}(\boldsymbol{r}) = &\frac{\rho(\boldsymbol{r})k_BT}{m}\delta^{\alpha\beta} \\ &- \frac{1}{2}\int \mathrm{d}\boldsymbol{y}\frac{y^\alpha}{|\boldsymbol{y}|}\frac{\mathrm{d}\varphi(|\boldsymbol{y}|)}{\mathrm{d}|\boldsymbol{y}|}\oint_{\ell_{\boldsymbol{o}\to\boldsymbol{y}}} \mathrm{d}s^\beta \rho^{(2)}(\boldsymbol{r}-\boldsymbol{s},\boldsymbol{r}-\boldsymbol{s}+\boldsymbol{y})\,,\end{aligned} \tag{2.19}$$

where $\delta^{\alpha\beta}$ is the Kronecker's delta operator. Here $\rho^{(2)}(\boldsymbol{r},\boldsymbol{r}')$ is the two-particle density [36] and the line-integral is extended, without any loss in generality, from the origin $\boldsymbol{o}$ to a given point $\boldsymbol{y}$. Making use of this result it is possible to show that in the homogeneous and isotropic limit the ambiguity in the definition of the pressure tensor disappears. Indeed the two-particle distribution function can be expressed in terms of the radial distribution function

$$\rho^{(2)}(\boldsymbol{r},\boldsymbol{r}') = \frac{\rho^2}{m^2}g(|\boldsymbol{r}-\boldsymbol{r}'|) \tag{2.20}$$

and thus Equation 2.19 reduces to

$$\begin{aligned}p^{\alpha\beta}(\boldsymbol{r}) &= p\delta^{\alpha\beta} \\ &= \frac{\rho(\boldsymbol{r})k_BT}{m}\delta^{\alpha\beta} - \frac{1}{2}\frac{\rho^2}{m^2}\int \boldsymbol{r}\frac{r^\alpha r^\beta}{|\boldsymbol{r}|}\frac{\mathrm{d}\varphi(|\boldsymbol{r}|)}{\mathrm{d}|\boldsymbol{r}|}g(|\boldsymbol{r}|)\,,\end{aligned} \tag{2.21}$$

which is the well known virial expression for the pressure in a homogeneous and isotropic fluid at density ρ [36].

The problem of the non-uniqueness of the local pressure tensor was firstly implicitly recognized by Kirkwood in the fifties. He obtained two different expressions for the configurational contribution to the stress tensor: The first one in a paper with Buff [45] and the second in another work with Irving[3] [42]. The first explicit description of this ambiguity was given by Harasima[4]

[3] The so called Irving-Kirkwood stress tensor, which will be discussed in the next Chapter.
[4] Also the Harasima stress tensor will be better introduced in the next Chapter.

in 1958 [38] and a review was published by Ono and Kondo [58] a couple of years later. A rigorous and exhaustive study of the problem was given in the eighties by Schofield and Henderson [70]. More recently, Baus and Lovett [6, 7] (and also other authors) have attempted to define the pressure tensor uniquely. However, their definition can not be accepted because it only holds for particular geometries [69, 68]. This ambiguity related to the definition of the pressure tensor has been recently revived in two numerical papers [32, 33] dealing with thermo-osmosis. The authors try to discriminate between different expressions of the pressure tensor estimating the value of the thermo-osmotic flow resulting from (approximate) predictions which involve the knowledge of the pressure tensor itself. In the most recent paper [33], they compare these predictions with the exact results obtained through a clever nonequilibrium molecular dynamics simulation: They conclude that both the virial[5] and the Irving-Kirkwood expressions do not accurately predict surface forces due to temperature gradients.

However, we remark that the infinite possible definitions of the the pressure tensor are indeed equivalent, i.e. all the physical observables must be invariant with respect to different choices of the path $\ell_{i\to j}$ [70]. As regards an inhomogeneous fluid, the pressure tensor itself is not a well defined observable on a length scale shorter than the correlation length or the range of the inter-particle potential [69]. Qualitatively, we can try to understand this circumstance reflecting on the fact that it is not possible to identify the surface where the pressure is acting. Analogously, we can not define without ambiguities the surface which separates two different phases of the same fluid. On the other hand, both the pressure exerted on a given region of fluid and the surface tension of an interface are well defined observables: Indeed proving that they do not depend on the particular definition of the pressure tensor is possible[70]. As regards approximate theories, such as the local equilibrium assumption or the approach originally put forward by Derjaguin and recently re-derived in [32], the invariance of the observables with respect different definitions of the pressure tensor is not guaranteed *a priori*. However, the slip velocity of a fluid subject to a temperature gradient is a genuine physical quantity, also from the microscopic viewpoint. Therefore every exact prediction of the thermo-osmotic slip must be invariant on the choice of the trajectory in 2.14: We conclude that both the local thermal equilibrium and the Derjaguin approach should be considered as approximations, because their expression are not endowed by this invariance.

Finally, we remark that the virial pressure tensor (Equation 2.21) extended to inhomogeneous systems, which has been evaluated in [32, 33] in order to obtain the thermo-osmotic properties of the fluid, does not correspond to any choice of the path in 2.14 and in addition it does not fulfill the hydrostatic balance

[5]Note that any contour $\ell_{i\to j}$ can not define the virial expression for the pressure. This means that the virial one is not an admissible definition of the pressure tensor.

condition: If a fluid is in equilibrium near a surface, than the profile of its pressure component normal to this confinement must be shaped in order to balance the force exerted on the fluid by the surface, but the virial pressure tensor does not satisfy this condition. This expression is commonly adopted within continuum hydrodynamics, where it is assumed that the relevant quantities vary on a length scale much larger than the correlation length.

2.1.3 Energy conservation

The same steps followed before in the case of the mass and momentum currents allow also to define the microscopic conservation law for the energy local density $\hat{\mathcal{H}}(\boldsymbol{r})$

$$\begin{aligned}\frac{\mathrm{d}\hat{\mathcal{H}}(\boldsymbol{r})}{\mathrm{d}t} &= -\mathcal{L}\hat{\mathcal{H}}(\boldsymbol{r}) \\ &= -\mathcal{L}_K\hat{\mathcal{H}}(\boldsymbol{r}) - \sum_i^N \delta(\boldsymbol{q}_i-\boldsymbol{r})\left[\mathcal{L}_\varphi+\mathcal{L}_V\right]\frac{p_i^2}{2m}\,.\end{aligned} \tag{2.22}$$

The action of the Liouvillians on the energy local density operator reads

$$\begin{aligned}\mathcal{L}_K\hat{\mathcal{H}}(\boldsymbol{r}) = &\sum_i^N \frac{p_i^\alpha}{m}\left[h_i\partial_\alpha\delta(\boldsymbol{q}_i-\boldsymbol{r}) - \frac{\partial V(\boldsymbol{q}_i)}{\partial q_i^\alpha}\right] \\ &- \frac{1}{2m}\sum_{i\neq j}^N \delta(\boldsymbol{q}_i-\boldsymbol{r})\frac{\partial\varphi_{ji}}{\partial q_i^\alpha}(p_i^\alpha-p_j^\alpha)\end{aligned} \tag{2.23}$$

for the kinetic part and

$$\left[\mathcal{L}_\varphi+\mathcal{L}_V\right]\frac{p_i^2}{2m} = \frac{p_i^\alpha}{m}\left[\sum_{j(\neq i)}^N \frac{\partial\varphi_{ji}}{\partial q_i^\alpha} + \frac{\partial V(\boldsymbol{q}_i)}{\partial q_i^\alpha}\right] \tag{2.24}$$

for the potential contributions. Making use of these results we get

$$\frac{\mathrm{d}\hat{\mathcal{H}}(\boldsymbol{r})}{\mathrm{d}t} = -\partial_\alpha\left[\sum_i^N \delta(\boldsymbol{q}_i-\boldsymbol{r})\frac{p_i^\alpha}{m}\hat{h}_i\right] - \frac{1}{2m}\sum_{i\neq j}^N p_i^\alpha\frac{\partial\varphi_{ji}}{\partial q_i^\alpha}\left[\delta(\boldsymbol{q}_i-\boldsymbol{r})-\delta(\boldsymbol{q}_j-\boldsymbol{r})\right] \tag{2.25}$$

and the distributional identity (Equation 2.14) allows to express Equation 2.25 in the form of a microscopic conservation law

$$\frac{\mathrm{d}\hat{\mathcal{H}}(\boldsymbol{r})}{\mathrm{d}t} = -\partial_\alpha\hat{J}_{\mathcal{H}}^\alpha(\boldsymbol{r})\,, \tag{2.26}$$

where the energy local density current has been defined

$$\hat{J}^{\alpha}_{\mathcal{H}}(\boldsymbol{r}) = \sum_{i}^{N} \delta(\boldsymbol{q}_i - \boldsymbol{r}) \frac{p_i^{\alpha}}{m} \hat{h}_i + \frac{1}{2} \sum_{i}^{N} \frac{p_i^{\delta}}{m} \sum_{j(\neq i)}^{N} \frac{\partial \varphi_{ji}}{\partial q_i^{\alpha}} \oint_{\ell_{i \to j}} \mathrm{d}y^{\alpha} \delta(\boldsymbol{y} - \boldsymbol{r}) \,. \quad (2.27)$$

Here we stress that Equation 2.27 is the microscopic energy flux according to the definition of the local energy density given in Equation 2.8. Different microscopic forms of the local energy provide different expressions of $\hat{J}^{\alpha}_{\mathcal{H}}(\boldsymbol{r})$. In addition to this, the same considerations stated above for the momentum current apply: The ambiguity in the definition of the heat flux is recovered in the freedom connected to the choice of the integration path. However the thermal transport coefficients, which are genuine physical observables, turn out to be independent on the particular choice in Equations 2.27 and 2.8 [21].

2.2 EVALUATION OF THE AVERAGES

In the previous Section we have defined microscopic operators related to the physical observables of interest for the description of thermo-osmosis. The link between these operators and the associated physical observables is provided by the statistical mechanics through the phase-space distribution function $F(q, p)$:

$$\langle A \rangle = \int \int \mathrm{d}q \, \mathrm{d}p \, A(q, p) F(q, p) \quad (2.28)$$

where $A(q, p)$ is any dynamical function and $\langle A \rangle$ the associated physical observable. Let us now consider a system prepared in a starting state F_0 and let us apply a certain perturbation to it at a given instant of time $t = 0$. Consequently the distribution function related to this system will evolve in time. Being $F(q, p)$ a dynamical function of the phase space, also its time evolution is regulated by the Liouville equation

$$\partial_t F(t) = \mathcal{L} F(t) \quad (2.29)$$

which must be supplemented with the initial condition $F(t = 0) = F_0$. The formal solution of Equation 2.29 can be written as

$$F(t) = \mathcal{U}(t) F_0 \quad (2.30)$$

where $\mathcal{U}(t) = \exp\{t\mathcal{L}\}$ is the so called Green propagator.
These considerations are important for our purpose: In order to describe this nonequilibrium phenomenon we can think to start from an equilibrium system, characterized by an equilibrium distribution function F^{eq}, apply to it a thermal gradient and let evolve it towards a stationary nonequilibrium state, characterized by a distribution function F which is stationary solution of the Liouville Equation 2.29.

2.2.1 Local equilibrium averages

Thermo-osmosis is a nonequilibrium phenomenon. In order to give a statistical description of it we can start considering a distribution function which describes a system slightly out of equilibrium, the so-called Local thermal Equilibrium (LE) distribution function. To introduce it, let us consider a system of interacting particles in the presence of an external potential, described by the Hamiltonian defined in Equation 2.4 and kept at non-uniform temperature. Following the approach developed by Mori [54, 55], we define the LE distribution function, which resembles a local generalization of the Boltzmann distribution:

$$F^{LE} = \mathcal{Q}^{-1} \mathrm{e}^{-\int \mathrm{d}\boldsymbol{r} \beta(\boldsymbol{r}) \hat{\mathcal{E}}(\boldsymbol{r})} \,. \tag{2.31}$$

Here $\beta(\boldsymbol{r})$ is a scalar field related to the local temperature, $\hat{\mathcal{E}}(\boldsymbol{r})$ is the internal energy local density operator and $\mathcal{Q}$ is the Local Equilibrium partition function. The presence of a non-uniform temperature in principles induces in the system a non-uniform chemical potential and a local velocity profile. Therefore also the contributions arising from these two local fields must be included in the internal energy expression:

$$\hat{\mathcal{E}}(\boldsymbol{r}) = \hat{\mathcal{H}}(\boldsymbol{r}) - \hat{\boldsymbol{j}}(\boldsymbol{r}) \cdot \boldsymbol{u}(\boldsymbol{r}) - \hat{\rho}(\boldsymbol{r}) \mu(\boldsymbol{r}) \,, \tag{2.32}$$

where the local Hamiltonian, momentum and particles density have been defined in the previous Section, while $\boldsymbol{u}(\boldsymbol{r})$ and $\mu(\boldsymbol{r})$ are the vector and scalar fields linked respectively to the local velocity profile and the chemical potential (per unit mass) of the fluid. These three fields just introduced couple locally to the conserved quantities: $\mu(\boldsymbol{r})$ couples to the local mass, $\boldsymbol{u}(\boldsymbol{r})$ to the local momentum and $\beta(\boldsymbol{r})$ to the local energy. These fields define the LE state and are considered as external known parameters (we will discuss later how to fix them). In order to justify the linear response formalism later employed, we require that they are smooth functions and that their gradients $\partial_\alpha \beta(\boldsymbol{r})$, $\partial_\alpha u^\beta(\boldsymbol{r})$ and $\partial_\alpha \mu(\boldsymbol{r})$ are small. Furthermore we limit to the study of systems where it is possible to find a Galileo transformation such that the field $\boldsymbol{u}(\boldsymbol{r})$ is small[6].

The LE distribution defined in Equation 2.31 allows to compute the averages of the previously introduced microscopic operators in a Local Equilibrium state. This average evaluation can be accomplished within linear response theory, as explained in the following. The fundamental hypothesis is that the nonequilibrium state described by the LE distribution is a small perturbation of an equilibrium state, characterized by the equilibrium distribution function

$$F^{eq} = \mathcal{Q}_0^{-1} \mathrm{e}^{-\beta(H - \mu m N)} \,, \tag{2.33}$$

[6]For this reason we can neglect the quadratic term in the reported expression of $\hat{\mathcal{E}}(\boldsymbol{r})$.

where $\mathcal{Q}_0$ is the equilibrium grand canonical partition function while β and μ are respectively uniform temperature and chemical potential (per unit mass) (the velocity field $\boldsymbol{u}(\boldsymbol{r})$ does not appear in this equilibrium state). In the LE state these fields can be written in terms of small deviations from their values in the equilibrium one:

$$\beta(\boldsymbol{r}) = \beta + \delta\beta(\boldsymbol{r}) \tag{2.34}$$

$$\mu(\boldsymbol{r}) = \mu + \delta\mu(\boldsymbol{r}) \tag{2.35}$$

$$\boldsymbol{u}(\boldsymbol{r}) = \boldsymbol{0} + \delta\boldsymbol{u}(\boldsymbol{r})\,. \tag{2.36}$$

These considerations allow to express the LE state as a slight deviation from the equilibrium one, thus, inspired by the linear response theory, we expand the LE distribution 2.31 about F^{eq}, expressed in Equation 2.33, to the first order in the deviations $\delta\beta(\boldsymbol{r})$, $\delta\mu(\boldsymbol{r})$ and $\delta\boldsymbol{u}(\boldsymbol{r})$. These deviations appear both in the exponential and in the partition function $\mathcal{Q}$, thus the linearized local equilibrium distribution reads

$$\begin{aligned} F^{LE} &= \mathcal{Q}^{-1}\mathrm{e}^{-\int \mathrm{d}\boldsymbol{r}\beta(\boldsymbol{r})\hat{\mathcal{E}}(\boldsymbol{r})} \\ &\simeq \frac{\mathcal{Q}_0 F^{eq}(1-\hat{\mathcal{C}}_\mathrm{e})}{\mathcal{Q}_0(1-\mathcal{C}_\mathcal{Q})} \\ &\simeq F^{eq}(1-\hat{\mathcal{C}}_\mathrm{e}+\mathcal{C}_\mathcal{Q})\,, \end{aligned} \tag{2.37}$$

where the linear corrections in the exponential and in the partition function are

$$\begin{aligned} \hat{\mathcal{C}}_\mathrm{e} &= \int \mathrm{d}\boldsymbol{r}\left\{\delta\beta(\boldsymbol{r})\left[\hat{\mathcal{H}}(\boldsymbol{r})-\mu\hat{\rho}(\boldsymbol{r})\right]-\beta\left[\hat{\boldsymbol{j}}(\boldsymbol{r})\cdot\delta\boldsymbol{u}(\boldsymbol{r})+\delta\mu(\boldsymbol{r})\hat{\rho}(\boldsymbol{r})\right]\right\}, \\ \mathcal{C}_\mathcal{Q} &= \int \mathrm{d}\boldsymbol{r}\left\{\delta\beta(\boldsymbol{r})\left[\langle\hat{\mathcal{H}}(\boldsymbol{r})\rangle_0-\mu\langle\hat{\rho}(\boldsymbol{r})\rangle_0\right]+\beta\delta\mu(\boldsymbol{r})\langle\hat{\rho}(\boldsymbol{r})\rangle_0\right\}, \end{aligned} \tag{2.38}$$

where the averages $\langle ...\rangle_0$ are evaluated through the equilibrium distribution F^{eq} and the different notation between $\hat{\mathcal{C}}_\mathrm{e}$ and $\mathcal{C}_\mathcal{Q}$ underlines that only $\hat{\mathcal{C}}_\mathrm{e}$ still depends on the phase-space coordinates. The final expression for the LE distribution within the linear approximation is given by

$$\begin{aligned} F^{LE} = F^{eq}\Bigg\{1-\int \mathrm{d}\boldsymbol{r}\Big\{&\delta\beta(\boldsymbol{r})\left[\hat{\mathcal{H}}(\boldsymbol{r})-\mu\hat{\rho}(\boldsymbol{r})\right] \\ &-\beta\left[\hat{\boldsymbol{j}}(\boldsymbol{r})\cdot\delta\boldsymbol{u}(\boldsymbol{r})+\delta\mu(\boldsymbol{r})\hat{\rho}(\boldsymbol{r})\right]\Big\}+\mathcal{C}_\mathcal{Q}\Bigg\}\,. \end{aligned} \tag{2.39}$$

Thus, we can express the local equilibrium average of an observable $\hat{A}(\boldsymbol{r})$ as

$$\begin{aligned} \langle\hat{A}(\boldsymbol{r})\rangle_{LE} = &\langle\hat{A}(\boldsymbol{r})\rangle_0 \\ &-\int \mathrm{d}\boldsymbol{r}'\Big\{\delta\beta(\boldsymbol{r}')\left[\langle\hat{A}(\boldsymbol{r})\hat{\mathcal{H}}(\boldsymbol{r}')\rangle_0-\mu\langle\hat{A}(\boldsymbol{r})\hat{\rho}(\boldsymbol{r}')\rangle_0\right] \\ &-\beta\left[\langle\hat{A}(\boldsymbol{r})\hat{j}^\alpha(\boldsymbol{r}')\rangle_0\delta u^\alpha(\boldsymbol{r}')+\delta\mu(\boldsymbol{r}')\langle\hat{A}(\boldsymbol{r})\hat{\rho}(\boldsymbol{r}')\rangle_0\right]\Big\} \\ &+\mathcal{C}_\mathcal{Q}\langle\hat{A}(\boldsymbol{r})\rangle_0\,. \end{aligned} \tag{2.40}$$

It is important to notice that the expression for $\langle \hat{A}(\boldsymbol{r})\rangle_{LE}$ can lose some terms: All the equilibrium averages $\langle \hat{\mathcal{O}}\rangle_0$ that appear in Equation 2.40 vanish if the averaged resulting operator $\hat{\mathcal{O}}$ is odd in the momentum coordinates[7].
It is now possible to apply this result to express the local equilibrium averages for the most relevant observables. In the case of the momentum density it can be expressed as

$$\begin{aligned}\langle \hat{j}^{\alpha}(\boldsymbol{r})\rangle_{LE} &= \beta \int \mathrm{d}\boldsymbol{r}' \langle \hat{j}^{\alpha}(\boldsymbol{r})\hat{j}^{\gamma}(\boldsymbol{r}')\rangle_0 u^{\gamma}(\boldsymbol{r}') \\ &= \langle \hat{\rho}(\boldsymbol{r})\rangle_0 u^{\alpha}(\boldsymbol{r}')\end{aligned} \tag{2.41}$$

while for the energy current it is

$$\langle \hat{J}^{\alpha}_{\mathcal{H}}(\boldsymbol{r})\rangle_{LE} = \beta \int \mathrm{d}\boldsymbol{r}' \langle \hat{J}^{\alpha}_{\mathcal{H}}(\boldsymbol{r})\hat{j}^{\gamma}(\boldsymbol{r}')\rangle_0 u^{\gamma}(\boldsymbol{r}') \tag{2.42}$$

and for the mass density

$$\begin{aligned}\langle \hat{\rho}(\boldsymbol{r})\rangle_{LE} = \langle \hat{\rho}(\boldsymbol{r})\rangle_0 \\ - \int \mathrm{d}\boldsymbol{r}' \Big\{ \delta\beta(\boldsymbol{r}') \Big[\langle \hat{\rho}(\boldsymbol{r})\hat{\mathcal{H}}(\boldsymbol{r}')\rangle_0 - \mu \langle \hat{\rho}(\boldsymbol{r})\hat{\rho}(\boldsymbol{r}')\rangle_0 \Big] \\ - \beta\delta\mu(\boldsymbol{r}')\langle \hat{\rho}(\boldsymbol{r})\hat{\rho}(\boldsymbol{r}')\rangle_0 \Big\} + \mathcal{C}_{\mathcal{Q}} \langle \hat{\rho}(\boldsymbol{r})\rangle_0\end{aligned} \tag{2.43}$$

This result can be written in a more suggestive way:

$$\langle \hat{\rho}(\boldsymbol{r})\rangle_{LE} = \langle \hat{\rho}(\boldsymbol{r})\rangle_0 \Big|_{\beta(\boldsymbol{r}),\mu(\boldsymbol{r})} \tag{2.44}$$

showing that the local equilibrium average of the density can be evaluated as an equilibrium average through F^{eq}, provided that the temperature and the chemical potential are fixed at their local value in $\boldsymbol{r}$: $\beta = \beta(\boldsymbol{r})$ and $\mu = \mu(\boldsymbol{r})$. The local equilibrium average of the momentum current reads

$$\begin{aligned}\langle \hat{J}^{\alpha\beta}_{j}(\boldsymbol{r})\rangle_{LE} = \langle \hat{J}^{\alpha\beta}_{j}(\boldsymbol{r})\rangle_0 \\ - \int \mathrm{d}\boldsymbol{r}' \Big\{ \delta\beta(\boldsymbol{r}') \Big[\langle \hat{J}^{\alpha\beta}_{j}(\boldsymbol{r})\hat{\mathcal{H}}(\boldsymbol{r}')\rangle_0 - \mu \langle \hat{J}^{\alpha\beta}_{j}(\boldsymbol{r})\hat{\rho}(\boldsymbol{r}')\rangle_0 \Big] \\ - \beta\delta\mu(\boldsymbol{r}')\langle \hat{J}^{\alpha\beta}_{j}(\boldsymbol{r})\hat{\rho}(\boldsymbol{r}')\rangle_0 \Big\} + \mathcal{C}_{\mathcal{Q}} \langle \hat{J}^{\alpha\beta}_{j}(\boldsymbol{r})\rangle_0 \,.\end{aligned} \tag{2.45}$$

Note that in Equation 2.45 the equilibrium averages $\langle ... \rangle_0$ are different from zero also if $\alpha \neq \beta$, because the configurational contribution of $\hat{J}^{\alpha\beta}_{j}$ is not an odd operator with respect to the momenta. This means that the pressure tensor, which is diagonal in equilibrium systems, can acquire off diagonal

[7] In the equilibrium averages integrals from $-\infty$ to $+\infty$ are performed on the momentum coordinates

components when the state of the system is described by a local thermal equilibrium distribution. Anyway, the same shorthand notation introduced for $\langle \hat{\rho}(\boldsymbol{r}) \rangle_{LE}$ can be applied also for the diagonal components of the pressure tensor:

$$\begin{aligned} \langle \hat{J}_j^{\alpha\alpha}(\boldsymbol{r}) \rangle_{LE} &= \langle \hat{J}_j^{\alpha\alpha}(\boldsymbol{r}) \rangle_0 \Big|_{\beta(\boldsymbol{r}),\mu(\boldsymbol{r})} \\ &= p^{\alpha\alpha}(\boldsymbol{r}) \Big|_{\beta(\boldsymbol{r}),\mu(\boldsymbol{r})} . \end{aligned} \tag{2.46}$$

It is important to note that this simplified way for the evaluation of the averages in local thermal equilibrium is not valid for all the observables: For instance it does not work when the off-diagonal components of the pressure tensor are considered.

2.2.2 Time-evolution of the distribution function

The equilibrium distribution function F^{eq} depends only on the five global constant of motion, thus it is a stationary solution of the Liouville equation 2.29. On the other hand it is possible to show that this is not true for the LE distribution function, i. e. $\mathcal{L}F^{LE} \neq 0$, thus it can not be employed to evaluate averages in stationary conditions. Indeed, if external constraints (as the temperature, the chemical potential and the velocity fields) are kept fixed, the actual phase-space distribution will evolve in time due to the ensuing dynamics towards a stationary (time-independent) out-of-equilibrium distribution. In order to obtain such distribution we follow, with slight changes, the approach proposed by Mori [54, 55]. Thus let us assume that the system is described at $t = 0$ by a given LE state: $F(t = 0) = F^{LE}$. At times $t > 0$ the phase-space distribution $F(t)$ will evolve according to the Liouville equation 2.29, whose formal solution can be written in the integral form as

$$\begin{aligned} F(t) &= F(0) + \int_0^t \mathrm{d}t' \frac{\mathrm{d}}{\mathrm{d}t'} F(t') \\ &= F^{LE} + \int_0^t \mathrm{d}t' \mathcal{L}\mathcal{U}(t') F^{LE} \\ &= F^{LE} + \int_0^t \mathrm{d}t' \mathcal{U}(t') \left[\mathcal{L}F^{LE} \right] , \end{aligned} \tag{2.47}$$

where in the last equality we used the fact that within classical statistical mechanics the Liouvillian operator commutes with the Green propagator. The explicit evaluation of the right hand side of Equation 2.47, to linear order in the field $\boldsymbol{u}(\boldsymbol{r})$ and in the gradients $\partial_\alpha \beta(\boldsymbol{r})$, $\partial_\alpha \mu(\boldsymbol{r})$ and $\partial_\alpha u^\beta(\boldsymbol{r})$, is straightforward. The Liouvillian $\mathcal{L}$ acts on the LE distribution as a partial derivative with

respect to the phase-space coordinates and we get

$$\begin{aligned} F(t) &= F^{LE} - \int_0^t \mathrm{d}t' \int \mathrm{d}\boldsymbol{r}\, \mathcal{U}(t') \left[F^{LE} \beta(\boldsymbol{r}) \mathcal{L}\hat{\mathcal{E}}(\boldsymbol{r}) \right] \\ &= F^{LE} - \int_0^t \mathrm{d}t' \int \mathrm{d}\boldsymbol{r}\, \mathcal{U}(t') \Big\{ F^{LE} \beta(\boldsymbol{r}) \Big[\partial_\alpha \hat{J}^\alpha_{\mathcal{H}}(\boldsymbol{r}) - \partial_\gamma \hat{J}^{\alpha\gamma}_j(\boldsymbol{r}) u^\alpha(\boldsymbol{r}) \\ &\quad - \mu(\boldsymbol{r}) \partial_\alpha \hat{j}^\alpha_\rho - \frac{\hat{\rho}(\boldsymbol{r})}{m} \partial_\alpha V(\boldsymbol{r}) u^\alpha(\boldsymbol{r}) \Big] \Big\}, \end{aligned} \tag{2.48}$$

where the action of $\mathcal{L}$ on the local energy, mass and momentum operators has already been evaluated in Section 2.1 and corresponds to the local conservation of energy, momentum and mass respectively.
Now, if we assume that the perturbation on the system due to the fields $\beta(\boldsymbol{r})$, $\boldsymbol{u}(\boldsymbol{r})$ and $\mu(\boldsymbol{r})$ is small, it is possible to evaluate the response of the system at linear order and thus we can get, within this approximation, the time-dependent average of a local observable $\hat{A}(\boldsymbol{r})$:

$$\begin{aligned} \langle \hat{A}(\boldsymbol{r}) \rangle_t &= \langle \hat{A}(\boldsymbol{r}) \rangle_{LE} \\ &\quad - \int_0^t \mathrm{d}t' \int \mathrm{d}\boldsymbol{r}' \mathrm{Tr} \Big\{ \hat{A}(\boldsymbol{r}) \mathcal{U}(t') \Big[F^{LE} \beta(\boldsymbol{r}') \Big(\partial'_\alpha \hat{J}^\alpha_{\mathcal{H}}(\boldsymbol{r}') - \partial'_\gamma \hat{J}^{\alpha\gamma}_j(\boldsymbol{r}') u^\alpha(\boldsymbol{r}') \\ &\quad - \mu(\boldsymbol{r}') \partial'_\alpha \hat{j}^\alpha_\rho(\boldsymbol{r}') - \frac{\hat{\rho}(\boldsymbol{r}')}{m} \partial'_\alpha V(\boldsymbol{r}') u^\alpha(\boldsymbol{r}') \Big) \Big] \Big\}, \end{aligned} \tag{2.49}$$

where $\mathrm{Tr}\{...\}$ is the trace over all the degrees of freedom and the symbol ∂' represents the derivative w.r.t. $\boldsymbol{r}'$. Now, integrating by parts, neglecting the contributions at the boundaries[8] and taking the limit $t \to \infty$[9] we obtain the stationary expression for the average of $\hat{A}(\boldsymbol{r})$

$$\begin{aligned} \langle \hat{A}(\boldsymbol{r}) \rangle &= \langle \hat{A}(\boldsymbol{r}) \rangle_{LE} - \int_0^\infty \mathrm{d}t' \int \mathrm{d}\boldsymbol{r}' \Big[\langle \hat{A}(\boldsymbol{r}, t') \hat{J}^\alpha_{\mathcal{H}}(\boldsymbol{r}') \rangle_0 \partial'_\alpha \beta(\boldsymbol{r}') \\ &\quad - \beta \langle \hat{A}(\boldsymbol{r}, t') \hat{J}^{\alpha\gamma}_j(\boldsymbol{r}') \rangle_0 \partial'_\gamma u^\alpha(\boldsymbol{r}') - \langle \hat{A}(\boldsymbol{r}, t') \hat{j}^\alpha_\rho(\boldsymbol{r}') \rangle_0 \partial'_\alpha [\beta\mu](\boldsymbol{r}') \\ &\quad + \partial'_\alpha V(\boldsymbol{r}') \langle \hat{A}(\boldsymbol{r}, t') \hat{\rho}(\boldsymbol{r}') \rangle_0 \frac{u^\alpha(\boldsymbol{r}')}{m} \Big], \end{aligned} \tag{2.50}$$

where we have shifted the time dependence on the observable $\hat{A}(\boldsymbol{r})$ performing the canonical transformation $\mathcal{U}(-t')$ and we have retained only the linear contributions in Equation 2.49.
Looking at Equation 2.50 an important feature of the stationary averages

[8] Thus, we are assuming that the dynamic correlation functions between $\hat{A}(\boldsymbol{r})$ and the current operators rapidly decay in space.
[9] Where the stationary state is expected to be reached.

here discussed can be noticed: In addition to the local thermal equilibrium contribution, further corrections appear. These corrections are expressed in terms of equilibrium dynamic correlation functions, weighted with the appropriate field and integrated over space and time. Note that in Equation 2.49 the divergences of current operators appear and they are independent of the choice of the contour $\ell_{i\to j}$. Therefore, also the spatial integrals of the dynamic correlation functions appearing in Equation 2.50 do not depend on the definition of the contour. Finally, we can now provide the explicit expressions for the expectation value of the most important quantities.
The formal expression of the average flux of fluid molecules is

$$\begin{aligned}\langle\hat{j}^{\sigma}(\boldsymbol{r})\rangle = \langle\hat{j}^{\sigma}(\boldsymbol{r})\rangle_{LE} - \int_0^{\infty}\mathrm{d}t'\int\mathrm{d}\boldsymbol{r}'\Big[&\langle\hat{j}^{\sigma}(\boldsymbol{r},t')\hat{J}^{\alpha}_{\mathcal{H}}(\boldsymbol{r}')\rangle_0\partial'_{\alpha}\beta(\boldsymbol{r}')\\ &-\beta\langle\hat{j}^{\sigma}(\boldsymbol{r},t')\hat{J}^{\alpha\gamma}_{j}(\boldsymbol{r}')\rangle_0\partial'_{\gamma}u^{\alpha}(\boldsymbol{r}') - \langle\hat{j}^{\sigma}(\boldsymbol{r},t')\hat{j}^{\alpha}_{\rho}(\boldsymbol{r}')\rangle_0\partial'_{\alpha}[\beta\mu](\boldsymbol{r}')\\ &+\partial'_{\alpha}V(\boldsymbol{r}')\langle\hat{j}^{\sigma}(\boldsymbol{r},t')\hat{\rho}(\boldsymbol{r}')\rangle_0\frac{u^{\alpha}(\boldsymbol{r}')}{m}\Big],\end{aligned} \tag{2.51}$$

the average heat flux is

$$\begin{aligned}\langle\hat{J}^{\sigma}_{\mathcal{H}}(\boldsymbol{r})\rangle = \langle\hat{J}^{\sigma}_{\mathcal{H}}(\boldsymbol{r})\rangle_{LE} - \int_0^{\infty}\mathrm{d}t'\int\mathrm{d}\boldsymbol{r}'\Big[&\langle\hat{J}^{\sigma}_{\mathcal{H}}(\boldsymbol{r},t')\hat{J}^{\alpha}_{\mathcal{H}}(\boldsymbol{r}')\rangle_0\partial'_{\alpha}\beta(\boldsymbol{r}')\\ &-\beta\langle\hat{J}^{\sigma}_{\mathcal{H}}(\boldsymbol{r},t')\hat{J}^{\alpha\gamma}_{j}(\boldsymbol{r}')\rangle_0\partial'_{\gamma}u^{\alpha}(\boldsymbol{r}') - \langle\hat{J}^{\sigma}_{\mathcal{H}}(\boldsymbol{r},t')\hat{j}^{\alpha}_{\rho}(\boldsymbol{r}')\rangle_0\partial'_{\alpha}[\beta\mu](\boldsymbol{r}')\\ &+\partial'_{\alpha}V(\boldsymbol{r}')\langle\hat{J}^{\sigma}_{\mathcal{H}}(\boldsymbol{r},t')\hat{\rho}(\boldsymbol{r}')\rangle_0\frac{u^{\alpha}(\boldsymbol{r}')}{m}\Big],\end{aligned} \tag{2.52}$$

the average momentum flux reads

$$\begin{aligned}\langle\hat{J}^{\sigma\delta}_{j}(\boldsymbol{r})\rangle = \langle\hat{J}^{\sigma\delta}_{j}(\boldsymbol{r})\rangle_{LE} - \int_0^{\infty}\mathrm{d}t'\int\mathrm{d}\boldsymbol{r}'\Big[&\langle\hat{J}^{\sigma\delta}_{j}(\boldsymbol{r},t')\hat{J}^{\alpha}_{\mathcal{H}}(\boldsymbol{r}')\rangle_0\partial'_{\alpha}\beta(\boldsymbol{r}')\\ &-\beta\langle\hat{J}^{\sigma\delta}_{j}(\boldsymbol{r},t')\hat{J}^{\alpha\gamma}_{j}(\boldsymbol{r}')\rangle_0\partial'_{\gamma}u^{\alpha}(\boldsymbol{r}') - \langle\hat{J}^{\sigma\delta}_{j}(\boldsymbol{r},t')\hat{j}^{\alpha}_{\rho}(\boldsymbol{r}')\rangle_0\partial'_{\alpha}[\beta\mu](\boldsymbol{r}')\\ &+\partial'_{\alpha}V(\boldsymbol{r}')\langle\hat{J}^{\sigma\delta}_{j}(\boldsymbol{r},t')\hat{\rho}(\boldsymbol{r}')\rangle_0\frac{u^{\alpha}(\boldsymbol{r}')}{m}\Big],\end{aligned} \tag{2.53}$$

while the average of the mass density results

$$\begin{aligned}\langle\hat{\rho}(\boldsymbol{r})\rangle = \langle\hat{\rho}(\boldsymbol{r})\rangle_{LE} - \int_0^{\infty}\mathrm{d}t'\int\mathrm{d}\boldsymbol{r}'\Big[&\langle\hat{\rho}(\boldsymbol{r},t')\hat{J}^{\alpha}_{\mathcal{H}}(\boldsymbol{r}')\rangle_0\partial'_{\alpha}\beta(\boldsymbol{r}')\\ &-\beta\langle\hat{\rho}(\boldsymbol{r},t')\hat{J}^{\alpha\gamma}_{j}(\boldsymbol{r}')\rangle_0\partial'_{\gamma}u^{\alpha}(\boldsymbol{r}') - \langle\hat{\rho}(\boldsymbol{r},t')\hat{j}^{\alpha}_{\rho}(\boldsymbol{r}')\rangle_0\partial'_{\alpha}[\beta\mu](\boldsymbol{r}')\\ &+\partial'_{\alpha}V(\boldsymbol{r}')\langle\hat{\rho}(\boldsymbol{r},t')\hat{\rho}(\boldsymbol{r}')\rangle_0\frac{u^{\alpha}(\boldsymbol{r}')}{m}\Big].\end{aligned} \tag{2.54}$$

2.2.3 Constraints for the external fields

The expressions reported above are particularly important because allow to compute the averages of the relevant observables for a system out of equilibrium. However the time-independent fields $\beta(\boldsymbol{r})$, $\mu(\boldsymbol{r})$ and $\boldsymbol{u}(\boldsymbol{r})$ appear in these expressions and they have not been fixed yet, but they can not be determined *a priori*. In order to understand this point let us consider a fluid in a channel. To create a thermal gradient $\boldsymbol{\nabla}\beta(\boldsymbol{r})$ inside it we can control the the temperature of the two extremities of the channel, but we can not have a direct control on the temperature profile. On the contrary, it will be self-consistently determined by the fluid, as well as the chemical potential profile and the velocity field[10].
In order to obtain the expressions of these fields we can make use of the continuity equation for the average local density $\langle\hat{\mathcal{H}}(\boldsymbol{r})\rangle$, the local momentum density $\langle\hat{j}^{\gamma}(\boldsymbol{r})\rangle$ and the local particle density $\langle\hat{\rho}(\boldsymbol{r})\rangle$, and impose the stationary condition:

$$\partial_{\gamma}\langle\hat{j}^{\gamma}(\boldsymbol{r})\rangle = 0\,, \tag{2.55}$$

$$\partial_{\gamma}\langle\hat{J}^{\gamma}_{\mathcal{H}}(\boldsymbol{r})\rangle = 0\,, \tag{2.56}$$

$$\partial_{\gamma}\langle\hat{J}^{\alpha\gamma}_{j}(\boldsymbol{r})\rangle = -\frac{\langle\hat{\rho}(\boldsymbol{r})\rangle}{m}\partial_{\alpha}V(\boldsymbol{r})\,. \tag{2.57}$$

The solution of this set of five independent differential equations formally provides the expressions of the gradients of the fields: $\partial_{\alpha}\beta(\boldsymbol{r})$, $\partial_{\alpha}\mu(\boldsymbol{r})$ and $\partial_{\alpha}u^{\gamma}(\boldsymbol{r})$. Unfortunately, without further approximations the general solution of this system can not be obtained in closed form. On the other hand, when the equations are specialized to some simple geometry, symmetry considerations allow to considerably simplify the problem.
In the following we will restrict our results to the so called slit (or slab) geometry, shown in Figure 2.1, where a fluid fills the region between two infinite parallel planar walls, placed at fixed distance h. Furthermore we impose that the walls behave as an external potential constant in the x and y direction, i.e. $V(\boldsymbol{r}) = V(z)$, and the fluid is kept out of equilibrium applying a temperature difference in the x-direction. The temperature difference is set at infinity and in such a way that the gradient is small and finite. On the basis of the simple geometry of the problem, we expect that the solutions of the system consisting of Equations 2.55, 2.56, 2.57 will show some additional properties. Here we will assume these properties and then we will show that such a solution exists. The assumptions on the solutions are the following:

- The gradient of the field $\beta(\boldsymbol{r})$ is uniform throughout the fluid and is set only in the x-direction

$$\boldsymbol{\nabla}\beta(\boldsymbol{r}) = (\partial_{x}\beta, 0, 0) \tag{2.58}$$

[10] As will be clear later, the velocity field $\boldsymbol{u}(\boldsymbol{r})$ arises if the fluid is not homogeneous.

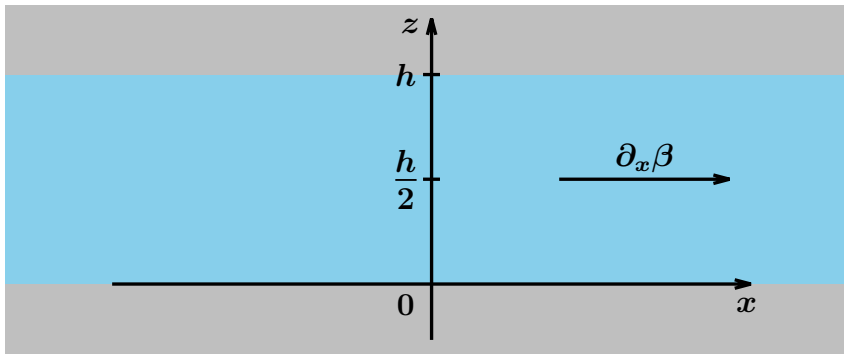

Figure 2.1: Schematic representation of the slab geometry: Fluid particles occupy the light blue region, while the grey ones represent the confinements. The y direction is perpendicular to the plane of the sheet.

being $\partial_x \beta$ constant.

- The gradient of the field $\mu(\boldsymbol{r})$ is uniform throughout the fluid and is set only in the x-direction

$$\boldsymbol{\nabla}\mu(\boldsymbol{r}) = (\partial_x \mu, 0, 0) \tag{2.59}$$

being $\partial_x \mu$ constant. Let us now consider the field $\beta(\boldsymbol{r})\mu(\boldsymbol{r})$ and let us apply these first two assumptions to write it as

$$(\beta + \partial_x \beta\, x)\,(\mu + \partial_x \mu\, x) = \beta\mu + \partial_x\,(\beta\mu)\; x + \partial_x \beta \partial_x \mu\, x^2\,, \tag{2.60}$$

Being $\partial_x\,(\beta\mu)$ constant. But, within linear response theory, that is considering only terms linear in the gradients of the fields, we can state

$$\boldsymbol{\nabla}\,[\beta\mu]\,(\boldsymbol{r}) = (\partial_x\,(\beta\mu)\,, 0, 0)\,. \tag{2.61}$$

- The only non-vanishing component of the velocity field is along the x-axis and is dependent only on the coordinate z normal to the wall

$$\boldsymbol{u}(\boldsymbol{r}) = (u^x(z), 0, 0)\;. \tag{2.62}$$

In the following we will check the consistency of these assumptions by showing that they indeed provide a solution of the conservation laws 2.55, 2.56 and 2.57.
At this scope it is useful to review the symmetry properties characterizing systems in a planar geometry.

Symmetries in planar systems

Under the hypotheses introduced above, the system is invariant along the x and y-directions, when held at a constant temperature. Therefore the equilibrium averages evaluated by means of the underlying equilibrium distribution F^{eq} do not depend on that coordinates. To give an example, the average equilibrium density profile $\langle\hat{\rho}(\boldsymbol{r})\rangle$ depends only on the coordinate orthogonal to the walls z. Obviously, the thermal gradient along the x direction introduces an additional dependence of the averages on x.

Furthermore, any second-rank tensor representing a physical quantity and belonging to systems characterized by a broken symmetry along a single direction, let us say z as in our case, reads

$$T^{\alpha\beta} = a\,\delta^{\alpha\beta} + b\,\hat{\boldsymbol{z}}^{\alpha}\hat{\boldsymbol{z}}^{\beta}, \tag{2.63}$$

because it has to preserve the symmetry of the system. In Equation 2.63 a and b are constants, possibly position dependent if the tensor is a tensor field, and $\hat{\boldsymbol{z}}$ is the unit vector along the z-direction. This peculiar expression is motivated by the symmetry properties of its terms: The identity tensor has no intrinsic symmetry whereas the product between the unit versors $\hat{\boldsymbol{z}}\hat{\boldsymbol{z}}$ owns the symmetry of the problem. Equation 2.63 is the most general expression for a second-rank tensor that we can obtain combining the delta function and the unit versor $\hat{\boldsymbol{z}}$, which are the unique tensors preserving the symmetries of the system.
It follows that in planar symmetry the equilibrium momentum flux tensor is diagonal and is determined by two different non-vanishing components:

$$\overline{\overline{p}}(z) = \begin{bmatrix} p_{\mathrm{T}}(z) & 0 & 0 \\ 0 & p_{\mathrm{T}}(z) & 0 \\ 0 & 0 & p_{\mathrm{N}}(z) \end{bmatrix},$$

where p_{T} and p_{N} are referred to as the tangential and the normal pressure respectively. According to the notation introduced in Equation 2.63, $a = p_{\mathrm{T}}(z)$ and $b = p_{\mathrm{N}}(z) - p_{\mathrm{T}}(z)$.
In the following we will deal with expressions as

$$I^{\alpha\gamma} = \int \mathrm{d}\boldsymbol{r}'\, T^{\alpha\gamma}(\boldsymbol{r}'), \tag{2.64}$$

where $T^{\alpha\gamma}(\boldsymbol{r})$ is second-rank tensor. Now let us impose that the tensor $T^{\alpha\gamma}(\boldsymbol{r})$ is invariant under a given coordinate transformation $\mathcal{R}$, represented by a matrix belonging to the orthogonal group $\mathscr{O}(3)$

$$T^{\alpha\gamma}(R\boldsymbol{r}) = R^{\alpha\sigma}R^{\gamma\delta}T^{\sigma\delta}(\boldsymbol{r}).$$

It follows that the integral must obey the following property

$$I^{\alpha\gamma} = R^{\alpha\sigma}R^{\gamma\delta}I^{\gamma\delta}, \tag{2.65}$$

because the Jacobian of the transformation is equal to 1. Then, if T is invariant under all the rotations belonging to $\mathscr{O}(3)$ it follows, due to Schur's lemma, that the tensor $I^{\alpha\gamma} = a\delta^{\alpha\gamma}$. However, if T is invariant under a subset of $\mathscr{O}(3)$, e.g. the rotations about the z-axis, Equation 2.65 is fulfilled only if the $I^{\alpha\gamma}$ has the form (2.63).
Following the same argument adopted in the construction of the second-rank tensor, it is possible to show that a third-rank tensor endowed with the same symmetries reads

$$T^{\alpha\beta\gamma} = a_1\,\delta^{\alpha\beta}\hat{\boldsymbol{z}}^{\gamma} + a_2\,\delta^{\alpha\gamma}\hat{\boldsymbol{z}}^{\beta} + a_3\,\delta^{\gamma\beta}\hat{\boldsymbol{z}}^{\alpha} + b\,\hat{\boldsymbol{z}}^{\alpha}\hat{\boldsymbol{z}}^{\beta}\hat{\boldsymbol{z}}^{\gamma}. \tag{2.66}$$

These symmetries properties in planar systems will be used in the following, where we will check the consistency of assumptions 2.58-2.62 by showing that they indeed provide a solution of the conservation laws of the mass, the energy and the momentum.

Mass and energy conservation laws

Due to the symmetries of the system, it turns out that the steady-state conservation law for the mass density and for the energy density, expressed in Equations 2.55 and 2.56, are identically satisfied. In order to show it, let us apply the assumptions introduced above to the average value of the momentum density expressed in Equation 2.51:

$$\begin{aligned}\langle\hat{j}^{\alpha}(\boldsymbol{r})\rangle = {} & \langle\hat{\rho}(z)\rangle_0 u^x(z)\delta^{\alpha x} \\ & + \int_0^{\infty}\mathrm{d}t'\int\mathrm{d}\boldsymbol{r}'\Big[\langle\hat{j}^{\alpha}(\boldsymbol{r},t')\hat{J}^x_{\mathcal{H}}(\boldsymbol{r}')\rangle_0\partial'_x\beta - \beta\langle\hat{j}^{\alpha}(\boldsymbol{r},t')\hat{J}^{xz}_{j}(\boldsymbol{r}')\rangle_0\partial'_z u^x(z') \\ & - \langle\hat{j}^{\alpha}(\boldsymbol{r},t')\hat{j}^x_{\rho}(\boldsymbol{r}')\rangle_0\partial'_x(\beta\mu)\Big]\end{aligned} \tag{2.67}$$

where we only made use of the assumptions introduced above. Note that the contribution to the averages given by the external potential $V(z)$ vanishes, because it enters in the expressions multiplied to the velocity profile in the form

$$\partial_{\alpha}V(\boldsymbol{r})u^{\alpha}(\boldsymbol{r}) \tag{2.68}$$

which results to be zero due to the assumption made on $\boldsymbol{u}(\boldsymbol{r})$ and $V(\boldsymbol{r})$. Moreover, due to the symmetry properties of the equilibrium system, only the

x component of the average momentum density is non-vanishing:

$$\langle \hat{j}^y(\boldsymbol{r})\rangle = 0 \tag{2.69}$$

$$\langle \hat{j}^z(\boldsymbol{r})\rangle = 0 \tag{2.70}$$

$$\begin{aligned}\langle \hat{j}^x(\boldsymbol{r})\rangle = {}& \langle\hat{\rho}(z)\rangle_0 u^x(z) \\ &+ \int_0^\infty \mathrm{d}t' \int \mathrm{d}\boldsymbol{r}' \Big[\langle \hat{j}^x(\boldsymbol{r},t')\hat{J}^x_{\mathcal{H}}(\boldsymbol{r}')\rangle_0 \partial'_x\beta \\ &- \beta\langle \hat{j}^x(\boldsymbol{r},t')\hat{J}^{xz}_j(\boldsymbol{r}')\rangle_0 \partial'_z u^x(z') \\ &- \langle \hat{j}^x(\boldsymbol{r},t')\hat{j}^x_\rho(\boldsymbol{r}')\rangle_0 \partial'_x(\beta\mu)\Big] .\end{aligned} \tag{2.71}$$

Therefore the stationary condition for the mass density reads

$$\begin{aligned}0 &= \partial_\alpha \langle \hat{j}^\alpha(\boldsymbol{r})\rangle \\ &= \partial_x \langle \hat{j}^x(\boldsymbol{r})\rangle \\ &= \partial_x \int_0^\infty \mathrm{d}t' \int \mathrm{d}\boldsymbol{r}' \Big[\langle \hat{j}^x(\boldsymbol{r},t')\hat{J}^x_{\mathcal{H}}(\boldsymbol{r}')\rangle_0 \partial'_x\beta \\ &\quad - \beta\langle \hat{j}^x(\boldsymbol{r},t')\hat{J}^{xz}_j(\boldsymbol{r}')\rangle_0 \partial'_z u^x(z') - \langle \hat{j}^x(\boldsymbol{r},t')\hat{j}^x_\rho(\boldsymbol{r}')\rangle_0 \partial'_x(\beta\mu)\Big] .\end{aligned} \tag{2.72}$$

The two-point correlation functions only depend on the difference $x - x'$, z and z', because the averages are evaluated at equilibrium and thus the system is homogeneous along the coordinate x. Therefore their integral over $\boldsymbol{r}'$ will be independent of x and its derivative vanishes. The same considerations apply also for the continuity equation for $\langle\hat{\mathcal{H}}(\boldsymbol{r})\rangle$: Only the component of the flux along the x direction is different from zero:

$$\langle \hat{J}^y_{\mathcal{H}}(\boldsymbol{r})\rangle = 0 \tag{2.73}$$

$$\langle \hat{J}^z_{\mathcal{H}}(\boldsymbol{r})\rangle = 0 \tag{2.74}$$

$$\begin{aligned}\langle \hat{J}^x_{\mathcal{H}}(\boldsymbol{r})\rangle = {}& \beta \int \mathrm{d}\boldsymbol{r}' \langle \hat{J}^x_{\mathcal{H}}(\boldsymbol{r})\hat{j}^x(\boldsymbol{r}')\rangle_0 u^x(z) \\ &+ \int_0^\infty \mathrm{d}t' \int \mathrm{d}\boldsymbol{r}' \Big[\langle \hat{J}^x_{\mathcal{H}}(\boldsymbol{r},t')\hat{J}^x_{\mathcal{H}}(\boldsymbol{r}')\rangle_0 \partial'_x\beta \\ &- \beta\langle \hat{J}^x_{\mathcal{H}}(\boldsymbol{r},t')\hat{J}^{xz}_j(\boldsymbol{r}')\rangle_0 \partial'_z u^x(z') \\ &- \langle \hat{J}^x_{\mathcal{H}}(\boldsymbol{r},t')\hat{j}^x_\rho(\boldsymbol{r}')\rangle_0 \partial'_x(\beta\mu)\Big]\end{aligned} \tag{2.75}$$

and, as before, the continuity equation, which in the stationary limit reduces to the derivative w.r.t. x of $\langle \hat{J}^x_{\mathcal{H}}(\boldsymbol{r})\rangle$, is identically satisfied because the integral of the correlation functions does not depend on x.

Momentum conservation law

The stationary condition expressed by Equation 2.57 leads to three independent equations. Two of them are identically satisfied, as in the case of the

mass and energy density continuity equations, while the last one defines the gradient of the velocity profile.
Let us start with the conservation law for $\langle \hat{j}^z(\boldsymbol{r})\rangle$. The αz-component of the momentum current which enters the stationary conservation of momentum density reads

$$\begin{aligned}
\langle \hat{J}_j^{\alpha z}(\boldsymbol{r})\rangle &= \langle \hat{J}_j^{\alpha z}(\boldsymbol{r})\rangle_{LE} \\
&\quad + \int_0^\infty \mathrm{d}t' \int \mathrm{d}\boldsymbol{r}' \Big[\langle \hat{J}_j^{\alpha z}(\boldsymbol{r},t') \hat{J}^x_{\mathcal{H}}(\boldsymbol{r}')\rangle_0 \partial'_x \beta \\
&\quad - \beta \langle \hat{J}_j^{\alpha z}(\boldsymbol{r},t') \hat{J}_j^{xz}(\boldsymbol{r}')\rangle_0 \partial'_z u^x(z') \\
&\quad - \langle \hat{J}_j^{\alpha z}(\boldsymbol{r},t') \hat{j}^x_\rho(\boldsymbol{r}')\rangle_0 \partial'_x(\beta\mu) \Big] \\
&= \langle \hat{J}_j^{\alpha z}(\boldsymbol{r})\rangle_{LE} \\
&\quad + \delta^{\alpha x} \int_0^\infty \mathrm{d}t' \int \mathrm{d}\boldsymbol{r}' \Big[\langle \hat{J}_j^{xz}(\boldsymbol{r},t') \hat{J}^x_{\mathcal{H}}(\boldsymbol{r}')\rangle_0 \partial'_x \beta \\
&\quad - \beta \langle \hat{J}_j^{xz}(\boldsymbol{r},t') \hat{J}_j^{xz}(\boldsymbol{r}')\rangle_0 \partial'_z u^x(z') \\
&\quad - \langle \hat{J}_j^{xz}(\boldsymbol{r},t') \hat{j}^x_\rho(\boldsymbol{r}')\rangle_0 \partial'_x(\beta\mu) \Big]
\end{aligned} \tag{2.76}$$

where the last equality follows from the usual symmetry properties. The term proportional to the Kronecker delta does not depend on x, because the correlation functions only depend on $x - x'$, and a suitable change of variable in the integral makes it independent of x. The Local equilibrium contribution $\langle \hat{J}_j^{\alpha z}(\boldsymbol{r})\rangle_{LE}$ for the considered planar symmetry has not been specified yet. Applying the usual assumptions to the general definition of $\langle \hat{J}_j^{\alpha z}(\boldsymbol{r})\rangle_{LE}$ given in Equation 2.45 we obtain

$$\begin{aligned}
\langle \hat{J}_j^{\alpha z}(\boldsymbol{r})\rangle_{LE} &= \langle \hat{J}_j^{\alpha z}(\boldsymbol{r})\rangle_0 \\
&\quad - \partial_x \beta \int \mathrm{d}\boldsymbol{r}' x' \left[\langle \hat{J}_j^{\alpha z}(\boldsymbol{r}) \hat{\mathcal{H}}(\boldsymbol{r}')\rangle_0 - \mu \langle \hat{J}_j^{\alpha z}(\boldsymbol{r}) \hat{\rho}(\boldsymbol{r}')\rangle_0 \right] \\
&\quad + \beta \partial_x \mu \int \mathrm{d}\boldsymbol{r}' x' \langle \hat{J}_j^{\alpha z}(\boldsymbol{r}) \hat{\rho}(\boldsymbol{r}')\rangle_0 + \mathcal{C}_{\mathcal{Q}} \langle \hat{J}_j^{\alpha z}(\boldsymbol{r})\rangle_0 \,.
\end{aligned} \tag{2.77}$$

The quantity $\langle \hat{J}_j^{yz}(\boldsymbol{r})\rangle_{LE}$ is equal to 0, because on one side the equilibrium pressure tensor is diagonal (thus $\langle \hat{J}_j^{yz}(\boldsymbol{r})\rangle_0 = 0$) and on the other side the linear corrections, which are integrated along $\boldsymbol{r}'$, vanishes due to the symmetry properties of the system. On the other hand $\langle \hat{J}_j^{xz}(\boldsymbol{r})\rangle_{LE}$ is different from zero due to the presence of the linear contributions in the derivatives of the fields in Equation 2.77. Furthermore this term depends on z , but not on x: The

integrals in the definition of $\langle \hat{J}_j^{xz}(\boldsymbol{r})\rangle_{LE}$ can be rearranged as

$$\begin{aligned}\int \mathrm{d}\boldsymbol{r}' x' \langle \hat{J}_j^{xz}(\boldsymbol{r})\hat{\mathcal{O}}(\boldsymbol{r}')\rangle_0 &= \int \mathrm{d}\boldsymbol{r}'(x'-x)\langle \hat{J}_j^{xz}(\boldsymbol{r})\hat{\mathcal{O}}(\boldsymbol{r}')\rangle_0 \\ &\quad + x\int \mathrm{d}\boldsymbol{r}'\langle \hat{J}_j^{xz}(\boldsymbol{r})\hat{\mathcal{O}}(\boldsymbol{r}')\rangle_0 \\ &= \int \mathrm{d}\boldsymbol{r}'(x'-x)\langle \hat{J}_j^{xz}(\boldsymbol{r})\hat{\mathcal{O}}(\boldsymbol{r}')\rangle_0 \,,\end{aligned} \tag{2.78}$$

where $\hat{\mathcal{O}}(\boldsymbol{r})$ is one of the scalar operator appearing in Equation 2.77. We remark that the correlation function $\langle \hat{J}_j^{xz}(\boldsymbol{r})\hat{\mathcal{O}}(\boldsymbol{r}')\rangle_0$ depends on z, z' and $x-x'$. We can thus write the xz-component of the LE pressure as

$$\begin{aligned}\langle \hat{J}_j^{xz}(\boldsymbol{r})\rangle_{LE} = \int \mathrm{d}\boldsymbol{r}'(x-x')\Big[&\partial_x\beta\langle \hat{J}_j^{xz}(\boldsymbol{r})\hat{\mathcal{H}}(\boldsymbol{r}')\rangle_0 \\ &- \partial_x(\beta\mu)\langle \hat{J}_j^{xz}(\boldsymbol{r})\hat{\rho}(\boldsymbol{r}')\rangle_0\Big] \,.\end{aligned} \tag{2.79}$$

Finally, the continuity equation we are considering involves also the LE average of the zz-component of the momentum flux, which can be written as

$$\langle \hat{J}_j^{zz}(\boldsymbol{r})\rangle_{LE} = p_N(z)\Big|_{\beta(x),\mu(x)} \,, \tag{2.80}$$

and this quantity depends both on z and x, because the equilibrium averages are evaluated at the local value of the temperature and the chemical potential. At this point we can express the stationarity condition for the z component of the momentum density:

$$\begin{aligned}\partial_\alpha \langle \hat{J}_j^{\alpha z}(\boldsymbol{r})\rangle &= \partial_z p_N(z)\Big|_{\beta(x),\mu(x)} \\ &\quad - \frac{\rho(z)}{m}\Big|_{\beta(x),\mu(x)}\partial_z V(z) \,,\end{aligned} \tag{2.81}$$

where $\rho(z)$ is the equilibrium density profile evaluated at the local $\beta(x)$ and $\mu(x)$, while if hard walls are considered $\partial_z V(z)$ vanishes[11]. Equation 2.81, the so called hydrostatic equilibrium condition, is identically fulfilled by the normal component of the pressure tensor for every choice of β and μ and then at each value of the x-coordinate. Note that for hard walls it implies that the normal pressure is constant along z and equals the bulk pressure p at the local temperature $\beta(x)$ and chemical potential $\mu(x)$. However, regardless of $V(z)$ Equation 2.81 implies that the normal pressure depends on x.
The stationarity condition for $\langle \hat{j}^y(\boldsymbol{r})\rangle$ is identically satisfied because of the symmetry of the problem which implies $\partial_\alpha \langle \hat{J}_j^{\alpha y}(\boldsymbol{r})\rangle = 0$.

[11] With hard walls $V(z) = \infty$ for $z < 0$ and $z > h$, while it is equal to 0 in the fluid region.

The most interesting continuity equation comes from the conservation of the x-component of the momentum density $\langle \hat{j}^x(\boldsymbol{r})\rangle$:

$$\begin{aligned}\partial_\alpha \langle \hat{J}_j^{\alpha x}(\boldsymbol{r})\rangle &= \partial_x \langle \hat{J}_j^{xx}(\boldsymbol{r})\rangle + \partial_z \langle \hat{J}_j^{xz}(\boldsymbol{r})\rangle \\ &= 0\,,\end{aligned} \tag{2.82}$$

and it is immediate to show that the relevant terms in this relation are

$$\begin{aligned}\langle \hat{J}_j^{\alpha x}(\boldsymbol{r})\rangle = \langle \hat{J}_j^{\alpha x}(\boldsymbol{r})\rangle_{LE} &\\ + \int_0^\infty \mathrm{d}t' \int \mathrm{d}\boldsymbol{r}' \Big[&\langle \hat{J}_j^{xz}(\boldsymbol{r},t')\hat{J}^x_{\mathcal{H}}(\boldsymbol{r}')\rangle_0 \partial'_x \beta \\ - \beta \langle \hat{J}_j^{xz}(\boldsymbol{r},t')\hat{J}_j^{xz}(\boldsymbol{r}')\rangle_0 &\partial'_z u^x(z') \\ - \langle \hat{J}_j^{xz}(\boldsymbol{r},t')\hat{j}^x_\rho(\boldsymbol{r}')\rangle_0 &\partial'_x(\beta\mu)\Big]\,,\end{aligned} \tag{2.83}$$

where $\langle \hat{J}_j^{zx}(\boldsymbol{r})\rangle_{LE}$ has been evaluated in Equation 2.79, $\langle \hat{J}_j^{yx}(\boldsymbol{r})\rangle_{LE}$ is equal to 0 and

$$\langle \hat{J}_j^{\alpha x}(\boldsymbol{r})\rangle_{LE} = p_T(z)\Big|_{\beta(x),\mu(x)}\,. \tag{2.84}$$

Note that also the tangential pressure p_T acquires a dependence on x because the equilibrium averages are evaluated at $\beta(x)$ and $\mu(x)$. We can now express the stationarity condition for the x-component of the momentum density:

$$\begin{aligned}0 = \partial_x p_T(z)\Big|_{\beta(x),\mu(x)} &\\ + \partial_z \int \mathrm{d}\boldsymbol{r}'(x-x')\Big[&\partial'_x \beta \langle \hat{J}_j^{xz}(\boldsymbol{r})\hat{\mathcal{H}}(\boldsymbol{r}')\rangle_0 - \partial'_x(\beta\mu)\langle \hat{J}_j^{xz}(\boldsymbol{r})\hat{\rho}(\boldsymbol{r}')\rangle_0\Big] \\ + \partial_z \int_0^\infty \mathrm{d}t' \int \mathrm{d}\boldsymbol{r}' \Big[&\langle \hat{J}_j^{xz}(\boldsymbol{r},t')\hat{J}^x_{\mathcal{H}}(\boldsymbol{r}')\rangle_0 \partial'_x \beta \\ - \beta \langle \hat{J}_j^{xz}(\boldsymbol{r},t')\hat{J}_j^{xz}(\boldsymbol{r}')\rangle_0 &\partial'_z u^x(z') - \langle \hat{J}_j^{xz}(\boldsymbol{r},t')\hat{j}^x_\rho(\boldsymbol{r}')\rangle_0 \partial'_x(\beta\mu)\Big]\,.\end{aligned} \tag{2.85}$$

Equation 2.85 defines an integro-differential equation for the velocity profile $u^x(z)$.
In order to make further progress we have to better specify the nature of the slit and employ the appropriate boundary conditions. For example, in an open channel a free flow develops imposing equal bulk pressure at the left and right (in the x direction) boundaries. If the channel is closed the fluid can not flow through the slit and a bulk pressure gradient develops in order to fulfill the mass conservation law.

2.3 OPEN CHANNEL

Let us now consider an infinitely long channel, as the one reported in Figure 2.1, where a free flow develops and let us consider its height h large enough to

guarantee that the fluid properties in the central region of the channel are not conditioned by perturbations due to the walls. In this region ($z \sim h/2$) the fluid can be considered homogeneous and isotropic, thus the normal and the tangential components of the pressure tensor are equal and reduce to the bulk pressure p of the fluid, evaluated at the local value of the fields $\beta(x)$ and $\mu(x)$:

$$p_N\left(z \sim \frac{h}{2}\right)\Big|_{\beta(x),\mu(x)} = p_T\left(z \sim \frac{h}{2}\right)\Big|_{\beta(x),\mu(x)} = p\big|_{\beta(x),\mu(x)}\,. \tag{2.86}$$

The free flow in an open channel imposes equal bulk pressure at the left and the right boundaries. It means that the temperature and chemical potential fields will adapt in order to guarantee this condition:

$$\begin{aligned} 0 &= \partial_x p\big|_{\beta(x),\mu(x)} \\ &= \partial_x \beta \left[\partial_\beta p + \frac{\partial_x \mu}{\partial_x \beta}\partial_\mu p\right]\,. \end{aligned} \tag{2.87}$$

This equation fixes the ratio between the temperature and the chemical potential gradients, which can be expressed in terms of thermodynamic quantities as

$$\begin{aligned} \frac{\partial_x \mu}{\partial_x \beta} &= -\frac{\partial_\beta p}{\partial_\mu p} \\ &= \frac{sT}{\beta\rho}\,, \end{aligned} \tag{2.88}$$

where s is the entropy density and we made use of the thermodynamic relations

$$\begin{aligned} \partial_T p\big|_\mu &= -\partial_T\left(\frac{\Omega}{V}\right)\Big|_\mu \\ &= s \\ \partial_\mu p\big|_T &= -\partial_\mu\left(\frac{\Omega}{V}\right)\Big|_T \\ &= \rho\,, \end{aligned} \tag{2.89}$$

where Ω is the grand potential and its derivatives have been evaluated at constant volume V. Now we can express the $\partial_x(\beta\mu)$ in a more suggestive way:

$$\partial_x(\beta\mu) = \partial_x\beta\left(\mu + T\frac{s}{\rho}\right) = \partial_x\beta\frac{u+p}{\rho} = \partial_x h_m\,, \tag{2.90}$$

being u the internal energy density and h_m the enthalpy per unit mass. Note that this use of (macroscopic) thermodynamics relations does not introduce any ambiguity, because they are applied in the central region of the fluid, where it supposed to be homogeneous.

This expression of $\partial_x(\beta\mu)$ allows to straightforwardly integrate along z the stationary condition expressed in Equation 2.85. This integration is performed from $h/2$ to z. Note that two terms in Equation 2.85 can be integrated analytically. Moreover the integrals vanish at $z = h/2$ where the fluid acquires bulk properties. Therefore the integro-differential equation for the velocity profile can be written as

$$\int_0^h \mathrm{d}z' \mathcal{K}(z,z') \partial'_z u^x(z') = \partial_x \beta \mathcal{S}(z)\,, \tag{2.91}$$

where the kernel $\mathcal{K}(z,z')$ is related to the local viscosity of the fluid

$$\mathcal{K}(z,z') = \beta \int_0^\infty \mathrm{d}t' \int \mathrm{d}\boldsymbol{r}'_\perp \langle \hat{J}_j^{xz}(\boldsymbol{r},t') \hat{J}_j^{xz}(\boldsymbol{r}') \rangle_0 \tag{2.92}$$

and $\mathcal{S}(z)$ is the source therm of the thermo-osmotic mass flow in an open channel and can be written as the sum of a static contribution $\mathcal{S}_s(z)$ and a dynamic one $\mathcal{S}_d(z)$[12]:

$$\mathcal{S}(z) = \mathcal{S}_s(z) + \mathcal{S}_d(z)\,, \tag{2.93}$$

$$\mathcal{S}_s(z) = \int_{\frac{h}{2}}^z \mathrm{d}z' \frac{\partial p_T(z')}{\partial \beta}\Big|_p - \int \mathrm{d}\boldsymbol{r}' (x-x') \langle \hat{J}_j^{xz}(\boldsymbol{r}) \hat{\mathcal{P}}(\boldsymbol{r}') \rangle_0\,, \tag{2.94}$$

$$\mathcal{S}_d(z) = \int_0^\infty \mathrm{d}t' \int \mathrm{d}\boldsymbol{r}' \langle \hat{J}_j^{xz}(\boldsymbol{r},t') \hat{J}_Q^{x}(\boldsymbol{r}') \rangle_0\,. \tag{2.95}$$

Here we have introduced the operator $\hat{\mathcal{P}}(\boldsymbol{r}) = h_m \hat{\rho}(\boldsymbol{r}) - \hat{\mathcal{H}}(\boldsymbol{r})$ and the operator $\hat{J}_Q^\alpha(\boldsymbol{r}) = \hat{J}_\mathcal{H}^\alpha(\boldsymbol{r}) - h_m \hat{j}_\rho^\alpha(\boldsymbol{r})$ which can be interpreted as the microscopic heat flux[13]. In Equation 2.94 the tangential pressure has been rewritten as a function of the temperature field $\beta(x)$ and of the bulk pressure p. Indeed we can write

$$p_T\left(\frac{h}{2}\right)\Big|_{\beta(x),\mu(x)} = p \tag{2.96}$$

for each value of the coordinate x and we can replace the dependence on the local chemical potential with the bulk pressure:

$$\partial_x p_T(z)\big|_{\beta(x),p} = \frac{\partial p_T(z)}{\partial \beta}\Big|_p \partial_x \beta\,. \tag{2.97}$$

The solution of this set of equations provides the gradient $\partial_z u^x(z)$, which does not have a direct physical meaning. The real flow is instead defined by the

[12]Static and Dynamic because they are expressed respectively as static and dynamic correlation functions at equilibrium.

[13]Note that this definition of the heat flux does not correspond to its microscopic counterpart introduced within classical hydrodynamics. See for example [42].

average value of the mass current expressed by Equation 2.71, which in an open channel reads

$$\begin{aligned}\langle \hat{j}^x(z)\rangle = \rho(z)u^x(z) \\ + \int_0^\infty \mathrm{d}t' \int \mathrm{d}\boldsymbol{r}' \Big[\langle \hat{j}^x(\boldsymbol{r},t')\hat{J}_Q^x(\boldsymbol{r}')\rangle_0 \partial_x \beta \\ -\beta \langle \hat{j}^x(\boldsymbol{r},t')\hat{J}_j^{xz}(\boldsymbol{r}')\rangle_0 \partial'_x u^x(z') \Big] \,.\end{aligned} \tag{2.98}$$

The mass flux can not be fully determined by this equation: The velocity field, and not only its derivative, appears in the expression. Thus a full knowledge of the mass flow requires to know its value at a given height z, i. e. a physical boundary condition is needed. This point is not a limitation of the theory, but rather a consequence of the Galilean invariance of the problem, which in an experimental set-up is broken by the presence of friction between the fluid and the confining wall [80]. In our model instead $V = V(z)$ and thus the external potential, which describes the confining wall, does not modify the x component of the particles' momenta. One can for example introduce the no-slip boundary condition:

$$\langle \hat{j}^x(0)\rangle_0 = \langle \hat{j}^x(h)\rangle_0 = 0 \,. \tag{2.99}$$

Beyond its quantitative importance, Equation 2.98 clearly shows that the mass flow is an interfacial phenomenon: All the contributions that appear in the Equation vanish in the bulk. In a homogeneous fluid Equation 2.91 admits only a constant solution for $u^x(z)$: The source term vanishes because it involves bulk integrals of odd rank tensors and the derivative of the tangential pressure evaluated at constant bulk pressure (and here $p_T = p_N = p$). Moreover the integral of the mass-heat correlation function vanishes because mass and heat fluctuations are decoupled in the bulk [47][14],[4][15].

This analysis of a model of simple fluid closed to a wall is exact, within linear response theory, and proves that two distinct mechanisms give rise to thermo-osmosis. Both these mechanisms are related to interface physics: The presence of anisotropies in the pressure tensor near the wall, $\mathcal{S}_s(z)$ and the role played by the confining surface on the dynamical correlation functions, $\mathcal{S}_d(z)$. Let us now consider two limiting situations where the relative importance of these two mechanisms is totally unbalanced.

[14] See section 49.
[15] See Section 12.5.

2.3.1 Thermo-osmosis in liquids

In liquids the theoretical tool for dealing with thermo-osmosis is the nonequilibrium thermodynamics. As discussed in the previous Chapter, the reference result is due to Derjaguin [15, 16], who expressed the slip velocity far from the surface as:

$$v_\infty = \frac{1}{\eta}\int_0^\infty \mathrm{d}z \Delta h(z) \frac{\nabla T}{T} \,. \tag{2.100}$$

Thus the mass flux arises due to the spatial dependence of the local enthalpy density near the surface. Such a macroscopic approach is however not fully satisfactory: Continuum theories, as nonequilibrium thermodynamics, can not account for changes in thermodynamics quantities over length scales of the order of the range of the microscopic interaction[16]. Nevertheless in Equation 2.100 the perturbation induced by the surface on the local enthalpy is taken into account. Moreover, the bulk viscosity appears, without accounting for the effect of the confining surface on it. Furthermore it is interesting to note that, according to Derjaguin's result, the only dynamic quantity that plays a role in thermo-osmosis is the (bulk) viscosity.
Thus Derjaguin's result suggests that the contribution of the dynamical correlations is negligible in the liquid state. There are no evidences of the accuracy of this assumption, but anyway, in order to compare our results with Equation 2.100, we can evaluate Equations 2.91 and 2.98 in the "continuum spirit": To do this we evaluate all the dynamic and static correlation functions in the bulk and we assume that the kernel is a short ranged function:

$$\mathcal{K}(z, z') \sim \eta \delta(z - z') \tag{2.101}$$

being η the bulk viscosity. Under these assumptions the dynamic source term $\mathcal{S}_d(z)$ vanishes, and the static one $\mathcal{S}_s(z)$ retains only the contribution including the anisotropy of the pressure tensor. Thus we obtain a simpler source term

$$\mathcal{S}_{CA}(z) = \int_{\frac{h}{2}}^{z} \mathrm{d}z' \frac{\partial p_T(z')}{\partial \beta}\Big|_p \,, \tag{2.102}$$

where the subscript CA refers to continuum approximation. Also Equation 2.98 results simplified by these assumptions:

$$\langle \hat{j}^x(z) \rangle = \rho(z) u^x(z) \tag{2.103}$$

while the differential equation for the velocity profile reads

$$\partial_z u^x(z) = -\frac{\partial_x \beta}{\eta} \int_z^{\frac{h}{2}} \mathrm{d}z' \frac{\partial p_T(z')}{\partial \beta}\Big|_p \,. \tag{2.104}$$

[16] Similar considerations can be applied also to the result obtained by Ganti et all [32].

The integration of this first-order differential equation needs a boundary condition, as previously explained. To go further let us assume the no-slip boundary condition $\langle \hat{j}^x(0) \rangle = 0$, which implies $u^x(0) = 0$. Once this choice is made, the corresponding mass flux reads

$$\langle \hat{j}^x(z) \rangle = -\rho(z) \frac{\partial_x \beta}{\eta} \int_0^{\frac{h}{2}} \mathrm{d}z' \min(z, z') \frac{\partial p_T(z')}{\partial \beta}\Big|_p , \tag{2.105}$$

where the following change of variables has been performed:

$$\int_0^z \mathrm{d}x \int_0^{\frac{h}{2}} \mathrm{d}y \, f(y) = \int_0^{\frac{h}{2}} dy \, f(y) \int_0^{\min(y,x)} \mathrm{d}x \, . \tag{2.106}$$

In the asymptotic limit, i.e. when h and z are larger than the typical length scale of the correlations ($z \to \infty$ and $h \to \infty$), $\min(z, z') \sim z'$ and the slip velocity can be written as

$$\begin{aligned} v_\infty &= \frac{\langle \hat{j}^x \rangle_\infty}{\rho_b} \\ &= -\frac{\partial_x T}{\eta} \frac{\partial}{\partial T}\Big|_p \int_0^\infty \mathrm{d}z' \, z \, [p_T(z') - p] \\ &= -\frac{\partial_x T}{\eta} \frac{\partial}{\partial T}\Big|_p \int_0^\infty \mathrm{d}z' \, z \Delta p_T(z') \, , \end{aligned} \tag{2.107}$$

where ρ_b is the bulk density of the fluid and the bulk pressure in the integral has been subtracted and does not provide an additional contribution because the derivative is taken at fixed bulk pressure p. This relation for the slip velocity far from the surface can be related to Derjaguin's prediction. To this end, we note that in order to obtain the thermo-osmotic flow expressed in Equation 2.107 we must evaluate the tangential pressure near a hard wall. While the normal pressure has been shown, through the continuity equation for the z component of the momentum density, to be independent of z, the tangential component is not. In the spirit of the local density approximation [36], we can then express $p_T(z)$ at a given $(T(x), [\beta\mu](x))$ in terms of the bulk pressure p at a modified z dependent chemical potential $\beta\mu \to \beta\mu + \psi(z)$. The shift ψ in chemical potential is uniquely fixed by imposing that the density profile $\rho(z)$ coincides with the physical one. Under this assumption the x-derivative of the

tangential pressure in local thermal equilibrium becomes[17]

$$\begin{aligned}\partial_x \left\{ p_T(z)\big|_{T(x),[\beta\mu](x)} \right\} &= \partial_x \left\{ p(z)\big|_{T(x),[\beta\mu](x)+\psi(z)} \right\} \\ &= \frac{\partial p(z)}{\partial T}\Big|_{[\beta\mu](x)} \partial_x T + \frac{\partial p(z)}{\partial [\beta\mu]}\Big|_{T(x)} \partial_x [\beta\mu] \\ &= \frac{h(z)}{T}\partial_x T + \frac{\rho(z)}{\beta}\partial_x [\beta\mu] \\ &= \frac{h(z) - h_m \rho(z)}{T}\partial_x T \,,\end{aligned} \tag{2.108}$$

where, according to the adopted approximation, $p(z)$ and $h(z)$ are the pressure and the enthalpy per unit volume of a homogeneous system at density $\rho(z)$ and the dependence of the thermodynamic variables on $\beta(x)$ and $\mu(x)$ is understood. Finally we can write the slip velocity far from the surface in continuum approximation

$$v_\infty = \frac{1}{\eta}\frac{\partial_x T}{T}\int_0^\infty \mathrm{d}z'\, z\,[h(z') - h_m \rho(z')]\,, \tag{2.109}$$

which resembles Derjaguin's equation, but there $\Delta h(z) = h(z) - h_m \rho_b$, while Equation 2.109 is the same results obtained by Ganti et all.

Connection with the Navier-Stokes equations

It is now interesting to show that Equation 2.107 coincides with the solution of the linearized Navier-Stokes equation for an incompressible fluid when a tangential pressure gradient given by the LE expression is applied [32, 64]. The fully macroscopic Navier-Stokes approach based on the continuum approximation states that the differential equation obeyed by the stationary velocity field $\boldsymbol{v}(\boldsymbol{r})$ of an incompressible fluid can be written as

$$\begin{aligned} 0 &= \partial_t \left(\rho v^\alpha\right) \\ &= -\partial_\beta \Pi^{\alpha\beta} + F^\alpha \,. \end{aligned} \tag{2.110}$$

This is the stationary Navier-Stokes equation, where $\boldsymbol{F}$ is the force field acting on the fluid and it can be due either to the presence of the wall or to an external field. The momentum flux tensor $\Pi^{\alpha\beta}$ can be written in terms of the

[17] Recalling that $\partial_x p_T(z)\big|_{\beta(x),p} = \frac{\partial p_T(z)}{\partial \beta}\Big|_p \partial_x \beta$:

$$\begin{aligned}\frac{\partial \Delta p_T(z)}{\partial T}\Big|_p \partial_x T = \frac{\partial \Delta p_T(z)}{\partial \beta}\Big|_p \partial_x \beta &= \partial_x p_T(z)\big|_{\beta(x),p} = \partial_x p_T(z)\big|_{\beta(x),\mu(x)} \\ &= \partial_x p_T(z)\big|_{\beta(x),[\beta\mu](x)}\end{aligned}$$

and the last identities follow from the freedom in the choice of the thermodynamic variables.

stationary momentum flux $\langle \hat{J}_j^{\alpha\beta}(\boldsymbol{r})\rangle$

$$\Pi^{\alpha\beta} = \langle \hat{J}_j^{\alpha\beta}(\boldsymbol{r})\rangle + \rho v^\alpha v^\beta - \eta\left[\frac{\partial v^\alpha}{\partial r^\beta} - \frac{\partial v^\beta}{\partial r^\alpha}\right] . \tag{2.111}$$

If the limit of small velocities and planar symmetry are considered, the x-component of the velocity field fulfills the linearized Navier-Stokes equation

$$\eta \frac{\mathrm{d}^2 v^x}{\mathrm{d}z^2} = \partial_x p_T \,, \tag{2.112}$$

where we are considering an external potential $V(\boldsymbol{r}) = V(z)$, thus $\boldsymbol{F}$ does not contributes to the velocity field. As usual, we can express the right hand side of the previous equation in terms of the temperature derivative of the tangential pressure at fixed bulk pressure:

$$\eta \frac{\mathrm{d}^2 v^x}{\mathrm{d}z^2} = \partial_x T \frac{\partial p_T(z)}{\partial T}\Big|_p . \tag{2.113}$$

Imposing no-slip boundary conditions at the wall ($v^x(0) = 0$) Equation 2.113 can be easily integrated[18] and the asymptotic velocity field reads

$$v_\infty = -\frac{\partial_x T}{\eta}\frac{\partial}{\partial T}\Big|_p \int_0^\infty \mathrm{d}z' z' \left[p_T(z') - p\right] , \tag{2.114}$$

which coincides with Equation 2.107.

2.3.2 Thermo-osmosis in gases

Let us now examine the other limit, i.e. the rarefied regime. Here kinetic theories provide a quantitative description of the phenomenon, as already explained in the previous Chapter. Our approach should be able to reproduce the known results, in the ideal gas limit, where the creep velocity far from the surface was obtained by Maxwell:

$$v_\infty = \frac{3}{4}\frac{\eta}{\rho}\frac{\nabla T}{T} . \tag{2.115}$$

In this limit, interparticle interactions are negligible, thus the momentum (Equation 2.16) and the energy (Equation 2.27) fluxes can be written as

$$\hat{J}_j^{\alpha\beta}(\boldsymbol{r}) = \sum_i^N \frac{p_i^\alpha p_i^\beta}{m}\delta(\boldsymbol{q}_i - \boldsymbol{r}) \tag{2.116}$$

$$\hat{J}_{\mathcal{H}}^{\alpha}(\boldsymbol{r}) = \sum_i^N \frac{p_i^2 p_i^\alpha}{m}\delta(\boldsymbol{q}_i - \boldsymbol{r}) . \tag{2.117}$$

[18]The first integration is from $h/2$ to z, and we exploit the symmetry of the problem which implies that the derivative of the velocity profile vanishes at $z = h/2$. Then, the second integration proceeds as already described.

Moreover, let us consider a wall which does not exert a force on the fluid. Under these assumptions, for an ideal gases $p_T = p_N = p$ and the static source term $\mathcal{S}_s(z)$ vanishes[19]: p_T does not depend on x and Equation 2.94 simplifies because the second contribution is odd in particles momenta. Thus only the dynamic contribution survives and the source term can be written as

$$\begin{aligned}\mathcal{S}_{IG}(z) = \sum_{i,l} \Bigg\langle \int_0^\infty \mathrm{d}t \int \mathrm{d}\boldsymbol{r}' \delta[\boldsymbol{r} - \boldsymbol{q}_l(t)]\delta(\boldsymbol{r}' - \boldsymbol{q}_i) \\ \cdot \frac{p_l^x(t)p_l^z(t)}{m^2} p_i^x \left[\frac{p_i^2}{2m} - mh_m\right] \Bigg\rangle_0 ,\end{aligned} \tag{2.118}$$

where $\boldsymbol{q}_i$ and $\boldsymbol{p}_i$ are respectively the coordinate and the momentum of the particle at $t = 0$.
Without any kind of interaction between the particles the time integral in Equation 2.118 diverges because the correlations never decay over time. In order to mimic the behavior of an almost ideal gas, where some collisions appear and correlations have a finite life time, we introduce a finite relaxation time τ. This procedure introduces the collisions between the (ideal) particles *a posteriori*, and τ is by definition the time interval between two collisions of a given particle. Moreover only the self correlation contribution (i.e. $i = l$) survives and the source term reads

$$\begin{aligned}\mathcal{S}_{IG}(z) = N \Bigg\langle \int_0^\tau \mathrm{d}t \int \mathrm{d}\boldsymbol{r}' \delta[\boldsymbol{r} - \boldsymbol{q}(t)]\delta(\boldsymbol{r}' - \boldsymbol{q}) \\ \cdot \frac{p^x(t)p^z(t)}{m^2} p^x \left[\frac{p^2}{2m} - mh_m\right] \Bigg\rangle_0 ,\end{aligned} \tag{2.119}$$

where also the indistinguishability between particles has been exploited. In the case of a perfectly reflective wall, it is straightforward to show that the source term is zero. Indeed, specular reflections without energy exchange conserve both the x-component and the modulus of the momentum. It follows that all the integrated quantities in Equation 2.119 can be evaluated at time t. If we perform the canonical transformation $\mathcal{U}(-t)$ the average over the momenta does not depend on time, and the source term vanishes.
In agreement with the results obtained within kinetic theory [44, 53], the occurrence of thermal-creep is possible only assuming that in the particle-surface scattering the momentum or the energy are not conserved. In order to mimic this behavior and to obtain an analytical result, we assume that, due to the scattering process between particles and surface, the x-component of the particle's momenta before and after the collisions are fully uncorrelated. Moreover, we consider a semi-infinite geometry, where only the wall at $h = 0$ is present.

[19] If $V(z) \neq 0$ then $p_T = p_N = p$, but p acquires a dependence over z and x, thus $\mathcal{S}_s(z) \neq 0$.

The averages can be evaluated, without any loss in generality, within the canonical (N, V, T) ensemble and the source term reads

$$\begin{aligned}\mathcal{S}_{IG}(z) = \frac{N}{\tilde{\mathcal{Q}}_c}\int_0^\tau \mathrm{d}t \int \mathrm{d}\boldsymbol{r}' \int \mathrm{d}\boldsymbol{q} \int \mathrm{d}\boldsymbol{p}\, \delta[\boldsymbol{r} - \boldsymbol{q}(t)]\delta(\boldsymbol{r}' - \boldsymbol{q}) \\ \cdot \frac{p^x(t)p^z(t)}{m^2} p^x \left[\frac{p^2}{2m} - mh_m\right] \mathrm{e}^{-\frac{\beta p^2}{2m}}\,,\end{aligned} \tag{2.120}$$

where $\tilde{\mathcal{Q}}_c = V(2\pi m k_\mathrm{B} T)^{\frac{3}{2}}$ is the ideal gas partition function. In order to evaluate the source term it is useful to briefly examine the behavior of a particle, with initial coordinates $\boldsymbol{q}$ and $\boldsymbol{p}$, between the instant $t' = 0$ and a given time $t' = t > 0$. If $p^z \geq -mq^z/t$, the particle does not bounce on the wall in the time interval $[0, t]$[20] and we can write

$$\boldsymbol{p}(t) = \boldsymbol{p}\,, \tag{2.121}$$

$$\boldsymbol{q}(t) = \boldsymbol{q} + \frac{\boldsymbol{p}}{m}t\,. \tag{2.122}$$

On the other hand, when $p^z < -mq^z/t$ the particle hits the wall at time $t_s = -mq^z/p^z < t$. During the scattering the particle has completely lost the memory of the value of p^x before the bounce, therefore the self dynamic correlation $[0, t]$ is equal to 0 and the contribution in Equation 2.120 arising from $p^z < -mq^z/t$ vanishes. Therefore we can restrict the integral over p^z to the domain $[-mq^z/t, +\infty]$ and, exploiting Equations 2.121 and 2.122, we can write

$$\begin{aligned}\mathcal{S}_{IG}(z) = \frac{N}{\tilde{\mathcal{Q}}_c}\int_0^\tau \mathrm{d}t \int \mathrm{d}\boldsymbol{r}' \int \mathrm{d}\boldsymbol{q} \int \mathrm{d}\boldsymbol{p}_\perp \int_{-mq^z/t}^{\infty} \mathrm{d}p^z\, \delta\left(\boldsymbol{r} - \boldsymbol{q} - \frac{\boldsymbol{p}}{m}t\right) \\ \cdot \delta(\boldsymbol{r}' - \boldsymbol{q}) \frac{(p^x)^2 p^z}{m^2} \left[\frac{p^2}{2m} - mh_m\right] \mathrm{e}^{-\frac{\beta p^2}{2m}}\,,\end{aligned} \tag{2.123}$$

where the integral over the momentum $\boldsymbol{p}_\perp$ orthogonal to p^z is extended to $\mathbb{R}^2$. After the evaluation of the integrals in Equation 2.123 the source term results to be

$$\mathcal{S}_{IG}(z) = -\frac{\pi N m \tau}{\hat{\mathcal{Q}}_c \beta^4} \mathrm{e}^{-\beta\frac{mz^2}{2\tau^2}}\,. \tag{2.124}$$

A similar argument allows to write the kernel $\mathcal{K}_{IG}(z, z')$ as

$$\mathcal{K}_{IG}(z, z') = \frac{2\pi N m^2}{\hat{\mathcal{Q}}_c \beta^2} \Theta(z)\Theta(z') \mathrm{e}^{-\beta\frac{m(z-z')^2}{2\tau^2}}\,, \tag{2.125}$$

being $\Theta(\cdot)$ the Heaviside function. Performing an appropriate change of variables the differential equation 2.91 for $u^x(z)$ can be written as

$$\int_0^{+\infty} \mathrm{d}z'\, \partial'_z u^x(z') \frac{2m}{\tau k_\mathrm{B} \partial_x T} \mathrm{e}^{-z'^2 + 2\zeta z'} = 1\,, \tag{2.126}$$

[20] Remembering that the wall is placed at $z = 0$.

where $\zeta = z\sqrt{m\beta/2\tau^2}$, and the solution of this equation reads

$$u^x(z) = \frac{k_\mathrm{B}}{2m}\tau\,\Theta(z+\epsilon)\partial_x T + C\,, \tag{2.127}$$

where C is an additive constant, to be evaluated by imposing the appropriate boundary condition, and $\epsilon \to 0$. The relaxation time τ introduced above can be related to the bulk viscosity η:

$$\begin{aligned}\eta &= \beta\int_0^\tau \mathrm{d}t\int \mathrm{d}\boldsymbol{r}'\langle \hat{J}_j^{xz}(\boldsymbol{r},t)\hat{J}_j^{xz}(\boldsymbol{r}')\rangle_0 \\ &= p\tau\end{aligned} \tag{2.128}$$

where the integrals have been evaluated through the same arguments introduced above for $\mathcal{S}_{IG}(z)$ and $\mathcal{K}_{IG}(z,z')$. Finally, far from the wall, the field $u^x(z)$ can be written as

$$\begin{aligned}u^x(z) &= \frac{\eta}{p}\frac{k_\mathrm{B}T}{2m}\frac{\partial_x T}{T} + C \\ &= \frac{\eta}{2\rho}\frac{\partial_x T}{T} + C\,.\end{aligned} \tag{2.129}$$

As already stated, the velocity field $u^x(z)$ does not have a direct physical meaning. The real flow is related to the average value of the x component of the mass current $\langle\hat{j}^x(z)\rangle$ which we report here

$$\begin{aligned}\langle\hat{j}^x(z)\rangle = \rho u^x(z) &\\ + \int_0^\tau \mathrm{d}t\int \mathrm{d}\boldsymbol{r}'\Big\{\Big\langle\hat{j}^x(\boldsymbol{r},t)\left[\hat{J}^x_{\mathcal{H}}(\boldsymbol{r}') - h_m\hat{j}^x(\boldsymbol{r}')\right]\Big\rangle_0\partial_x\beta & \\ - \beta\Big\langle\hat{j}^x(\boldsymbol{r},t)\hat{J}_j^{xz}(\boldsymbol{r}')\Big\rangle_0\partial'_z u^x(z')\Big\}\,, &\end{aligned} \tag{2.130}$$

where for an ideal gas confined by the wall[21] $\rho(z) = \rho_b$, moreover the flux $\hat{J}^x_Q$ has been written explicitly. In the following we report the space integrals[22] of the dynamic correlation functions appearing in Equation 2.130:

$$\begin{aligned}\int \mathrm{d}\boldsymbol{r}'\langle\hat{j}^x(\boldsymbol{r},t)\hat{J}^x_{\mathcal{H}}(\boldsymbol{r}')\rangle_0 = \frac{5}{2}\frac{\pi N m^2}{\hat{\mathcal{Q}}_c\beta^3}\frac{2\pi}{m\beta}\left[\mathrm{erf}\left(z\sqrt{\frac{\beta m}{2t^2}}\right)+1\right] & \\ - \frac{\pi N m^2}{\hat{\mathcal{Q}}_c\beta^3}\frac{z}{t}\mathrm{e}^{-\beta\frac{mz^2}{2t^2}}\,, &\end{aligned} \tag{2.131}$$

$$h_m\int \mathrm{d}\boldsymbol{r}'\langle\hat{j}^x(\boldsymbol{r},t)\hat{j}^x(\boldsymbol{r}')\rangle_0 = \frac{5}{2}\frac{\pi N m^2}{\hat{\mathcal{Q}}_c\beta^3}\frac{2\pi}{m\beta}\left[\mathrm{erf}\left(z\sqrt{\frac{\beta m}{2t^2}}\right)+1\right] \tag{2.132}$$

[21] Note that also the correlations appearing in Equation 2.130 would vanish with a perfect reflective wall.

[22] Solved with the usual assumptions.

and

$$\int \mathrm{d}\boldsymbol{r}' \langle \hat{j}^x(\boldsymbol{r},t) \hat{J}_j^{xz}(\boldsymbol{r}') \rangle_0 \partial_z' u^x(z') = \frac{\pi N m^2 k_\mathrm{B} \tau \partial_x T}{\hat{\mathcal{Q}}_c \beta^2} \frac{z}{t^2} \mathrm{e}^{-\beta \frac{m z^2}{2t^2}} \,. \tag{2.133}$$

After the time integration we can obtain the final result for the mass current

$$\langle \hat{j}^x(z) \rangle = \frac{\eta}{2} \left\{ 1 + \frac{1}{2} \left\{ \mathrm{erf}\left(\sqrt{\frac{3}{2}} \frac{z}{\ell_g} \right) - \sqrt{\frac{3}{2\pi}} \frac{z}{\ell_g} \mathrm{Ei}\left[-\frac{3}{2} \left(\frac{z}{\ell_g} \right)^2 \right] \right\} \right\} \frac{\partial_x T}{T} \,, \tag{2.134}$$

where the constant C has been evaluated through no-slip boundary conditions and resulted $C = (\eta/4\rho)(\partial_x T/T)$, $\mathrm{Ei}(\cdot)$ is the exponential integral and $\ell_g = \tau\sqrt{3/(m\beta)}$. Far from the wall ($z \gg \ell_g$) the exponential integral rapidly decays to 0 and the slip velocity $v_\infty = \langle \hat{j}^x(z) \rangle|_{z \gg \ell_g} / \rho$ reduces to

$$\begin{aligned} v_\infty &= \frac{3}{4} \frac{\eta}{\rho} \frac{\partial_x T}{T} \\ &= \frac{3}{4} k_\mathrm{B} T \frac{\eta}{p} \frac{\partial_x T}{T} \,, \end{aligned} \tag{2.135}$$

which coincides with the kinetic theory result expressed in Equation 2.115, showing how the slip velocity in rarefied systems is aligned to the temperature gradient and grows at low pressure, as experimentally demonstrated [73], and in agreement with the prediction by Maxwell [53].

2.4 CLOSED CHANNEL

Now let us examine the thermo-osmosis phenomenon in a "closed channel" geometry[23]. We consider an *infinitely long* planar slab of height h with, as usual, a uniform temperature gradient in the x direction. Note that, being the channel infinitely long, the translation symmetry in the x direction (for the system at equilibrium) is not broken[24], thus all the relations and considerations up to Equation 2.85 remain valid.

As in the case of the open channel, we have to fix the value of the gradient $\partial_x[\beta\mu]$, but in this regard an important difference between the two configurations arises. In the open channel a free flow develops and thus the condition of constant bulk pressure has been employed. Instead, the closed configuration imposes the overall constraint of vanishing average mass flux, which can be

[23] "Closed channel" because besides the walls aligned to the temperature gradient there are two walls perpendicular to it at the extremities of the channel.

[24] Perturbations induced by the walls perpendicular to the temperature gradient vanish within some molecular diameter.

expressed as

$$\frac{1}{h}\int_0^h \mathrm{d}z\langle\hat{j}^x(z)\rangle = 0\,. \tag{2.136}$$

This condition has an important consequence: The (physical) velocity profile $v(z) = \langle\hat{j}^x(z)\rangle/\rho(z)$ must change sign over z (maintaining its symmetry with respect to $h/2$). This happens because the thermo-osmotic mass flow pushes particles along the x direction towards a side of the channel and, consequently, a bulk pressure gradient develops in the same direction. It follows that the Poiseuille effect takes place: The bulk pressure gradient drives a mass flow in opposition to the overall thermo-osmotic one in order to exactly balance it. Therefore, the open channel condition to evaluate $\partial_x[\beta\mu]$ can not be applied any more because the bulk pressure is not constant along the x direction, instead we can make use of the condition expressed by Equation 2.136. Thus, let us write this equation as

$$\begin{aligned}&\frac{1}{h}\int_0^h \mathrm{d}z\rho(z)u^x(z) + \frac{1}{h}\int_0^h \mathrm{d}z\mathcal{A}(z)\partial_x\beta - \frac{1}{h}\int_0^h \mathrm{d}z\mathcal{B}(z)\partial_x[\beta\mu]\\ &-\frac{1}{h}\int_0^h \mathrm{d}z\int_0^\infty \mathrm{d}t\int \mathrm{d}\boldsymbol{r}'\beta\langle\hat{j}^x(\boldsymbol{r},t)\hat{J}_j^{xz}(\boldsymbol{r}')\rangle_0\partial'_z u^x(z') = 0\,,\end{aligned} \tag{2.137}$$

where

$$\mathcal{A}(z) = \int_0^\infty \mathrm{d}t\int \mathrm{d}\boldsymbol{r}'\langle\hat{j}^x(\boldsymbol{r},t)\hat{J}^x_{\mathcal{H}}(\boldsymbol{r}')\rangle_0 \tag{2.138}$$

and

$$\mathcal{B}(z) = \int_0^\infty \mathrm{d}t\int \mathrm{d}\boldsymbol{r}'\langle\hat{j}^x(\boldsymbol{r},t)\hat{j}^x_{\rho}(\boldsymbol{r}')\rangle_0\,. \tag{2.139}$$

Reference textbooks, see for example [36], suggest that both $\mathcal{A}(z)$ and $\mathcal{B}(z)$ are divergent quantities. But, in the open channel configuration we have shown that $\partial_x[\beta\mu]_{OC} = \partial_x\beta h_m$ and we have introduced the integrated dynamic correlation function

$$\begin{aligned}\mathcal{A}(z)\partial_x\beta - \mathcal{B}(z)\partial_x[\beta\mu]_{OC} &= \partial_x\beta\int_0^\infty \mathrm{d}t\int \mathrm{d}\boldsymbol{r}'\langle\hat{j}^x(\boldsymbol{r},t)\hat{J}_Q^{x\,OC}(\boldsymbol{r}')\rangle_0\\ &= \partial_x\beta\int_0^\infty \mathrm{d}t\int \mathrm{d}\boldsymbol{r}'\left\langle\hat{j}^x(\boldsymbol{r},t)\left[\hat{J}^x_{\mathcal{H}}(\boldsymbol{r}') - h_m\hat{j}^x_{\rho}(\boldsymbol{r}')\right]\right\rangle_0\\ &= \mathcal{C}_{OC}(z)\end{aligned} \tag{2.140}$$

where $\mathcal{C}_{OC}(z) = 0$ when $z \to \infty$ (to be more precise, when $z \gg \sigma$, where σ is the molecular diameter). Thus in bulk we can write

$$\lim_{z\to\infty}\frac{\mathcal{A}(z)}{\mathcal{B}(z)} = \gamma_{OC}\,, \tag{2.141}$$

where we have defined $\gamma = \partial_x[\beta\mu]/\partial_x\beta$. Relation 2.141 shows that, at least in the bulk of the fluid, the *ratio* of the two divergent quantities $\mathcal{A}(z)$ and $\mathcal{B}(z)$ is finite and does not depends on z far from the surface[25]. Thus we can exploit Equation 2.137 to express the field $\partial_x[\beta\mu]$ in a closed channel:

$$\gamma = \frac{\int_0^h \mathrm{d}z\mathcal{A}(z)}{\int_0^h \mathrm{d}z\mathcal{B}(z)}\,. \tag{2.142}$$

Moreover we can express also the heat flux operator as

$$\hat{J}^x_Q(\boldsymbol{r}) = \hat{J}^x_{\mathcal{H}}(\boldsymbol{r}) - \gamma\hat{j}^x_\rho(\boldsymbol{r})\,. \tag{2.143}$$

Note that in principle $\gamma = \gamma(h)$, because the proportionality between $\mathcal{A}(z)$ and $\mathcal{B}(z)$ is guaranteed only for $z \to \infty$, but for $h \to \infty$ the integrals in Equation 2.142 are dominated by the bulk contribution ($z \to \infty$), thus $\gamma(h) \to \gamma_{OC} = h_m$[26] and $\hat{J}^x_Q(\boldsymbol{r}) \to \hat{J}^{x\,OC}_Q(\boldsymbol{r})$ when $h \to \infty$.
Also in the closed channel configuration, the equation for the velocity field comes from the conservation of the x component of the mass current and it is written in a formally identical way to the open channel case:

$$\int_0^h \mathrm{d}z'\mathcal{K}(z,z')\partial'_z(z') = \partial_x\beta\left[\mathcal{S}_s(z) + \mathcal{S}_d(z)\right]\,, \tag{2.144}$$

where $\mathcal{K}(z,z') = \mathcal{K}_{OC}(z,z')$, but the expressions of the source terms are modified:

$$\begin{aligned}\mathcal{S}_s(z) = &\int_{\frac{h}{2}}^z \mathrm{d}z'\left[\left.\frac{\partial p_T(z')}{\partial\beta}\right|_{[\beta\mu]} - \gamma\left.\frac{\partial p_T(z')}{\partial[\beta\mu]}\right|_{\beta}\right]\\ &- \int \mathrm{d}\boldsymbol{r}'(x-x')\langle\hat{J}^{xz}_j(\boldsymbol{r})\hat{\mathcal{P}}(\boldsymbol{r}')\rangle_0\,,\end{aligned} \tag{2.145}$$

where now

$$\mathcal{P}(\boldsymbol{r}) = \gamma\rho(\boldsymbol{r}) - \mathcal{H}(\boldsymbol{r})\,, \tag{2.146}$$

[25]Note that $\mathcal{A}(z)$ and $\mathcal{B}(z)$ are integrated dynamic correlation functions of an equilibrium system and thus their value in open and closed systems is the same.

[26]The deviation from the open channel value is due to the contributions arising near the surface, on a length scale ξ, thus we can write

$$\gamma(h) = \frac{\int_0^h \mathrm{d}z\mathcal{A}(z)}{\int_0^h \mathrm{d}z\mathcal{B}(z)} = \frac{\int_0^\xi \mathrm{d}z\mathcal{A}(z) + \int_\xi^h \mathrm{d}z\mathcal{A}(z)}{\int_0^\xi \mathrm{d}z\mathcal{B}(z) + \int_\xi^h \mathrm{d}z\mathcal{B}(z)}$$

and when $h \to \infty$

$$\gamma(h) \sim \frac{\int_\xi^h \mathrm{d}z\mathcal{A}(z)}{\int_\xi^h \mathrm{d}z\mathcal{B}(z)} = \gamma_{CO}\,.$$

while

$$\mathcal{S}_d(z) = \int_0^\infty \mathrm{d}t' \int \mathrm{d}\boldsymbol{r}' \langle \hat{J}_j^{xz}(\boldsymbol{r}, t') \hat{J}_Q^x(\boldsymbol{r}') \rangle_0 \,, \tag{2.147}$$

being $\hat{J}_Q^x(\boldsymbol{r})$ defined in Equation 2.143. Finally, we can write the expression for the mass flow in a closed channel

$$\begin{aligned} \langle \hat{j}^x(z) \rangle = \rho(z) u^x(z) \\ + \int_0^\infty \mathrm{d}t' \int \mathrm{d}\boldsymbol{r}' \left[\left\langle \hat{j}^x(\boldsymbol{r}, t') \hat{J}_Q^x(\boldsymbol{r}') \right\rangle_0 \partial_x \beta \right. \\ \left. -\beta \left\langle \hat{j}^x(\boldsymbol{r}, t') \hat{J}_j^{xz}(\boldsymbol{r}') \right\rangle_0 \partial'_z u^x(z') \right] \,, \end{aligned} \tag{2.148}$$

where the dependence of $\langle \hat{j}^x(z) \rangle$ on h due to γ is understood. Also in this case the full knowledge of the mass flow requires to fix the value of the velocity field $u^x(z)$ at some point, for example $z = 0$, but now it is formally provided by Equation the condition of vanishing mass flux

$$\int_0^h \mathrm{d}z \left\langle \hat{j}^x(z) \right\rangle = 0 \,. \tag{2.149}$$

2.4.1 Asymptotic behavior

The closed channel configuration is particular interesting from an experimental point of view. As previously explained, the onset of the thermo-osmotic mass flow induces a bulk pressure gradient $\partial_x p$, which is in principle a measurable quantity of interest in liquid systems[61, 60, 41]. In this regard it is useful to understand how the height h of the system affects this quantity, besides the velocity profile.
At this scope we can use our results for large channels, i. e. $h \gg \sigma$. Moreover let us consider the dense regime limit: Correlation functions are evaluated in bulk and the kernel appearing in Equation 2.144 can be expressed as $\mathcal{K}(z, z') \sim \eta \delta(z - z')$. The point is that the coefficient $\gamma(h)$ depends on the height h of the system and tends to the bulk value[27] $\gamma_{OC} = h_m$ only for $h \to \infty$. Therefore the source term for a large system $\mathcal{S}_A(z)$ differs from its asymptotic value $\mathcal{S}_\infty(z)$ for an additive term due to the difference between $\gamma(h)$ and γ_{CO}:

$$\begin{aligned} \mathcal{S}_A(z) &= \mathcal{S}_\infty(z) + [\gamma(h) - \gamma_{OC}] \int_{\frac{h}{2}}^z \mathrm{d}z' \partial_{\beta\mu} p_T(z') \\ &\sim [\gamma(h) - \gamma_{OC}] \left(z - \frac{h}{2} \right) \partial_{\beta\mu} p \,, \end{aligned} \tag{2.150}$$

[27] The value of γ in an open channel, γ_{OC}, coincides with the value of γ in a bulk system, as shown in Equation 2.141.

where the second equality holds in the bulk region (i. e. $z \gg \sigma$), and where both $\mathcal{S}_A(z)$ and $\mathcal{S}_\infty(z)$ are considered with the dense regime approximations. Now we substitute this expression in the equation for the velocity profile (in the bulk region), leading to

$$\eta \partial_z u^x(z) = \rho \frac{\gamma(h) - \gamma_{OC}}{\beta^2} \left(z - \frac{h}{2} \right) \partial_x \beta \,, \tag{2.151}$$

where the thermodynamic identity $\partial_{\beta\mu} p = \frac{\rho}{\beta^2}$ has been employed. Comparing this Equation with the familiar Navier-Stokes equation for an incompressible fluid (Equation 2.110) we see that the pressure gradient is given by

$$\partial_x p = \rho \frac{\gamma(h) - \gamma_{OC}}{\beta^2} \partial_x \beta \,. \tag{2.152}$$

The solution of Equation 2.151 is the familiar Poiseuille flow:

$$\begin{aligned} u^x(z) &= u_0^x - \left[\rho \frac{\gamma(h) - \gamma_{OC}}{\beta^2} \partial_x \beta \right] \frac{z(h-z)}{2\eta} \\ &= u_0^x - \frac{\partial_x p}{2\eta} z(h-z) \end{aligned} \tag{2.153}$$

(valid for $z \gg \sigma$) where both γ and $u_0^x = u^x(z=0)$ depend on the channel height h. Let us now employ the mass conservation condition to evaluate u_0:

$$\rho h \left[u^x(0) - \frac{\partial_x p}{12\eta} h^2 \right] = \omega \,, \tag{2.154}$$

where ω is the contribution coming from the three dynamical correlation functions appearing in Equation 2.137, and, according to the previous assumptions, it is independent of h. Note that, to be more consistent with the dense regime approximation assumed in the definition of $\mathcal{K}(z, z')$ and $\mathcal{S}_A(z)$, we should set $\omega = 0$. Nevertheless we can maintain this dynamic contribution in order to include somehow the effect of the dynamic correlation functions near the surface[28]. Finally, we can express the full velocity profile[29]

$$v(z) = \frac{\omega}{\rho h} + \frac{\partial_x p}{12\eta} h^2 - \frac{\partial_x p}{2\eta} z(h-z) \,, \tag{2.155}$$

while the velocity at mid-height results to be

$$v(z)|_{z=\frac{h}{2}} = \frac{\omega}{\rho h} - \frac{\partial_x p}{24\eta} h^2 \,. \tag{2.156}$$

[28] As later explained, their contribution here included becomes negligible in the asymptotic limit $h \to \infty$.

[29] Note that in bulk $v(z) = u^x(z)$.

In the asymptotic limit, that is when $h \to \infty$, the mid-height velocity and the bulk pressure gradient are connected by a particularly simple relation

$$v|_{z=\frac{h}{2}}^{\infty} = -\frac{\partial_x p}{24\eta} h^2 \,. \tag{2.157}$$

Unfortunately both $v|_{z=\frac{h}{2}}^{\infty}$ and $\partial_x p$, expressed in Equation 2.152, in principle depend on h[30], thus Equation 2.157 cannot directly define the behavior of $\partial_x p$ with h. At this point we can only state that $\partial_x p$ must go to zero as h^{-2} or faster, in order to avoid an unphysical divergent behavior of $v|_{z=\frac{h}{2}}^{\infty}$.
Note that the numerical factor $\frac{1}{24}$ appearing in Equation 2.157 derives from the adoption of the three-dimensional slit geometry in the Navier-Sokes Equation reported in 2.110. For what will follow in Chapter 4 it is important to note that the same numerical factor is obtained in a two-dimensional slit geometry[31]. Thus Equation 2.157 holds also in 2D systems.

[30] On the contrary, η is a bulk property of the fluid, thus it does not depend on h.
[31] While, for example it changes in a circular pipe geometry, where it results to be $\frac{1}{48}$.

3

The role of correlation functions

In the previous Chapter we developed a microscopic theory of the thermo-osmosis phenomenon. From a physical point of view one of the most important results of this approach is the rigorous formalization of the thermal forces. In particular the presence of two different underlying mechanisms arises, a static one and a dynamic one, whose effects are expressed in terms of correlation functions, which consequently play a fundamental role in the theory of thermo-osmosis. Thus, it is indeed useful leaving for a while the main object of this thesis in order to examine more in depth some aspects related to the correlation functions.

As previously discussed, the static source term is written as the sum of two contributions: The temperature derivative of the pressure tensor and a specific static correlation function. Both terms are separately ill defined, because depend on the arbitrary choice of the integration path. However this ambiguity is expected to cancel in the particular combination defining the full static source term. This important analytical result will be tested from a numerical point of view evaluating the pressure tensors according to the two different definitions by Irving and Kirkwood [42] and Harasima [38]. We will show our numerical results for a two-dimensional geometry, which allows to simulate larger systems thereby reducing statistical errors.

Regarding the dynamic correlation functions, our attention will not be focused on the dynamic source term, but rather we will consider the more general problem of the definition of transport coefficients in two-dimensional systems[1]

[1] For static correlation functions problems related to the dimensionality of the system do not arise.

through the linear response theory formalism[2]. In particular we will numerically study the viscosity of a 2D fluid. This aspect will be particularly interesting in the interpretation of the results presented in the next Chapter, where direct simulations of thermo-osmotic mass flows in 2D systems will be discussed.
All the numerical results presented in this Chapter and in the next one are obtained by the molecular dynamics simulation technique. This choice is particular suitable to our purposes, because it allows to simulate both equilibrium and nonequilibrium systems. Simulations were performed through the open source software LAMMPS [65] (http://lammps.sandia.gov), supplemented by few customized routines.

3.1 NUMERICAL ALGORITHM TO COMPUTE CORRELATION FUNCTIONS

The routines employed to compute correlation functions and their integrals in two-dimensional systems were added to the open source software LAMMPS. Here we describe their basic structure.
Let us consider two generic operators $\mathcal{O}^1$ and $\mathcal{O}^2$ and their associated equilibrium correlation function

$$C(\boldsymbol{r}, \boldsymbol{r}', t) = \left\langle \mathcal{O}^1(\boldsymbol{r}, t)\mathcal{O}^2(\boldsymbol{r}') \right\rangle_0 . \tag{3.1}$$

In order to compute $C(\boldsymbol{r}, \boldsymbol{r}', t)$ we need to define a mesh over the system. The elements of this mesh are squares of side $\Delta = 0.05\sigma$ and for each simulation step the value of the *discretized* operators is computed on each of these squares. The link between the formal definition of these operators and their discretized counterpart computed on the mesh is provided by the following relation:

$$\tilde{\mathcal{O}}_{in} = \frac{1}{\Delta^2} \int_{x_i - \frac{\Delta}{2}}^{x_i + \frac{\Delta}{2}} \mathrm{d}x' \int_{z_i - \frac{\Delta}{2}}^{z_i + \frac{\Delta}{2}} \mathrm{d}z' \mathcal{O}(\boldsymbol{r}', t_n) , \tag{3.2}$$

where the subscript i refers to the mesh element centered in the position $\boldsymbol{r}$, while n refers to the simulation time step. As a result, also the corresponding correlation functions are discretized and can be expressed as

$$\tilde{C}_{ijn} = \left\langle \tilde{\mathcal{O}}^1_{in} \tilde{\mathcal{O}}^2_j \right\rangle_0 . \tag{3.3}$$

Due to the time translation invariance of the equilibrium correlation function, the label n here refers to the difference between the computational time steps of $\tilde{\mathcal{O}}^1_{in}$ and $\tilde{\mathcal{O}}^2_j$.

[2]We remember that linear response theory allows to compute a given transport coefficient as the integrals over space and time of a particular dynamic correlation function, i. e. through the so-called Green-Kubo relations.

For our purposes the most interesting quantities are the space integrals of the correlation functions, and we can easily express them as

$$\begin{aligned}\int \mathrm{d}\boldsymbol{r}' C(\boldsymbol{r},\boldsymbol{r}',t) &\rightarrow \sum_j \tilde{C}_{ijn}\Delta^2 \\ &= \Delta^2 \sum_j \left\langle \tilde{\mathcal{O}}^1_{in}\tilde{\mathcal{O}}^2_j \right\rangle_0 \\ &= \Delta^2 \left\langle \tilde{\mathcal{O}}^1_{in} \sum_j \tilde{\mathcal{O}}^2_j \right\rangle_0 \\ &= \Delta^2 \left\langle \tilde{\mathcal{O}}^1_{in}\tilde{\mathcal{I}}^2 \right\rangle_0 ,\end{aligned} \tag{3.4}$$

where the arrow links the analytical and numerical definitions of the integrals. When the system is characterized by some translation symmetry it can be exploited to improve the statistics accuracy in the calculation of the integrated correlation function. This is accomplished through an average operation in the translation-invariant direction:

$$\begin{aligned}\int \mathrm{d}\boldsymbol{r}' C\left(\boldsymbol{r}-\boldsymbol{r}',t\right) &= \frac{1}{A}\int \mathrm{d}\boldsymbol{r} \int \mathrm{d}\boldsymbol{r}' C\left(\boldsymbol{r}-\boldsymbol{r}',t\right) \\ &\rightarrow \frac{\Delta^2}{A}\sum_i \left\langle \tilde{\mathcal{O}}^1_{in}\,\mathcal{I}^2 \right\rangle_0 \Delta^2 \\ &= \frac{\Delta^4}{A}\left\langle \sum_i \tilde{\mathcal{O}}^1_{in}\,\mathcal{I}^2 \right\rangle_0 \\ &= \frac{\Delta^4}{A}\left\langle \mathcal{I}^1_n \mathcal{I}^2 \right\rangle_0\end{aligned} \tag{3.5}$$

where A is the area of the system and a homogeneous system has been considered. Note that if $\mathcal{O}^1$ and $\mathcal{O}^2$ refer to conserved quantities the associated correlation function computed through a molecular dynamics simulation will be zero or constant over time. For example, in order to numerically compute dynamic correlation functions a NVE dynamics is required and so if the operators $\mathcal{O}^1$ or $\mathcal{O}^2$ refers to the particles momenta the corresponding correlation function computed through Equation 3.5 would be equal to zero. In appendix A we will show a way that possibly overcomes this problem.
In a bulk system Equation 3.5 can be employed to compute a given transport coefficient $\mathcal{T}$, but in its Green-Kubo definition also a time integration is involved

$$\mathcal{T} \rightarrow \frac{\Delta^4}{A}\sum_{n=0}^{N}\left\langle \mathcal{I}^1_n \mathcal{I}^2 \right\rangle_0 \delta t\,, \tag{3.6}$$

where δt is the time separation between two consecutive time steps. Here the arrow $\rightarrow$ points out that the right hand side of the Equation 3.6 does

not necessary define the transport coefficient $\mathcal{T}$: Indeed the time integration domain in its definition is $(0, \infty)$, and this cannot be reproduced on a computer (where $N \not\to \infty$). More importantly, in 2D systems the possibility to define transport coefficient is still a debated issue. This happens because general arguments suggest that at long times $C(\boldsymbol{r}, \boldsymbol{r}', t)$ is characterized by the power-law decay $t^{-\frac{d}{2}}$ [66, 36], where d is the dimensionality of the system. It follows that in 2D systems the time integral should diverge.
In the last Section of this Chapter we will address this problem by computing the viscosity, defined as

$$\eta(\boldsymbol{r}) = \beta \int_0^\infty \mathrm{d}t \int \mathrm{d}\boldsymbol{r}' \left\langle \hat{J}_j^{xz}(\boldsymbol{r}, t) \hat{J}_j^{xz}(\boldsymbol{r}') \right\rangle_0 , \tag{3.7}$$

in a 2D closed system[3]. In a confined system the associated viscosity (if existing) is space-dependent, $\eta = \eta(\boldsymbol{r})$, thus we should not use Equation 3.6. Nevertheless it is still possible to exploit this Equation also in a confined system in order to obtain the average viscosity

$$\frac{1}{A} \int \mathrm{d}\boldsymbol{r} \eta(\boldsymbol{r}) \to \frac{\Delta^4}{A} \beta \sum_{n=0}^{N} \langle \Pi_n^{xz} \Pi^{xz} \rangle_0 \, \delta t \, , \tag{3.8}$$

where the integral operator Π^{xz} is defined as

$$\Pi^{xz} = \sum_l \tilde{J}_{j,l}^{xz} \, . \tag{3.9}$$

The operators Π^{xz} are computed during the simulation, while the time integration and the autocorrelation operation are performed by post processing of the data.
Let us now consider the contribution given by the static correlation function to the static source term. Its numerical form can be expressed as

$$\begin{aligned} \int \mathrm{d}\boldsymbol{r}'(x' - x) \left\langle \mathcal{O}^1(\boldsymbol{r}) \mathcal{O}^2(\boldsymbol{r}') \right\rangle_0 &\to \Delta^2 \sum_{\xi'} (\xi' - \xi) \sum_{\zeta'} \left\langle \tilde{\mathcal{O}}^1_{\xi\zeta} \tilde{\mathcal{O}}^2_{\xi'\zeta'} \right\rangle_0 \\ &= \Delta^2 \left\langle \tilde{\mathcal{O}}^1_{\xi\zeta} \sum_{\xi'} (\xi' - \xi) \sum_{\zeta'} \tilde{\mathcal{O}}^2_{\xi'\zeta'} \right\rangle_0 \end{aligned} \tag{3.10}$$

where ξ and ζ are respectively the x and z indices of the mesh element centered in $\boldsymbol{r}$, while ξ' and ζ' of the one centered in $\boldsymbol{r}'$. If we now consider a system such as the one shown in Figure 2.1, the integral of Equation 3.10 depends just on the z coordinate. Moreover, we can express it in an equivalent form as

$$\int \mathrm{d}\boldsymbol{r}'(x' - x) \left\langle \mathcal{O}^1(\boldsymbol{r}) \mathcal{O}^2(\boldsymbol{r}') \right\rangle_0 = \int \mathrm{d}\boldsymbol{r}' x' \left\langle \mathcal{O}^1(\boldsymbol{r}) \mathcal{O}^2(\boldsymbol{r}') \right\rangle_0 \tag{3.11}$$

[3]Note that the viscosity coefficient could acquire a dependence also on the simulation box size, but we will deeply discuss this point in the last Section of this Chapter.

and as a consequence its numerical counterpart can be expressed as

$$\int \mathrm{d}\boldsymbol{r}' x' \left\langle \mathcal{O}^1(\boldsymbol{r})\mathcal{O}^2(\boldsymbol{r}')\right\rangle_0 \to \Delta^2 \left\langle \tilde{\mathcal{O}}^1_{0\zeta} \sum_{\xi'} \xi' \sum_{\zeta'} \tilde{\mathcal{O}}^2_{\xi'\zeta'} \right\rangle_0 , \tag{3.12}$$

where now the index ξ is kept fix at $\xi = 0$[4]. The algorithm based on Equation 3.10 can exploit the invariance of the system with respect to translation in the x direction, but the one based on 3.12 resulted to be significantly faster.
Note that all the equilibrium averages $\langle ... \rangle_0$ are performed both through different initial conditions (ensemble average) and exploiting the ergodicity of fluid systems (time average). However the average procedure will be better explained later.

3.2 NON UNIQUENESS OF THE MICROSCOPIC PRESSURE TENSOR

Let us now recall the expression of the static source term in an open channel:

$$\mathcal{S}_s(z) = \int_{\frac{h}{2}}^{z} \mathrm{d}z' \left. \frac{\partial \left\langle \hat{J}^{xx}_j(z') \right\rangle_0}{\partial \beta} \right|_p - \int \mathrm{d}\boldsymbol{r}'(x - x')\langle \hat{J}^{xz}_j(\boldsymbol{r})\hat{\mathcal{P}}(\boldsymbol{r}')\rangle_0 \,, \tag{3.13}$$

where the operator $\hat{\mathcal{P}}$ is defined as

$$\hat{\mathcal{P}}(\boldsymbol{r}) = h_m \hat{\rho}(\boldsymbol{r}) - \hat{\mathcal{H}}(\boldsymbol{r}) \,. \tag{3.14}$$

The operators $\hat{\rho}(\boldsymbol{r})$ and $\hat{\mathcal{H}}(\boldsymbol{r})$ are *punctual* operators, that is they are defined exactly on the particles positions (see their expressions in Equations 2.6 and 2.8). Instead, the momentum flux operator is characterized by a *non-local* term which arises from the $\hat{J}^{\alpha\beta}_j(\boldsymbol{r})$ configurational contribution[5]

$$\hat{J}^{\alpha\beta}_{j,CO}(\boldsymbol{r}) = -\frac{1}{2} \sum_{i \neq l}^{N} \frac{q^\alpha}{|\boldsymbol{q}_{li}|} \left. \frac{\mathrm{d}\varphi(q)}{\mathrm{d}q} \right|_{q=|\boldsymbol{q}_{li}|} \oint_{\ell_{l\to i}} \mathrm{d}\ell^\beta \delta(\boldsymbol{\ell} - \boldsymbol{r}) \,. \tag{3.15}$$

Indeed it is defined also in the regions of space (and thus in the corresponding mesh elements) intersected by the contour $\ell_{l\to i}$ and not just at the particles position $\boldsymbol{q}_i$ and $\boldsymbol{q}_l$: The integral contour can be interpreted as the path across which particles i and l exchange the force $\mathrm{d}\varphi_{li}/\mathrm{d}q$. Moreover, as pointed out

[4]Note that $x \in [-L_x/2, +L_x/2]$., where L_x is the length of the simulation box in the x direction.

[5]Here a system of particles interacting through a central pair-wise potential is considered.

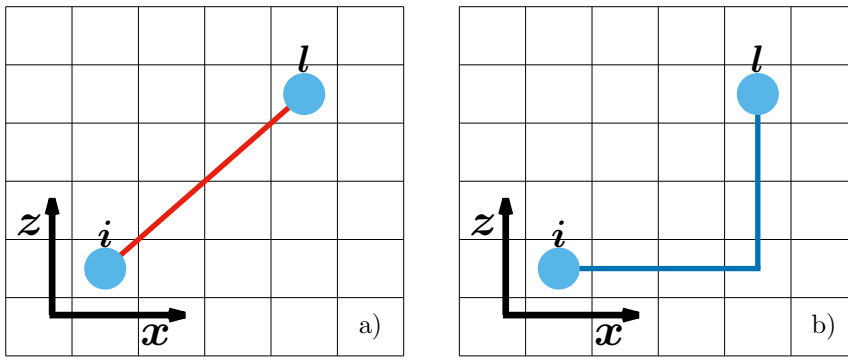

Figure 3.1: Representation of the Iriving-Kirkwood (panel a, red line) and Harasima (panel b, blue line) contours. Labelled light blue spheres symbolize two fluid particles.

in the previous Chapter, different contours $\ell_{l\to i}$ lead to different non-local configurational contributions and because of this freedom in the choice of the integration contour it is not possible to define a unique pressure tensor.
In what follows we will introduce two different kinds of contours, which lead to the definitions of the well-known Irving-Kirkwood (IK) and Harasima (Ha) pressure tensors, and we will use them to numerically verify the independence of $\mathcal{S}_s(z)$ from the choice of the integration contour.

3.2.1 Irving-Kirkwood and Harasima contours

Let us now consider two different choices of lines across which particles exchange forces. The first one is simply the straight segment joining particle i and particle l (shown in Figure 3.1, panel a), that is

$$\begin{aligned}\boldsymbol{\ell} &= \boldsymbol{q}_i\lambda + \boldsymbol{q}_l(1-\lambda)\\ &= \boldsymbol{q}_{li}\lambda + \boldsymbol{q}_l\,,\end{aligned} \tag{3.16}$$

where λ is the unique parameter of the chosen line and $\lambda \in [0,1]$. We can change the integration variable from ℓ^β to λ (referring to Equation 3.15), thus we can write

$$\begin{aligned}\hat{J}^{\alpha\beta}_{j,IK}(\boldsymbol{r}) = &\sum_i \frac{p_i^\alpha p_i^\beta}{m}\delta(\boldsymbol{q}_i - \boldsymbol{r})\\ &-\frac{1}{2}\sum_{i\neq l}\frac{q_{il}^\alpha q_{il}^\beta}{|\boldsymbol{q}_{il}|}\frac{\mathrm{d}\varphi_{li}}{\mathrm{d}q}\int_0^1 \mathrm{d}\lambda \prod_{\gamma=x,z}\delta(q_{il}^\gamma\lambda + q_i^\gamma - r^\gamma)\,,\end{aligned} \tag{3.17}$$

where the subscript IK points out that this choice of $\boldsymbol{\ell}$ is the one which defines the Irving-Kirkwood [42] local pressure tensor:

$$\begin{aligned}\left\langle \hat{J}^{\alpha\beta}_{j,IK}(\boldsymbol{r})\right\rangle_0 &= \left\langle \sum_i \frac{p_i^\alpha p_i^\beta}{m}\delta(\boldsymbol{q}_i-\boldsymbol{r})\right\rangle_0 \\ &\quad - \frac{N}{2}\left\langle \sum_{i\neq l}\frac{q_{il}^\alpha q_{il}^\beta}{|\boldsymbol{q}_{il}|}\frac{\mathrm{d}\varphi_{li}}{\mathrm{d}q}\int_0^1 \mathrm{d}\lambda \prod_{\gamma=x,z}\delta(q_{il}^\gamma\lambda + q_i^\gamma - r^\gamma)\right\rangle_0 .\end{aligned} \tag{3.18}$$

Let us now consider a system characterized by a planar geometry as shown in Figure 2.1, where the translational invariance is maintained in the x direction. The local pressure tensor then acquires a dependence only on the z variable, and we can exploit the average in the x direction to increase statistics:

$$\begin{aligned}\left\langle \hat{J}^{\alpha\beta}_{j,IK}(z)\right\rangle_0 &= \frac{1}{L_x}\int \mathrm{d}x \left\langle \hat{J}^{\alpha\beta}_{j,IK}(\boldsymbol{r})\right\rangle_0 \\ &= \frac{\rho(z)}{L_x\beta}\delta^{\alpha\beta} \\ &\quad - \frac{N}{2L_x}\left\langle \sum_{i\neq l}\frac{q_{il}^\alpha q_{il}^\beta}{|\boldsymbol{q}_{il}|}\frac{\mathrm{d}\varphi_{li}}{\mathrm{d}q}\int_0^1 \mathrm{d}\lambda\,\delta(z_{il}\lambda + z_i - z)\right\rangle_0 \\ &= \frac{\rho(z)}{L_x\beta}\delta^{\alpha\beta} \\ &\quad - \frac{N}{2L_x}\left\langle \sum_{i\neq l}\frac{q_{il}^\alpha q_{il}^\beta}{|\boldsymbol{q}_{il}||z_{il}|}\frac{\mathrm{d}\varphi_{li}}{\mathrm{d}q}\Theta\left(\frac{z_l-z}{z_{il}}\right)\Theta\left(\frac{z-z_i}{z_{il}}\right)\right\rangle_0 ,\end{aligned} \tag{3.19}$$

where L_x is the size of the system in the x direction and Θ is the Heaviside step function. Thus, the normal ($\alpha=\beta=z$) and tangential ($\alpha=\beta=x$) components of the local pressure tensor read

$$p_T^{IK}(z) = \frac{\rho(z)}{L_x\beta} - \frac{N}{2L_x}\left\langle \sum_{i\neq l}\frac{x_{il}^2}{|\boldsymbol{q}_{il}||z_{il}|}\frac{\mathrm{d}\varphi_{li}}{\mathrm{d}q}\Theta\left(\frac{z_l-z}{z_{il}}\right)\Theta\left(\frac{z-z_i}{z_{il}}\right)\right\rangle_0 \tag{3.20}$$

and

$$p_N^{IK}(z) = \frac{\rho(z)}{L_x\beta} - \frac{N}{2L_x}\left\langle \sum_{i\neq l}\frac{z_{il}^2}{|\boldsymbol{q}_{il}||z_{il}|}\frac{\mathrm{d}\varphi_{li}}{\mathrm{d}q}\Theta\left(\frac{z_l-z}{z_{il}}\right)\Theta\left(\frac{z-z_i}{z_{il}}\right)\right\rangle_0 \tag{3.21}$$

while the out-of-diagonal component results to be

$$p_{xz}^{IK}(z) = -\frac{N}{2L_x}\left\langle \sum_{i\neq l}\frac{x_{il}z_{il}}{|\boldsymbol{q}_{il}||z_{il}|}\frac{\mathrm{d}\varphi_{li}}{\mathrm{d}q}\Theta\left(\frac{z_l-z}{z_{il}}\right)\Theta\left(\frac{z-z_i}{z_{il}}\right)\right\rangle_0 . \tag{3.22}$$

Another possible choice of the contour line $\boldsymbol{\ell}$ is represented by two segments

(shown in Figure 3.1, panel b): One which connects the points (x_i, z_i) and (x_l, z_i), while the other connects the points (x_l, z_i) and (x_l, z_l). Such a line can be expressed as:

$$\boldsymbol{\ell} = (x_{il}\lambda_x + x_i, z_{il}\lambda_z + z_i) \tag{3.23}$$

where two parameters λ_x and λ_z have been introduced and $\lambda_z = 0$ for $\lambda_x \in [0, 1)$, while $\lambda_z \in (0, 1]$ for $\lambda_x = 1$. Adopting this contour the momentum flux operator results to be

$$\begin{aligned}\hat{J}^{\alpha z}_{j,Ha}(\boldsymbol{r}) = &\sum_i \frac{p_i^\alpha p_i^\beta}{m}\delta(\boldsymbol{q}_i - \boldsymbol{r}) \\ &- \frac{1}{2}\sum_{i\neq l}\frac{q_{il}^\alpha q_{il}^z}{|\boldsymbol{q}_{il}|}\frac{\mathrm{d}\varphi_{li}}{\mathrm{d}q}\delta(x - x_l)\int_0^1 \mathrm{d}\lambda\,\delta(z_{il}\lambda_z + z_i - z)\end{aligned} \tag{3.24}$$

and

$$\begin{aligned}\hat{J}^{xx}_{j,Ha}(\boldsymbol{r}) = &\sum_i \frac{(p_i^x)^2}{m}\delta(\boldsymbol{q}_i - \boldsymbol{r}) \\ &- \frac{1}{2}\sum_{i\neq l}\frac{x_{il}^2}{|\boldsymbol{q}_{il}|}\frac{\mathrm{d}\varphi_{li}}{\mathrm{d}q}\delta(z - z_i)\int_0^1 \mathrm{d}\lambda\,\delta(x_i + x_{li}\lambda_x - x)\,,\end{aligned} \tag{3.25}$$

where the subscript Ha indicates that $\left\langle \hat{J}^{\alpha\beta}_{j,Ha}(\boldsymbol{r})\right\rangle_0$ is the pressure tensor defined by Harasima [38] (and by Kirkwood and Buff [45]). Now we can specialize also this pressure tensor to the usual geometry of Figure 2.1 and thus obtain

$$p_T^{Ha}(z) = \frac{\rho(z)}{L_x\beta} - \frac{N}{2L_x}\left\langle \sum_{i\neq l}\frac{x_{il}^2}{|\boldsymbol{q}_{il}|}\frac{\mathrm{d}\varphi_{li}}{\mathrm{d}q}\delta\left(z - z_i\right)\right\rangle_0\,, \tag{3.26}$$

$$p_N^{Ha}(z) = \frac{\rho(z)}{L_x\beta} - \frac{N}{2L_x}\left\langle \sum_{i\neq l}\frac{z_{il}^2}{|\boldsymbol{q}_{il}||z_{il}|}\frac{\mathrm{d}\varphi_{il}}{\mathrm{d}q}\Theta\left(\frac{z_l - z}{z_{il}}\right)\Theta\left(\frac{z - z_i}{z_{il}}\right)\right\rangle_0 \tag{3.27}$$

and

$$p_{xz}^{Ha}(z) = -\frac{N}{2L_x}\left\langle \sum_{i\neq l}\frac{x_{il}z_{il}}{|\boldsymbol{q}_{il}||z_{il}|}\frac{\mathrm{d}\varphi_{li}}{\mathrm{d}q}\Theta\left(\frac{z_l - z}{z_{il}}\right)\Theta\left(\frac{z - z_i}{z_{il}}\right)\right\rangle_0\,. \tag{3.28}$$

At this point it is useful to compare the components of the two tensors expressed for the slit geometry. The tangential pressures, which enter in the first term of the static source term, result to be different[6], while the normal

[6]It is interesting to note that p_T^{Ha} is equal to the expression of the tangential virial pressure in the slit geometry.

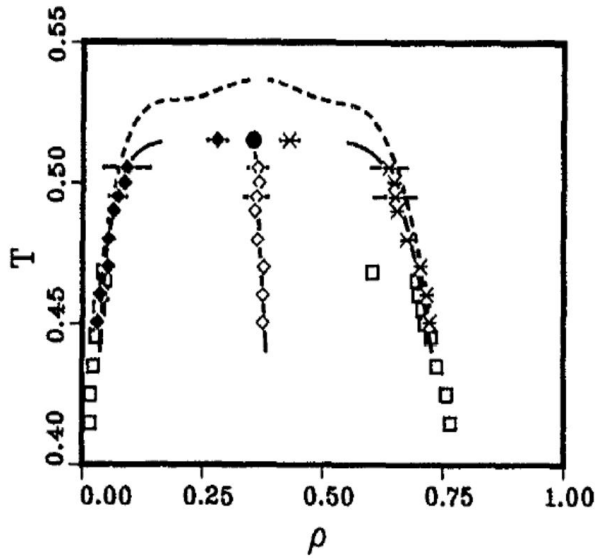

Figure 3.2: Phase diagram of the two-dimensional Lennard-Jones fluid. This Figure is taken from Ref. [72], where the meaning of the different symbols and lines are explained.

components are identical, as the hydrostatic equilibrium condition imposes. Also the expressions for p_{xz} are the same, and it means that p_{xz}^{IK} and p_{xz}^{Ha} fluctuate around zero exactly at the same way, while the fluctuations are different if the local expressions of these operators (Equation 3.17 and 3.24) are considered. This observation implies that the microscopic expression of $\hat{J}_{j,IK}^{xz}$ and $\hat{J}_{j,Ha}^{xz}$ must be employed in order to compute correlation functions, like the one appearing in the second term of the static source term, while the first one can be obtained through p_T^{Ha} and p_T^{IK}. It is now interesting to evaluate through molecular dynamics simulations the differences related to the tangential components of these two tensors, with particular attention to the derivative $\partial_\beta p_T(z)|_p$ and its integral $\int_{\frac{h}{2}}^{z} \mathrm{d}z' \partial_\beta p_T(z')|_p$.

Simulation details

The interparticle interactions are modeled through a truncated and shifted Lennard-Jones potential

$$\varphi(r) = \begin{cases} \varphi_{LJ}(r) - \varphi_{LJ}(r_c) & r \leq r_c \\ 0 & r > r_c \end{cases} \tag{3.29}$$

where the cut-off distance r_c is $r_c = 4.5\sigma$ [7] and the expression of the 12-6 LJ

Physical quantity	Unit	Value fo Ar
Length	σ	3.4×10^{-10} m
Energy	ϵ	1.65×10^{-21} J
Mass	m	6.69×10^{-26} kg
Time	$\tau = \sigma\sqrt{m/\epsilon}$	2.17×10^{-12} s

Table 3.1: Other quantities presented in the following can be directly derived by σ, ϵ, m and τ. For future references also the value of these parameters for Argon are reported.

potential reads

$$\varphi_{LJ}(r) = 4\epsilon_{ff}\left[\left(\frac{\sigma_{ff}}{r}\right)^{12} - \left(\frac{\sigma_{ff}}{r}\right)^{6}\right] \tag{3.30}$$

where the parameters $\epsilon_{ff} = 1\epsilon$ and $\sigma_{ff} = 1\sigma$ represent the depth of the potential well and the particle diameter respectively[8]. The phase diagram of the two-dimensional Lennard-Jones fluid is shown in Figure 3.2. This Figure is not a result obtained by us, instead it is taken from Ref. [72]. Here and in the following simulation results are expressed adopting the unit of measure expressed in Tab. 3.1.

Rectangular simulation boxes with $L_x = 200\sigma$ and periodic boundary conditions in the x direction are employed. In the z direction particles are confined by a wall at the bottom ($z = 0$) and by a piston at the top (see Figure 3.3). This piston is pushed down by a force F gauged in order to obtain the desired bulk pressure[9], thus it works like a barostat. Three kind of lower confining walls are considered, a reflective wall and two Einstein solids. Particles of the Einstein solids behave as independent harmonic oscillators (they are fixed to their position by a harmonic potential with elastic constant $k = 5000\epsilon/\sigma^2$) but they interact with fluid particles with a LJ 12-6 truncated and shifted potential. Two different ϵ_{wf} parameters were considered for the two walls, $\epsilon_{wf} = 0.1\epsilon$ and $\epsilon_{wf} = 0.5\epsilon$, while in both cases $\sigma_{wf} = 1\sigma$.

The temperature control is achieved through the so-called Bussi-Donadio-Parrinello thermostat (see Appendix B for more details) [11], and, in order to compute $\partial_\beta p_T(z)|_p$, for each considered confinement and value of bulk pressure p we performed two independent simulations at $T_H = 0.95\epsilon/k_B$ and $T_C = 0.85\epsilon/k_B$. Systems at different bulk pressures were simulated, ranging from $p \approx 0.036\epsilon/\sigma^2$ (with $\rho_H \approx 0.039\sigma^{-2}$, $N_C = 837$, $\rho_C \approx 0.045\sigma^{-2}$ and

[7] As shown in Ref. [29] the fluid static properties near the wall are essentially unaffected by the choice of the cut-off distance if it is greater than 4σ.

[8] The subscript ff refers to the fluid-fluid interaction while in the following the subscript wf will be introduced; it refers to the wall-fluid interaction.

[9] Therefore the height of the fluid is not properly fixed, because the piston slightly oscillates.

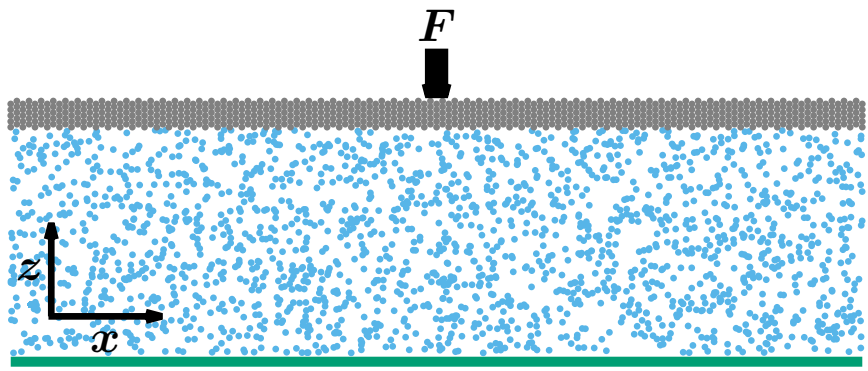

Figure 3.3: Schematic of the simulated system. Fluid particles are represented by the light blue spheres, while the piston, which is modeled as an Einstein solid and pushed by the force F, by the grey ones. The confinement placed at $z = 0$ is represented by the green line.

$N_C = 1000$) up to $p \approx 1.31\epsilon/\sigma^2$ (with $\rho_H \approx 0.675$, $N_H = 4725$, $\rho_C \approx 0.707\sigma^{-2}$ and $N_C = 4949$).

The time step has been chosen as $\delta t = 0.005\tau$. Simulations are divided into three stages: In the first stage the systems are equilibrated keeping the piston fixed for 10^7 time steps. In the second, the piston is released and the external force F is applied. 10^7 time steps are required to dump oscillations. In the last stage measurements are performed for 10^9 time steps.

As previously stated, the mesh size is set to $\Delta = 0.05\sigma$ and pressure profiles are measured in the whole system.

Results

These equilibrium simulations allow to compute the Irving-Kirkwood and Harasima pressure tensors previously introduced. The tangential components reported in Equations 3.20 and 3.26 clearly manifest their dissimilarity also in the numerical results, as shown in Figure 3.4, panel a. Here the fluid is kept at $p \approx 1.31\epsilon/\sigma^2$ and $T = 0.85\epsilon/k_\mathrm{B}$ and the bulk density is $\rho \approx 0.707\sigma^{-2}$, while the lower confinement is provided by a reflective wall. Both the tangential components strongly oscillate near the wall, while the normal component is everywhere constant, as it should be due to the hydrostatic equilibrium condition. All curves converge to the bulk pressure value within about 10σ from the confining surface. This kind of simulation allows also to verify the effect of different confinements on the tangential component of the pressure tensor and it is shown in the panel b of Figure 3.4, where three different systems confined by the walls previously introduced and in the same thermodynamic conditions of the previous case are considered. Here only the Harasima tensor

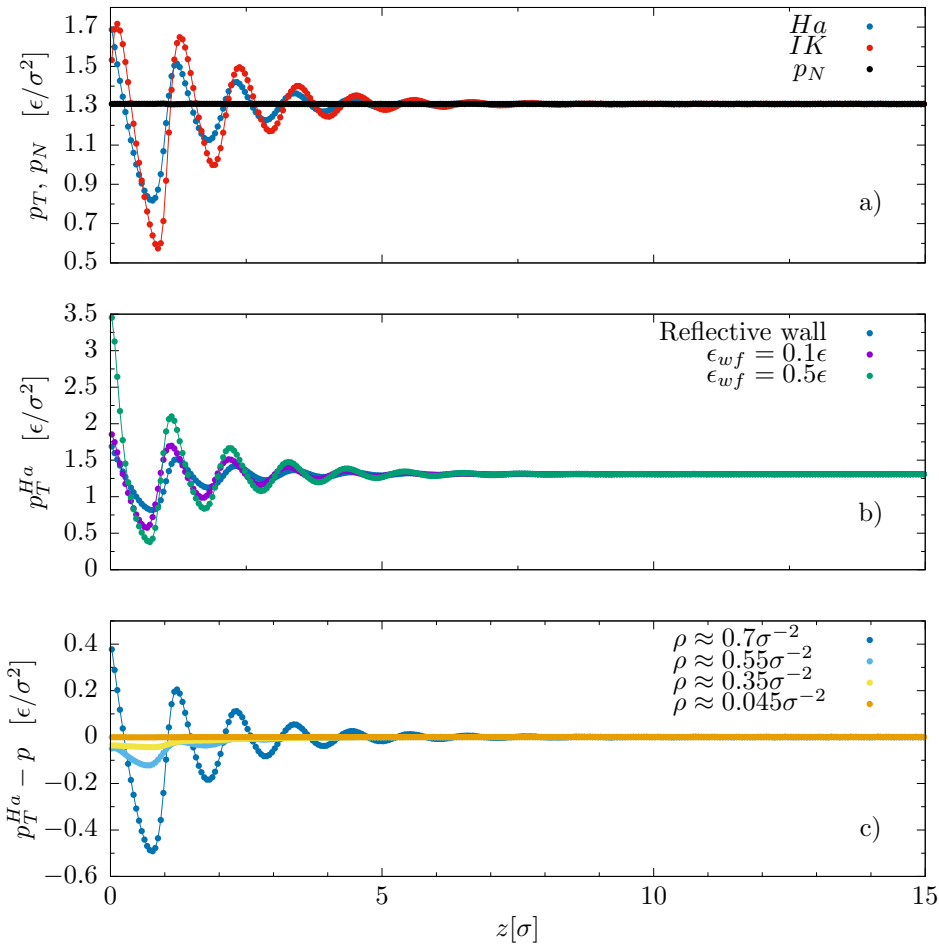

Figure 3.4: a): The anisotropy of the pressure tensor is shown considering the normal component (black dots) and both the Irving-Kirkwood (red dots) and Harasima (blue dots) formulations of the tangential one. The fluid, with a bulk density $\rho \approx 0.7\sigma^{-2}$, is kept at $T = 0.85\epsilon/k_{\mathrm{B}}$ and it is confined by a reflective wall. b): Harashima tangential pressure components for fluids (kept in the same thermodynamics conditions introduced in panel a) confined by reflective walls (blue dots) and Einstein solids characterized by $\epsilon_{wf} = 0.1\epsilon$ (purple dots) and $\epsilon_{wf} = 0.5\epsilon$ (green dots). c): Harashima tangential pressure components for fluids confined by reflective walls and kept at $T = 0.85\epsilon/k_{\mathrm{B}}$. Four bulk densities are considered: $\rho \approx 0.7\sigma^{-2}$ (blue dots), $\rho \approx 0.55\sigma^{-2}$ (light blue dots), $\rho \approx 0.35\sigma^{-2}$ (yellow dots) and $\rho \approx 0.045\sigma^{-2}$ (orange dots). For a greater legibility bulk pressures are subtracted to the corresponding tangential ones.

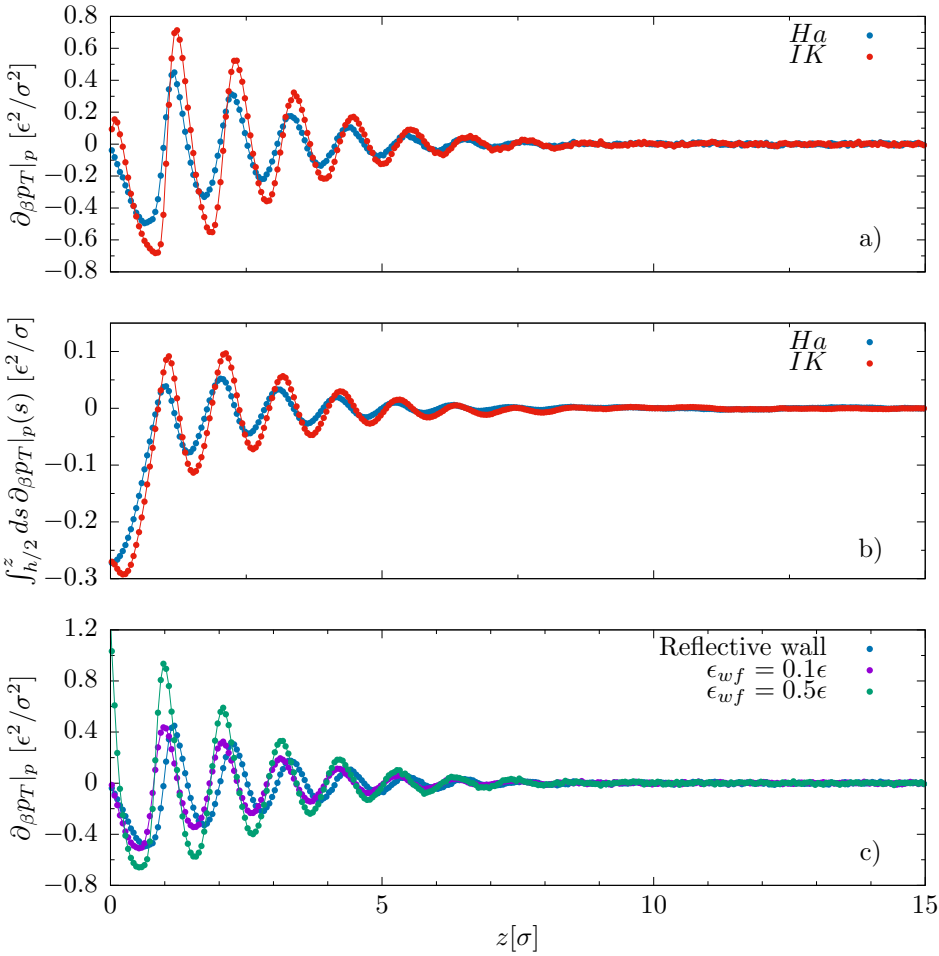

Figure 3.5: Comparison between of $\partial_\beta p_T(z)|_p$ (panel a) and $\int_{h/2}^{z} \mathrm{d}z' \partial_\beta p_T(z')|_p$ (panel b) computed with the Harasima (blue dots) and the Irving-Kirkwood (red dots) pressure tensor formulations. Fluid is confined by reflective walls. c): Effect of the confining surface on $\partial_\beta p_T(z)|_p$, computed with the Harasima tensor. The considered confinements are reflective walls (blue dots) and Einsteins walls characterized by $\epsilon_{wf} = 0.1\epsilon$ (purple dots) and $\epsilon_{wf} = 0.5\epsilon$ (green dots). In all panels profiles refer to systems kept at $T = 0.90\epsilon/k_\mathrm{B}$ and $\rho \approx 0.7\sigma^{-2}$.

is presented. Near the confining surface the results are considerably different: The more attractive is the wall the stronger are the oscillations (the reflective wall can be considered as a perfectly repulsive potential), but their range is not enhanced by more attractive walls. The corresponding profiles of the Irving-Kirkwood tensor are qualitatively similar. Finally, in the panel c of Figure 3.4 the role of the bulk density has been investigated: The oscillations around p of the Harasima tangential components of three systems, characterized by

$T = 0.85\epsilon/k_{\mathrm{B}}$, confined by reflective walls and kept at different bulk densities are shown. Lowering the density these oscillations near the surface decrease. This behavior, shared also by the Irving-Kirkwood profiles, is expected, because in the ideal gas limit also the tangential component is constant[10].
Simulations were performed also at $T = 0.95\epsilon/k_{\mathrm{B}}$ at the same bulk pressures: In this way it is possible to compute the derivative $\partial_\beta p_T(z)|_p$ at $T = 0.90\epsilon/k_{\mathrm{B}}$. It is interesting to note that also these derivatives are different when computed with the Harasima or the Irving-Kirkwood tangential components, as shown in Figure 3.5, panel a (where the bulk pressure and confinement are the same of Figure 3.4, panel a). But what is more important is that also their integrals $\int_{h/2}^{z} \mathrm{d}z' \partial_\beta p_T(z')|_p$ are different (Figure 3.5, panel b). This results numerically proof that the static source term $\mathcal{S}_s(z)$ can not be uniquely defined by the tangential pressure contribution alone. Moreover, the difference induced by different walls on the tangential pressures profiles are found also in their derivatives, as shown in panel c. Also in this case the oscillations are more important with the more attractive confinement[11]. Note that both $\partial_\beta p_T(z)|_p$ and $\int_{h/2}^{z} \mathrm{d}z' \partial_\beta p_T(z')|_p$ tend to zero when the bulk density is decreased (see the comment related to the panel c of Figure 3.4).

3.2.2 Numerical evaluation of the static source term and its invariance

The results just presented are a numerical proof of the non uniqueness of the term $\int_{h/2}^{z} \mathrm{d}z' \partial_\beta p_T(z')|_p$. Thus the invariance of the static source term $\mathcal{S}_s(z)$ must be provided, as predicted by the theory, by the integrated correlation function

$$\mathcal{C}(z) = \int \mathrm{d}\boldsymbol{r}' x' \left\langle \hat{J}_j^{xz}(\boldsymbol{r}) \left[h_m \hat{\rho}(\boldsymbol{r}') - \hat{\mathcal{H}}(\boldsymbol{r}') \right] \right\rangle_0 . \tag{3.31}$$

The computation of this quantity was accomplished through the numerical implementation of Equation 3.12, where $\mathcal{O}^2(\boldsymbol{r}) = h_m \hat{\rho}(\boldsymbol{r}) - \hat{\mathcal{H}}(\boldsymbol{r})$ and $\mathcal{O}^1(\boldsymbol{r}) = \hat{J}_j^{xz}(\boldsymbol{r})$. Obviously the computation of both $\mathcal{C}_{IK}(z)$ and $\mathcal{C}_{Ha}(z)$ (that is with $\mathcal{O}^1(\boldsymbol{r}) = \hat{J}_{j,IK}^{xz}(\boldsymbol{r})$ and $\mathcal{O}^1(\boldsymbol{r}) = \hat{J}_{j,Ha}^{xz}(\boldsymbol{r})$ respectively) is needed in order to verify the invariance of the static source term with respect to the choice of the pressure tensor definition.
Conceptually the easiest way to obtain $\mathcal{C}(z)$ would be to compute during

[10] In Equations 3.20 and 3.26 only the kinetic term survives: The pressure tensor becomes isotropic and invariant with the choice of the integration path.

[11] Actually the profile related to the Einstein wall characterized by $\epsilon_{wf} = 0.1\epsilon$ is very similar to the hard wall one, but slightly translated. The similarity is due to the fact that the potential of this Einstein wall is weakly attractive, thus it resembles a reflective wall. The translation is instead due to the position of the wall particles with respect to the position of the hard wall.

the simulation only the correlation function, and then perform its weighted spatial integral as a data post processing. However, this procedure requires a considerable amount of storage. Thus during the simulation the weighted integral is directly computed, as expressed in Equation 3.12. A further problem arises due to the integration over the x coordinate, i. e. the sum over the ξ variable. In principle the summation should run from $-\infty$ to $+\infty$. In order to define a cut-off κ we must have some information on the decay of the weighted correlation function. Therefore we performed the numerical evaluation of a sequence of correlation functions defined as

$$\tilde{\mathcal{C}}_{\kappa}(z) = \Delta^2 \left\langle \tilde{\mathcal{O}}^1_{0\zeta} \sum_{\xi'=-\kappa}^{+\kappa} \xi' \sum_{\zeta'} \tilde{\mathcal{O}}^2_{\xi'\zeta'} \right\rangle_0 . \tag{3.32}$$

Different values of κ were taken into account and the convergence is achieved when the integrals computed with κ_i and κ_{i+1} are equal, i. e.:

$$\tilde{\mathcal{C}}(z) \simeq \tilde{\mathcal{C}}_{\kappa_i}(z) \simeq \tilde{\mathcal{C}}_{\kappa_{i+1}}(z)\,. \tag{3.33}$$

Equation 3.32 is the final expression employed for the computation of $\tilde{\mathcal{C}}(z)$ during the molecular dynamic simulation and, due to the expensive time cost of this computation, just one system has been simulated.

Simulation details

Fluid particles interact through the Lennard-Jones 12-6 potential previously introduced. The simulation box is rectangular, with $L_x = 44\sigma$ and $L_z = 30\sigma$. Periodic boundary conditions are employed in the x-direction, while in z the system is confined by reflective walls. Also in this case the temperature is controlled through the Bussi-Donadio-Parrinello thermostat and it is set at $T = 0.90\epsilon/k_{\mathrm{B}}$. Instead the desired bulk pressure p is obtained by selecting the proper number of fluid particles N.
The average $\langle ... \rangle_0$ was computed exploiting both different initial conditions and the ergodicity of the fluid system. Therefore up to 1500 different initial conditions were simulated (for the largest integration domain here considered). The time step is set equal to 0.001τ and the mesh size is $\Delta = 0.05\sigma$. Each of these independent simulations is divided into two stages. In the first stage equilibration is obtained with 10^7 steps, while in the second one the evaluation of Equation 3.32 takes place during 5×10^7 time steps. Both IK and Ha correlations are computed. The number of simulated particles is $N = 726$, resulting in a bulk density $\rho \approx 0.557\sigma^{-2}$ and a bulk pressure $p \approx 0.583\epsilon/\sigma^2$. The final outputs of this simulation are then combined with the corresponding integrals $\int_{h/2}^{z} \mathrm{d}z' \partial_\beta p_T(z')|_p$ evaluated as discussed in Section 3.2.1, at the same bulk pressure and temperature.

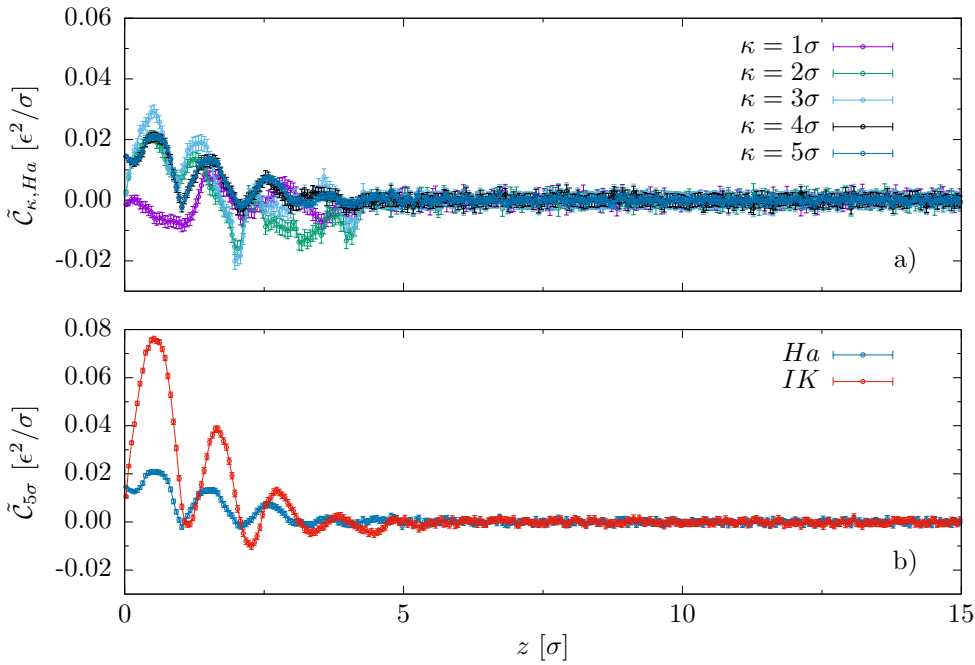

Figure 3.6: a) The effect of different integration domains $[-\kappa, +\kappa]$ on $\tilde{\mathcal{C}}_{\kappa,Ha}(z)$ is shown, considering $\kappa = 1\sigma$ (purple dots), $\kappa = 2\sigma$ (green dots), $\kappa = 3\sigma$ (light blue dots), $\kappa = 4\sigma$ (black dots) and $\kappa = 5\sigma$ (blue dots). These differences are less evident when $\tilde{\mathcal{C}}_{\kappa,IK}(z)$ is considered (data not shown). b) Comparison between $\tilde{\mathcal{C}}_{5\sigma,Ha}(z)$ (blue dots) and $\tilde{\mathcal{C}}_{5\sigma,IK}(z)$ (red dots). Thermodynamic properties of the simulated fluid are $\rho \approx 0.557\sigma^{-2}$, $p \approx 0.583\epsilon/\sigma^2$ and $T = 0.9\epsilon/k_B$

.

Results

First we identify a proper integration domain $[-\kappa, +\kappa]$ by examining five different values of κ: $\kappa = 1\sigma$, 2σ, 3σ, 4σ and 5σ. This range of the integration domain might seem small, but, as shown in Figure 3.6 panel a, the curve $\tilde{\mathcal{C}}_{4\sigma,Har}(z)$ and $\tilde{\mathcal{C}}_{5\sigma,Har}(z)$ are equal within the statistical uncertainty[12]. For sure more statistics would bring out more details of these curves, and probably a greater value of κ would be needed to achieve convergence. However the associated computation costs prevented this improvement. Note that the range of the functions $\tilde{\mathcal{C}}_{5\sigma,Har}(z)$ is about 5σ, thus the integration domain $[-5\sigma, +5\sigma]$ should be enough for evaluating $\tilde{\mathcal{C}}(z)$.
In panel b of the same Figure both $\tilde{\mathcal{C}}_{IK}(z) \approx \tilde{\mathcal{C}}_{5\sigma,IK}(z)$ and $\tilde{\mathcal{C}}_{Ha}(z) \approx \tilde{\mathcal{C}}_{5\sigma,Har}(z)$ are shown and they result to be visibly different.
Let us now consider $\int_{h/2}^{z} \mathrm{d}z' \partial_\beta p_T(z')|_p$ at $p \approx 0.583\epsilon/\sigma^2$ for the two contours

[12]The same consideration holds also for $\tilde{\mathcal{C}}_{4\sigma,IK}(z)$ and $\tilde{\mathcal{C}}_{5\sigma,IK}(z)$.

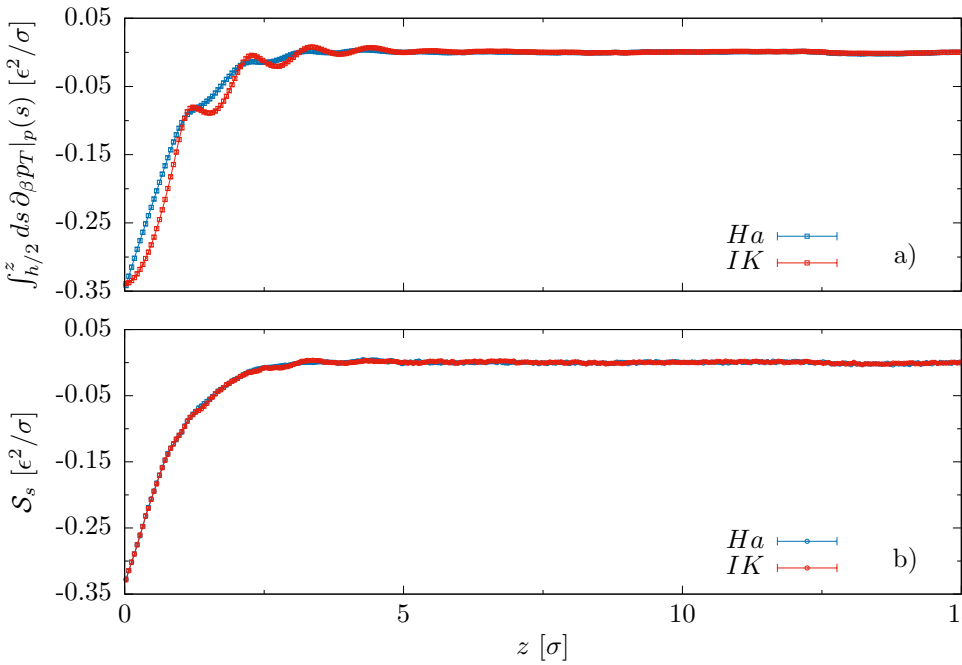

Figure 3.7: a) The first contributions $\int_{h/2}^{z} \mathrm{d}z' \partial_\beta p_T(z')|_p$ to the static source terms obtained with the IK (red dots) and Ha (blue dots) pressure tensors are shown. b) Invariance of the static source term with respect to the pressure tensor definition: The resulting $\mathcal{S}_s(z)$ computed with the IK (red dots) and the Ha (blue dots) formulations are statistically equivalent. The data in panel a are added to those of Figure 3.6b and refer to a fluid characterized by $\rho \approx 0.557\sigma^{-2}$, $p \approx 0.583\epsilon/\sigma^2$ and $T = 0.9\epsilon/k_\mathrm{B}$.

(Figure 3.7 panel a) and let us sum to them respectively $\tilde{\mathcal{C}}_{IK}(z)$ and $\tilde{\mathcal{C}}_{Ha}(z)$ in order to obtain the two static source term $\mathcal{S}_s^{IK}(z)$ and $\mathcal{S}_s^{Ha}(z)$. The result of this operation is reported in Figure 3.7, panel b: The two static source terms collapse on the same curve within the statistical accuracy. This is the numerical proof of the theoretical prediction of Chapter 2: The expression of the static source term reported in Equation 3.13 is invariant with respect to the choice of the pressure tensor definition because it is defined as the sum of two ill-defined quantities.
Note that for a system at $\rho \approx 0.557\sigma^{-2}$ confined by a reflective wall the static source term vanishes within a distance of 5σ from the confinement: This is a further confirmation of the interfacial nature of thermo-osmosis.

The control of the confined system bulk pressure p through pistons has been already employed in literature (see for example Ref. [29, 30, 32, 33]). In particular, also in Ref. [32] and [33] Ganti *et al.* computed the quantity $\partial_T p_T(z)|_p$ in order to investigate the problem of the non uniqueness of the pressure tensor: One of their objectives was to understand what is the effect

of different definitions of this quantity on the thermo-osmotic flow.
In Ref. [32] they simulated three-dimensional systems confined by an Einstein solid or a repulsive potential, and computed the derivative of the tangential pressure with respect to temperature at different values of T, considering the Irving-Kirkwood and the virial pressure tensors[13]. Then they applied these mechanical forces to a confined fluid in order to mimic a thermo-osmotic mass flow, and compared the resulting slip velocities far from the surface with the results obtained with other methods. They concluded that all the slip velocities were in agreement.
Instead, in the more recent paper [33] they compared the mechanical forces $\partial_T p_T^{IK}(z)|_p$ and $\partial_T p_T^{V}(z)|_p$ with the exact effective force exerted by a temperature gradient, computed through a suitable nonequilibrium simulation. They found that neither of the two adopted definitions of the pressure tensor was able to recover the exact result.
We recall that there are, in principle, infinite correct definitions of this quantity but, physical observable are not affected by this freedom in the choice of the pressure tensor, as shown by our theoretical prediction and numerical results just discussed, because of the presence of corrective quantities.

3.3 THE PROBLEM OF TRANSPORT COEFFICIENTS IN TWO-DIMENSIONAL SYSTEMS

Until the end of the 1960s it was believed that, far from the critical points, the dynamic autocorrelation functions of non-conserved variables decay exponentially at long times[14]. This expectation was questioned when Alder and Wainwright published their molecular-dynamics results related to the self diffusion of hard particles in two and three-dimensional systems [1, 2]: They showed that the velocity dynamic autocorrelation function decays at long times as $t^{-\frac{\mathrm{D}}{2}}$, being D the dimensionality of the system. The presence of these slowly-decaying tails suggests that collective effects play a relevant role in the process of self diffusion. Alder and Wainwright gave a simple but interesting interpretation of their results: Basically they suggested that the initial motion of a given particle gives rise to a vortex or backflow around it. This vortex in turn causes the development of a current in the direction of the initial velocity of the tagged particle. This current would lead to the $t^{-\frac{\mathrm{D}}{2}}$ decaying behavior. After this important numerical result a series of works

[13] Actually, as already stated in Chapter 2, the virial pressure tensor does not correspond to any choice of the integration contour $\boldsymbol{\ell}_{i\to l}$, thus it does not define an admisible form of the microscopic pressure tensor. However it is possible to show that in the planar geometry considered in Ref. [32] the tangential components of the virial and the Harasima formulations of the pressure tensor are identical.

[14] It is instead well known that fluctuations in the conserved hydrodynamic variables decay infinitely slowly in the long wavelength limit.

tried to analytically investigate this behavior [22, 18, 66], apparently shared also by the momentum and energy flux dynamic autocorrelation functions. The presence of long-time tails is particularly important in 2D systems: Its consequence is that at this dimensionality the transport coefficients related to those dynamic autocorrelation functions cannot be defined, at least in their microscopic formulation given by the linear response theory through the Green-Kubo integrals, because indeed they would lead to divergence. Therefore it is important to give some more detail about this question. In this regard we will provide a brief summary of the treatment of the viscosity given by Pomeau[15]. Thus, let us roughly introduce the Landau and Placzek method [46], which provides a powerful tool in the analysis of the dynamic autocorrelation functions. Accordingly to this method we can start considering a dynamic autocorrelation function $\langle X(\boldsymbol{r},0)Y(t)\rangle_0$ where $X(\boldsymbol{r},0)$ depends on the initial dynamic state of the many-body system in the neighborhood of $\boldsymbol{r}$ and $Y(t)$ on the dynamic state of the system at time t. We divide the system into cells, large enough to be considered statistically independent. Thus $X(\boldsymbol{r},0)$ only depends on the initial state of a given cell ΔV^0 and $\boldsymbol{r} \in \Delta V^0$. The method replaces $Y(t)$ by its average value over a nonequilibrium ensemble initially in a given nonequilibrium situation around $\boldsymbol{r}$ and at equilibrium far from $\boldsymbol{r}$[16]. Assuming that for long times this nonequilibrium ensemble relaxes to equilibrium according to the laws of hydrodynamics, we can replace $Y(t)$ in this limit by its value over the corresponding local equilibrium ensemble. That is, the correlation function related to the viscosity in an homogeneous system[17]

$$\psi(t) = \left\langle \sum_i \delta(\boldsymbol{r}-\boldsymbol{r}_i) X_i(\Omega_N^0) \sum_j X_j\left(\Omega_N^*(t,\Omega_N^0)\right) \right\rangle_0 \tag{3.34}$$

for large times can be expressed as

$$\psi(t) \overset{t\to\infty}{\simeq} \left\langle \sum_i \delta(\boldsymbol{r}-\boldsymbol{r}_i) X_i(\Omega_N^0) Z(t, \Omega_N^0 \cap \Delta V^0) \right\rangle_{\Delta V^0} \tag{3.35}$$

where Ω_N^0 is the phase-space point of the N-particle system at $t'=0$, its coordinates at time $t'=t$ are $\Omega_N^*(t,\Omega_N^0)$ and $\Omega_N^0 \cap \Delta V^0$ is the set of initial positions and momenta of particles lying in the cell ΔV^0. Moreover $\langle ... \rangle_{\Delta V^0}$ is the average over the equilibrium ensemble located in the cell ΔV^0 while $Z(t, \Omega_N^0 \cap \Delta V^0)$

[15] More details and the treatment of other transport coefficients can be found in [66] and [36].

[16] The underlying idea is that at $t=0$ the quantity $Y(t=0)$ is characterized in $\boldsymbol{r}$ by a fluctuation with respect to its equilibrium value.

[17] Here $\hat{J}_j^{xz} = \sum_i X_i$ and we recall that the freedom in the choice of the integral contour in the definition of $\hat{J}_j^{xz}$ does not hamper the uniqueness of the definition of transports coefficients.

is the time-dependent local equilibrium average of $\sum_j X_j(\Omega_N^*(t,\Omega_N^0))$.

The local equilibrium ensemble over which Z is computed is defined by a set of $\mathrm{D}+2=4$ functions of $\boldsymbol{r}$, t and $\Omega_N^0 \cap \Delta V^0$. This set of functions will be called hydrodynamical field and it is defined by

$$f(\boldsymbol{r},t) \equiv \{S(\boldsymbol{r},t), p(\boldsymbol{r},t), \boldsymbol{u}(\boldsymbol{r},t)\}\ , \tag{3.36}$$

being $S(\boldsymbol{r},t)$ the local entropy for unit mass, $p(\boldsymbol{r},t)$ the local pressure and $\boldsymbol{u}(\boldsymbol{r},t)$ the local velocity field of the fluid. Moreover we can introduce the perturbation of the hydrodynamical field, defined as $\delta f(\boldsymbol{r},t) = f(\boldsymbol{r},t) - f$, being f the equilibrium value of $f(\boldsymbol{r},t)$ and we assume that $f(\boldsymbol{r},t)$ varies smoothly in space, thus the space-dependent thermodynamical quantities are related through the equilibrium equations of state. Furthermore we also assume that $\delta f(\boldsymbol{r},t) \overset{t\to\infty}{\to} 0$, therefore for long times δf can be described by the linearized equations of hydrodynamics. These equations are easier to handle if the Fourier transform of the hydrodynamical quantities is considered

$$\delta f(\boldsymbol{k},t) = \int \mathrm{d}\boldsymbol{r} \mathrm{e}^{2\pi i \boldsymbol{k}\cdot\boldsymbol{r}} \delta f(\boldsymbol{r},t)\,. \tag{3.37}$$

In particular, if the viscosity is considered, the relevant hydrodynamic quantity in the local equilibrium average Z is the velocity field[18]

$$Z(T,\Omega_N^0 \cap \Delta V^0) \overset{t\to\infty}{\simeq} \rho \int \mathrm{d}\boldsymbol{k} u_x^*(\boldsymbol{k},t) u_y(\boldsymbol{k},t) \tag{3.38}$$

and if also the limit $\boldsymbol{k} \to 0$ is considered it is possible to show that

$$Z(T,\Omega_N^0 \cap \Delta V^0) \overset{t\to\infty}{\simeq} \alpha \frac{\delta P_x \delta P_z}{D(D+2)\rho} \left(\frac{\rho}{8\pi t}\right)^{\frac{D}{2}} \tag{3.39}$$

where α is a constant and δP_x and δP_z are the fluctuations at $t=0$ in ΔV^0 of the x and z component of the average momentum of the particles in ΔV^0. It follows that the Green-Kubo integrand which defines the viscosity decays in time as

$$\psi(t) \overset{t\to\infty}{\sim} t^{-\frac{D}{2}} \tag{3.40}$$

and thus the viscosity

$$\eta = \beta \int_0^\infty \mathrm{d}t\, \psi(t) \tag{3.41}$$

[18]The configurational contribution decays in time faster than the kinetic one, thus it can be neglected in the long time limit.

diverges logarithmically in two-dimensional systems. This result thus implies that it is not possible to define viscosity[19] through the linear response theory formalism if 2D systems are considered.

This rough summary of Pomeau's work does not want to be exhaustive, but simply to emphasize the relevant role played by hydrodynamics (for long times the motion of the many-body system was described by the linearized laws of hydrodynamics) in the treatment of this problem. Therefore the validity of this result can be questioned and so a series of papers tried to clarify this question by numerical simulations.

The first works were published by D. J. Evans and G. P. Morris [23, 56] in the eighties. They performed nonequilibrium dynamical simulations applying a shear stress to a fluid of soft-disk[20], and they confirmed the long-time tail predicted by theories.

In the nineties this question was again considered through both nonequilibrium and equilibrium simulations of large soft-disk systems [39, 40, 34, 28] and the general conclusions of these works led to partially overturn the previous convictions: These simulations suggest the existence of the viscosity coefficient in 2D fluids, but not of the self-diffusion coefficient. In particular Ciccotti *et al.* computed in periodic systems the velocity and shear stress dynamic autocorrelation functions up to $t = 10\tau$. Regarding the first quantity they confirmed a t^{-1} behavior, while data related to the shear stress dynamic autocorrelation function did not allow to obtain clear results about its time decay. However they concluded that the viscosity in 2D soft-disk fluid exists, because the time integral of its dynamic autocorrelation function reaches a plateau within $t \approx 3\tau$.

The question of the velocity dynamic autocorrelation function was definitely clarified by Masaharu Isobe in 2008 [43]: It was computed up to $t = 5 \times 10^3 \tau$ in large periodic systems (N up to about 10^6) of hard-disk through equilibrium simulations, and a time decaying faster than t^{-1} was clearly observed. In this work a relevant point related to the computation of dynamical autocorelation functions in periodic system is underlined: Being c the speed of sound and L_{box} the side of the simulation box, it is possible to define a recurrence time $t_r = \frac{L_{box}}{c}$ and the computed dynamic autocorrelation functions are reliable only up to $t \approx t_r$. Indeed this recurrence time defines the time needed to a sound wave to propagate along the simulation box, and after t_r non-physical effects induced by the periodic boundary conditions arise in the dynamic autocorrelation functions.

In literature it is possible to find more recent works also related to the problem of viscosity in two-dimensional fluids. In particular, Goree *et al.* published a series of experimental [57, 37] and numerical [50, 17, 27] works concerning 2D fluids of particles interacting through a Yukawa potential $\varphi(r) =$

[19] Actually in general transport coefficients, see [66].

[20] That is particles interact through the potential $\varphi(r) = \epsilon \left[\frac{\sigma}{r}\right]^{12}$.

$A\, r^{-1}\exp\{-r/B\}$. Also in these numerical papers equilibrium simulations are performed on periodic systems. They found that the existence of viscosity depends on the temperature of the Yukawa system: It exists in cool fluids but not in hot ones. Moreover, they tackled also the problem of the diffusion and thermal conductivity coefficients and they concluded that the first one exists in hot systems but not in cool ones, while data did not allow to obtain clear results for the thermal conductivity. It is important to notice that they recognize that definitive results could require greater system sizes L_{box}, in order to avoid artifact introduced by the sound wave propagation in periodic systems.
Therefore the numerical efforts did not produce a definite answer to the problem of the existence of transport coefficient in 2D fluids. Nevertheless they strongly suggest that they exist at least in some temperature and inter-particle potential conditions. In the next Chapter we will present nonequilibrium simulations of Lennard-Jones two-dimensional fluids kept at a temperature of the order of $T = 0.9\epsilon/k_{\rm B}$. To our knowledge the problem of transport coefficients in a two-dimensional fluid characterized by this interaction particles potential (and temperature) has never been tackled, thus it is interesting to get some hints about, at least, the existence of the viscosity coefficient.

3.3.1 Viscosity in two-dimensional Lennard-Jones fluids

In the computation of dynamic autocorrelation functions two relevant characteristic times must be considered. The first one is the collision time t_c [34], which is a measure of the mean time between two consecutive collisions of the same particle, and it can be defined as

$$t_c = \frac{1}{c\sqrt{\rho}}\,, \tag{3.42}$$

being $1/\sqrt{\rho}$ the average distance between particles and c the speed of sound[21]. The second characteristic time is the already introduced recurrence time t_r:

$$t_r = \frac{L_{box}}{c}\,. \tag{3.43}$$

[21] In this definition of the collision time, adopted by Gravina *et al.* in Ref. [34], the average distance between particles is divided by the speed of sound and not, as might be expected, by the ballistic velocity of the particle, which in a two-dimensional system is

$$v_b = \sqrt{\frac{2}{m\beta}}\,.$$

However, at $T = 0.9\epsilon/k_{\rm B}$ its value is $v_b = 1.342\sigma/\tau$ and it is comparable to the value of the speed of sound c that will be computed in the following. Therefore, due to the qualitative nature of the role played by the collision time t_c in our discussion, both definitions are equally acceptable.

In order to observe the time-tail behavior it is important to compute the dynamic autocorrelation function up to $t \gg t_c$. In this way a particle can undergo a great number M of collisions. But we must also take into account that the computation time t must be smaller than the recurrence time if periodic systems are considered. Thus the following condition must be satisfied if periodic boundary conditions are applied to the system

$$t_c \ll t \leq t_r \,. \tag{3.44}$$

Now, exploiting Equations 3.42 and 3.43, we can simply relate the number of collisions M that take place within t_r to the box size L_{box}:

$$M = L_{box}\sqrt{\rho} \tag{3.45}$$

and, considering a square box, also to the number of particles N in the system

$$N = M^2 \,. \tag{3.46}$$

Equation 3.46 is particularly useful because connects the size of the system to the number of collisions that will take place within t_r.
The problem is that it is not possible to know *a priori* how large M must be in order to compute the dynamic autocorrelation function up to a sufficient value of t, that is up to its asymptotic time behavior. As a consequence it is not possible to know how large the system must be.
Another possible route is to consider closed systems. This solution does not solve the problem of recurrence effects, because now particles will bounce against the confining surfaces. Nevertheless, in this case the recurrence effects acquire a genuine physical nature. Thus, dynamic correlation functions maintain a fully physical meaning also for $t > t_r$, and consequently a less restrictive condition on the correlation time can be adopted:

$$t_c \ll t \,. \tag{3.47}$$

However we stress that the dynamic correlation functions computed in a closed systems are expected to be dependent both on the position and on the system size due to the recurrence effects. Moreover, also the resulting viscosity coefficient (if existing) would be characterized by these dependencies.
Despite this, we decided to try to verify the existence of the viscosity coefficient in 2D Lennard-Jones fluids considering closed systems. Actually, we numerically computed the *spatial-averaged* dynamic autocorrelation function of our interest as

$$\langle \psi(t, \boldsymbol{r}, L_{box}) \rangle_{\boldsymbol{r}} = \frac{\Delta^4}{A} \langle \Pi_t^{xz} \Pi^{xz} \rangle_0 \,, \tag{3.48}$$

where we recall that

$$\Pi^{xz} = \sum_l \tilde{J}_{j,l}^{xz} \,, \tag{3.49}$$

while the symbol $\langle ... \rangle_{\boldsymbol{r}}$ emphasizes the space-averaged nature of this quantity. As we will see later, the noise of this output does not allow to evaluate the long-time behavior of $\langle \psi(t, \boldsymbol{r}, L_{box}) \rangle_{\boldsymbol{r}}$. Therefore we decided to test the existence of the viscosity coefficient looking directly at the time integral (multiplied by β) of the dynamic autocorrelation function

$$\langle \eta(\boldsymbol{r}, L_{box}; t) \rangle_{\boldsymbol{r}} = \frac{\Delta^4}{A} \beta \sum_{n=0}^{t} \langle \Pi_n^{xz} \Pi^{xz} \rangle_0 \, \delta t \,, \tag{3.50}$$

which is also a space-averaged quantity. Moreover, we can assume that Equation 3.50 defines the spaced-averaged viscosity coefficient $\langle \eta(\boldsymbol{r}, L_{box}) \rangle_{\boldsymbol{r}}$ only if the integral reaches a plateau at a certain value of time $t = t_p$, and then we can assume that

$$\langle \eta(\boldsymbol{r}, L_{box}) \rangle_{\boldsymbol{r}} = \langle \eta(\boldsymbol{r}, L_{box}; t \geq t_p) \rangle_{\boldsymbol{r}} \; : \tag{3.51}$$

Indeed the presence of a plateau suggests that the dynamic autocorrelation function rapidly converges to 0 for $t > t_p$ and so the existence of the viscosity coefficient.
The resulting coefficient $\langle \eta(\boldsymbol{r}, L_{box}) \rangle_{\boldsymbol{r}}$ would be dependent on the system length L_{box} because of the recurrence effects and the space dependency of the dynamic autocorrelation function induced by the presence of the confining surfaces. However, when large systems are considered this space-averaged quantity and the bulk viscosity η are expected to become equal, i. e.

$$\langle \eta(\boldsymbol{r}, L_{box}) \rangle_{\boldsymbol{r}} \overset{Lbox \to \infty}{=} \eta \,. \tag{3.52}$$

Unfortunately, we do not know how $\langle \eta(\boldsymbol{r}, L_{box}) \rangle_{\boldsymbol{r}}$ depends on L_{box}, and consequently we cannot extrapolate the value of η by numerical simulations of systems with different lengths.
However, we computed the value of the viscosity in closed systems in the nonequilibrium simulations presented in the next Chapter[22]. The system is characterized by $\bar{T} \approx 0.9\epsilon/k_{\mathrm{B}}$ and $\bar{\rho} \approx 0.548\sigma^{-2}$ [23] and the resulting viscosity coefficient is $\eta_{\mathrm{neq}} = 0.7855 \pm 0.0448\tau\epsilon/\sigma^2$. We stress that in principle also η_{neq} can depend on the system size and thus it cannot be considered representative of the bulk viscosity value. Despite this, a comparison between the viscosity coefficient obtained through the Green-Kubo relation 3.50 and this nonequilibrium value could be helpful: If result are comparable the idea of the existence of the viscosity coefficient in these systems would be strengthen.
In order to get some hints about the reliability of Equality 3.51 it is useful to understand how large is the average number of collisions per particle M

[22] In the bulk of the system a parabolic velocity field develops and, thanks to the Poiseuille law, viscosity can be obtained by fitting the velocity profile.
[23] $\bar{T}$ and $\bar{\rho}$ because are the average value in those nonequilibrium systems.

within t_p, but estimating it requires the knowledge of the sound velocity c in this Lenard-Jones fluid, and[24]

$$c = \sqrt{\frac{C_p}{C_V}\frac{1}{m}\left.\frac{\partial p}{\partial \rho}\right|_T}, \tag{3.53}$$

where m is the mass of the particles (set to 1) while C_p and C_V are the heat capacities at constant pressure and volume respectively, defined as

$$C_p = \left.\frac{\partial H}{\partial T}\right|_p \tag{3.54}$$

and

$$C_V = \left.\frac{\partial U}{\partial T}\right|_V, \tag{3.55}$$

where U and H are respectively the internal energy and the enthalpy of the system. We decided to compute the speed of sound c employing the definitions given in Equations 3.54 and 3.55 of the heat capacities. Thus we had to simulate two systems at the same pressure and different temperatures to compute C_p and two systems at the same pressure and different temperatures to obtain C_V. Moreover, in order to get c we simulated also two systems at different densities but at the same temperature.

Simulation details

Thus, six different systems have been simulated. All of them are square box with $L_{box} = 80\sigma$ and they are confined by repulsive walls. This kind of confinements is characterized by a reflective wall (placed for example at $z = 0$) plus a repulsive potential of the form

$$V_r(z) = \begin{cases} V_r(z) = k(z - z_r)^2 & 0 < z \leq z_r \\ 0 & z > z_r \end{cases} \tag{3.56}$$

with $k = 0.1\epsilon/\sigma^2$ and $z_r = 5\sigma$. This wall will be employed also in the evaluation of the dynamic correlation functions, where the energy conservation must be ensured: With pure reflective walls the energy conservation in a NVE ensemble (required in the dynamical correlation computation) is only satisfied to $O(\delta t)$, rather than to $O(\delta t^2)$ as it would be for simulation of systems without reflective walls [8]. This happens basically because of the particles that collide against the reflective wall. The repulsive potential minimizes these collisions and thus improves the energy conservation.

[24] See for example [47], p. 247.

In all systems the temperature control is achieved through the Bussi-Donadio-Parrinello thermostat and they were characterized by an equilibration stage of 2×10^7 time steps, each of duration 0.001τ, and by 2×10^8 time steps of the same duration for the production phase. For the computation of C_p a system with $N = 3510$ and $T = 0.85\epsilon/k_\mathrm{B}$ and another with $N = 3193$ and $T = 0.95\epsilon/k_\mathrm{B}$ were simulated. The number of particle was gauged in order to get the same bulk pressure p in both systems and to be equal to $\bar{p}$, i. e. the average value obtained in the nonequilibrium simulations where η was computed. For C_V the two systems are characterized by same number of particle $N = 3350$ but by different temperatures $T = 0.85\epsilon/k_\mathrm{B}$ and $T = 0.95\epsilon/k_\mathrm{B}$. This number of particles leads to $\rho \approx \bar{\rho}$. For the derivative of p with respect to ρ at constant temperature the two systems were kept at $T = 0.90\epsilon/k_\mathrm{B}$ with $N = 3180$ and $N = 3520$.

Results

The main outputs of these simulations are the internal energy, enthalpy, pressure and density profiles. All the derivatives appearing in the definition of c are computed considering the bulk values of these quantities, and the heat capacity at constant pressure per unit of area results to be $\tilde{C}_p \approx 1.948 k_\mathrm{B}/\sigma^2$, the one at constant volume $\tilde{C}_V \approx 0.904 k_\mathrm{B}/\sigma^2$, while the derivative of bulk pressure with respect to the bulk density at constant temperature is $\partial_\rho p|_T \approx 2.858\epsilon$[25]. Follows from Equation 3.53 that $c \approx 2.482\sigma/\tau$.
The bulk density of the system is $\rho \approx 0.548\sigma^{-2}$, thus follows from Equation 3.42 that the average time between two consecutive collisions of the same particle is $t_c \approx 0.544\tau$.

Let us now present our numerical results related to the viscosity. As previously explained they are not fully exhaustive, but their objective is simply to strengthen the possibility that viscosity can be defined in this kind of systems.

Simulation details

Simulation cells are square closed boxes of side L_{box} and confinements are provided by the repulsive walls previously introduced. The number of Lennard-Jones particles is gauged in order to get a bulk density $\rho \approx 0.548\sigma^{-2}$ and, in order to study the effect of the system size, four values of L_{box} are considered: $L_{box} = 40\sigma$, 60σ, 80σ and 100σ. The computation of the dynamic autocorrelation function is performed through Equation 3.48, and the equilibrium averages are computed exploiting both the ergodicity of the

[25] That is slightly greater than the ballistic velocity v_b, probably because of collective effects.

$L_{box}\,[\sigma]$	$\tau_0\,[\tau]$	A_p	$\langle\eta(\boldsymbol{r}, L_{box})\rangle_{\boldsymbol{r}}\,[\tau\epsilon\sigma^{-2}]$
40	30	-0.024	$0.5545 \pm 4 \times 10^{-4}$
60	40	-0.016	$0.5860 \pm 4 \times 10^{-4}$
80	50	-0.011	$0.6208 \pm 4 \times 10^{-4}$
100	60	-0.008	$0.6453 \pm 5 \times 10^{-4}$

Table 3.2: Dependence on L_{box} of oscillations period τ_0, the amplitude of the first oscillation A_p and spaced-averaged viscosity $\langle\eta(\boldsymbol{r}, L_{box})\rangle_{\boldsymbol{r}}$ in the simulated confined systems. The last column can be compared with the viscosity value obtained in the nonequilibrium simulations presented in the next Chapter, $\eta_{\text{neq}} = 0.7855 \pm 0.0448\tau\epsilon/\sigma^2$.

fluid systems and different initial conditions. Thus, for each value of L_{box} 144 independent simulations were run, each characterized by the usual two stages. The first one is the equilibration phase and it lasts 2×10^7 time steps during which the temperature is controlled through the Bussi-Donadio-Parrinello thermostat and it is set at $T = 0.9\epsilon/k_{\text{B}}$. The second stage is the production one. This phase is characterized by a NVE integration of the particles equations of motion[26] and it lasts 5×10^7 time steps. In both these stages the time step duration is $\delta t = 0.001\tau$. The spatial-integrated operator Π^{xz} is computed during the production phase every 10 time steps over the whole system area, while the autocorrelation operation and the time integration are performed as data post processing.

Results

The spaced-averaged dynamic autocorrelation function $\langle\psi(t, \boldsymbol{r}, L_{box})\rangle_{\boldsymbol{r}}$, normalized by its initial value, is shown for the system with $L_{box} = 60\sigma$ in Figure 3.8, panel a. As anticipated, it is clearly not possible to obtain clean results regarding the long-time behavior of $\langle\psi(t, \boldsymbol{r}, L_{box})\rangle_{\boldsymbol{r}}$ because of the noise, and the situation is similar when systems with others L_{box} are considered. Nevertheless an interesting feature of $\langle\psi(t, \boldsymbol{r}, L_{box})\rangle_{\boldsymbol{r}}$ can be observed: It is characterized by evident, even if small, oscillations, as shown in the panel b of Figure 3.8, where the systems with $L_{box} = 40\sigma$ and $L_{box} = 60\sigma$ are considered. What is more interesting is that the period τ_o of these oscillations increases with L_{box}, as reported in Table 3.2 (approximate values). The suggestion coming from this increase of τ_0 is that these oscillations can be interpreted as recursive effects induced by the propagating sound waves in a closed system. Therefore, as expected, the space-averaged dynamic autocorrelation function $\langle\psi(t, \boldsymbol{r}, L_{box})\rangle_{\boldsymbol{r}}$ depends on the system length. It follows that also the resulting viscosity coefficient is characterized by this dependence. Indeed, enlarging the

[26]The absence of thermostats ensures the tracking of correct particles trajectories.

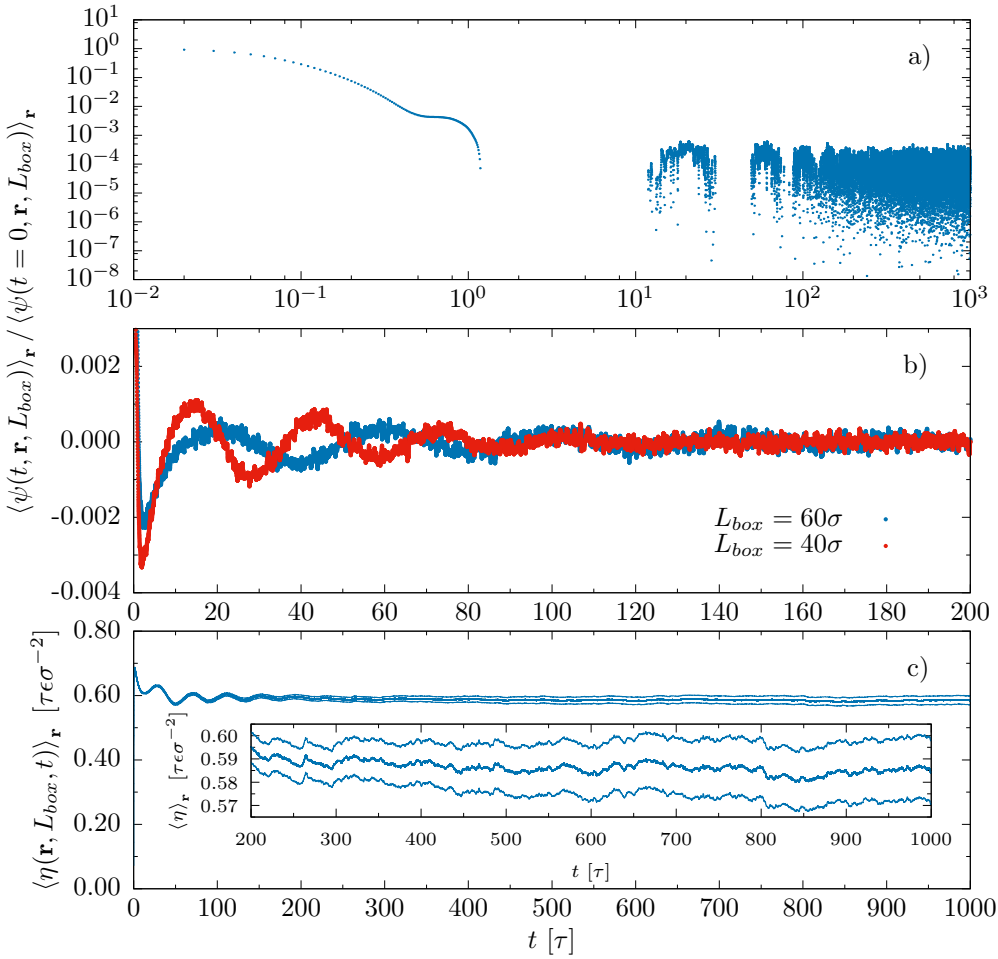

Figure 3.8: a) Normalized dynamical autocorrelation function of the xz component of the pressure tensor for the system with $L_{box} = 60\sigma$. Note that data are shown in a log-log scale, thus negative values of the normalized dynamical autocorrelation function do not appear in the graph. b) Oscillations in $\psi(t)/\psi(0)$ for systems with $L_{box} = 60\sigma$ (blue dots) and $L_{box} = 40\sigma$ (read dots). c) Viscosity obtained through the Green-Kubo relation integrated up to different times t for the system with $L_{box} = 60\sigma$ (solid lines indicate the errors). The inset shows that the long time behavior is not characterized by further oscillations (at least within statistical uncertainty). For the sake of simplicity the inset ordinate label is $\langle \eta \rangle_{\boldsymbol{r}}$ instead of $\langle \eta(\boldsymbol{r}, L_{box}, t) \rangle_{\boldsymbol{r}}$. Fluid bulk density and temperature are respectively $\rho \approx 0.548\sigma^{-2}$ and $T = 0.90\epsilon/k_{\mathrm{B}}$.

system these recursive effects become less important, as testified by a decrease of the oscillations amplitude with the increase of L_{box}, as reported in the Table where the amplitude of the first (negative) oscillation peak is reported for the different L_{box}.
Let us now consider the problem of viscosity. As previously shown, the noisiness of the time tail of the dynamic autocorrelation function $\langle \psi(t, \boldsymbol{r}, L_{box}) \rangle_{\boldsymbol{r}}$ does not allow to come to a conclusion about its existence. Thus we decided to consider the time-dependent quantity expressed in Equation 3.50, $\langle \eta(\boldsymbol{r}, L_{box}, t) \rangle_{\boldsymbol{r}}$, shown in the panel c of Figure 3.8 for the $L_{box} = 60\sigma$ system (the other systems are characterized by similar results). A clear plateau begins at $t_p \approx 250\tau$ and this suggests that a value of the viscosity can be computed through the Green-Kubo relation also in this kind of systems. Note that during this time frame a particle in the bulk undergoes about $M_p \approx 450$ collisions[27]. The resulting space-averaged values $\langle \eta(\boldsymbol{r}, L_{box}) \rangle_{\boldsymbol{r}} = \langle \eta(\boldsymbol{r}, L_{box}, t \geq t_p) \rangle_{\boldsymbol{r}}$ are reported in the Table for the different systems. They result to be smaller than the nonequilibrium value η_{neq}. The increasing trend of $\langle \eta(\boldsymbol{r}, L_{box}) \rangle_{\boldsymbol{r}}$ with L_{box} suggests that η_{neq} is less affected by size effects, and thus a better approximation of the real bulk viscosity. However, the Green-Kubo and nonequilibrium values are comparable. These results are for sure not exhaustive, but overall they suggest that viscosity can be defined in the kind of systems considered in the present work, because of both the plateau reached by $\langle \eta(\boldsymbol{r}, L_{box}, t) \rangle_{\boldsymbol{r}}$, the increase of $\langle \eta(\boldsymbol{r}, L_{box}) \rangle_{\boldsymbol{r}}$ with the box size and the comparable values with η_{neq}.

For the sake of simplicity, in the following Chapter we will refer to η_{neq} as bulk viscosity η.

[27] That is, a system of $N \approx 250000$ particles would be needed to simulate a periodic system and obtain the viscosity value without non-physical recursive artifacts.

4

Nonequilibrium simulations

The theoretical approach developed in chapter 2 allows to describe thermo-osmosis both in open and closed channel configurations. The emerging scenario is extremely complex, and a numerical study of this phenomenon can be useful to rationalize some relevant aspect, such as the role played by thermodynamic conditions of the fluid and the properties of confinements. In this context, the molecular dynamics technique is the most natural choice, because of the nonequilibrium and microscopic nature of thermo-osmosis. The reliability of this numerical tool for the study of thermo-osmosis is testified by the fact that this phenomenon was observed as a side effect in nonequilibrium simulations performed by Wold and Hafskjold [82] and by Galliéro *et al.* [31][1]. The authors of Ref. [31] employed periodic boundary conditions in the direction of the temperature gradient, simulating in such a way an open channel, and they observed a velocity field characterized by a backflow in the middle of the channel. This shape of the velocity profile is not due to real physical effects, but it is an artifact induced by the presence of periodic boundary conditions in the direction of the temperature gradient: At the ends of the simulation box in the periodic direction fluid portions kept at the hottest and coldest temperatures are in contact, therefore in this tight region a steep temperature gradient develops, but it is in opposition to the thermal gradient that characterizes the main part of the system. It follows that an artificial themo-osmotic flow develops in opposition to the physical one.

[1] In fact both groups were studying thermodiffusion.

The first nonequilibrium simulations specifically devised for the investigation of thermo-osmosis were performed by Fu *et al.* [29]. They were able to simulate three-dimensional fluids in an open-channel-like configuration: A channel is connected to two large particles reservoirs, kept at different temperatures, but at the same pressure by means of two pistons. In this way the fluid in the channel is characterized by a temperature gradient and by constant bulk pressure. Unfortunately, also with this clever solution the velocity profile resulted to be affected by viscous effects, induced by the different geometries of the channel and the reservoirs. Despite this they were able to correct this effect and to check the validity of Derjaguin's expression for the slip velocity: Accordingly to their results this expression must be modified in order to take into account also hydrodynamic effects induced by the surface. Moreover, they showed that the flow is directed towards the cold side when the wall-fluid interaction is weakly attractive, while it is reversed and weakened with more attractive wall-fluid interactions surfaces.
In order to avoid these difficulties related to the open-channel configuration, we decided to simulate closed systems, as already done by Wold and Hafskjold [82]. In this way, because of mass conservation, a bulk pressure gradient develops giving rise to a Poiseuille backflow in the middle of the channel. This is a genuine physical effect and this bulk pressure gradient can be useful in order to devise future experiments on thermo-osmosis. This property of our configuration will be studied in the last Section of this Chapter. Moreover, due to the large number of simulated systems and the need to obtain results statistically meaningful[2], we decided to simulate two-dimensional fluids. This choice could seem dangerous: The applicability of linear response theory and the existence of transport coefficients in two-dimensional systems is still an open question. Nevertheless, the most recent results on this topic and our studies related to the viscosity coefficient, presented in the previous Chapter, suggest this possibility, at least for the model system we investigated, i. e. two-dimensional Lennard-Jones fluids kept at a temperature $T \approx 0.9\epsilon/k_{\mathrm{B}}$. Therefore we feel confident in the interpretation of the numerical results presented in the following through our microscopic theory of thermo-osmosis. Moreover, in the following we will not attempt a quantitative comparison between theory and simulations, limiting our analysis at a qualitative level.

4.1 NONEQUILIBRIUM SIMULATIONS DETAILS

In this set of simulations the fluid-fluid interaction is modeled through the already introduced truncated and shifted Lennard-Jones 12-6 potential. The simulation boxes are two-dimensional rectangular cells (see Fig. 4.1) of width h and length L_x. Different values of these parameters will be considered.

[2]Often the signal-to-noise ratio is a challenge.

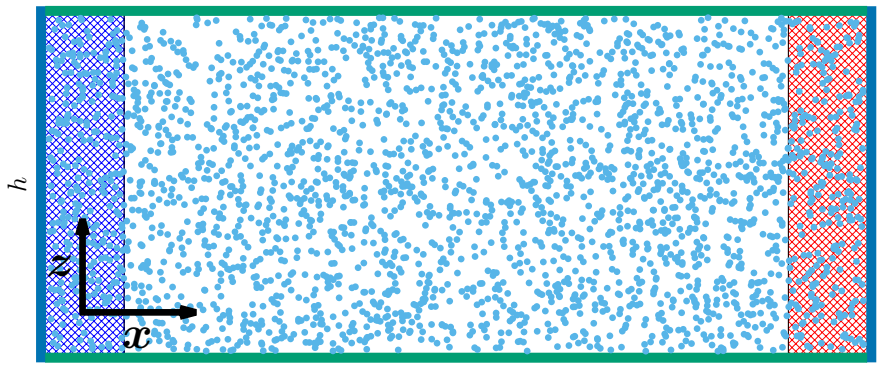

Figure 4.1: Schematic of a typical system. Blue and red rectangles represent the thermostated regions (cold and hot, respectively) while fluid particles are symbolized by the light blue spheres. Blue contours represent reflective walls and the green ones are different kind of confining surfaces, as explained in the main text.

The length of the thermostated region is 30σ at lower densities and is reduced to 10σ for the more concentrated systems. The number of particles in the simulation box is determined by the desired bulk density and approximately ranges from few tens up to 10^5. Along the x direction the particles are confined by purely reflective walls[3] (blue lines in Fig. 4.1), placed at $x = 0$ and $x = L_x$ in all the simulation runs. On the other hand, thermo-osmosis is a surface-induced phenomenon. Thus, in order to exhibit the diverse phenomenology related to the static and dynamic mechanisms described in Chapter 2, different external potentials will be chosen to confine the fluid in the z direction (these walls are placed at $z = 0$ and $z = h$, as shown by the green lines in Fig. 4.1). The analytical form and the peculiarities of the external potentials studied in this Chapter are introduced in Section 4.2 where the resulting thermo-osmotic flows are also presented.
Regardless of the confinement, each initial configuration is first equilibrated through a NVT dynamics, obtained employing the Bussi-Donadio-Parrinello thermostat for 3×10^7 steps. The time step δt is set equal to 0.005τ throughout all the simulations. The temperature gradient $\partial_x T$ along the x axis is obtained by setting the temperature of the thermostated regions at two different values, T_C and T_H. Under these conditions, a NVE time integration is performed for further 3×10^7 steps, during which the system reaches the stationary state. The results presented in the next Section have been obtained through an average process on the data accumulated by running the simulation for a number of steps ranging from 10^9 to 1.2×10^{11}, depending on the bulk density (more diluted systems need larger amount of data for a better statistics).

[3]Namely a step potential, vanishing in the fluid region and divergent outside.

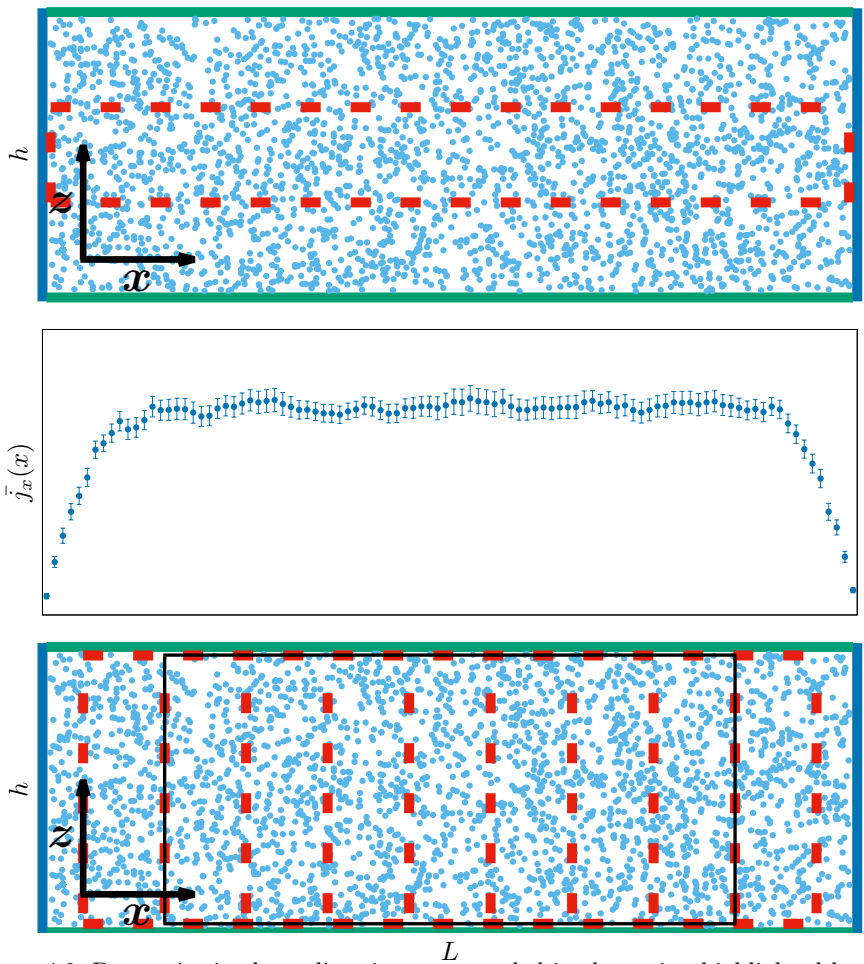

Figure 4.2: Properties in the x direction are sampled in the region highlighted by the red rectangle of the top panel. An example of such a property is given in the central panel, where the mass flow in the x direction is shown. The properties in the z direction are sampled in the red rectangles shown in the lower panel. The resulting z profiles are usually averaged, but only if not affected by the lateral hard walls (that is, referring to the example, if belonging to the black rectangle).

The sampling scheme is presented in Fig. 4.2. The red rectangle in the top panel outlines the region where bulk properties in the x direction are measured with a granularity of 2σ [4]. It is centered in the box, with a length equal to L_x, while its width depends on the value of h and must ensure to sample bulk properties. An example of a sampled property is given in the central panel, where the bulk mass flow $\bar{j^x}(x)$ is shown. Here an important feature of closed channels systems is clear: Lateral reflective walls affect the physical properties within a certain range.
This aspect is important when profiles in the z direction are considered. These are measured in the red rectangles shown in the bottom panel, with a granularity of 0.05σ. In order to improve statistics these profiles are averaged, but only those regions where the bulk properties are not affected by the thermostats (only particles within the black rectangle in the bottom panel) contribute to the average.

4.1.1 Linearity of the temperature profile

As previously explained, the thermal gradient is obtained keeping the two thermostated regions at different temperatures T_C and T_H through a canonical sampling thermostat and performing a NVE time integration. The theoretical approach formulated in Chapter 2, which was a guide for this molecular dynamics survey of thermo-osmosis, assumes a linear response of the system to the perturbation induced by a constant temperature gradient. For this reason the temperatures of the reservoirs were carefully chosen in order to obtain the same linear behavior. Moreover, in accordance with theory, a linear temperature profile induces linear bulk density and pressure profiles in the x direction. This prediction is confirmed by our molecular dynamics simulations, as shown in Fig. 4.3, where data for a typical simulated system are shown. A temperature gradient $\partial_x T \approx 0.0005\epsilon/k_B\sigma^5$ allows to obtain these linear behaviors independently of the bulk densities and of the external confining potentials considered in the present work. Lower values of the thermal gradient satisfy these linearity requirements, but induces weak responses to $\partial_x T$ with consequent problems related to the signal-to-noise ratio. Instead higher values induce a non-linear behavior of these thermodynamics properties in the more rarefied systems: Here, in bulk, $p \approx \rho k_B T$ and a high temperature gradient emphasizes this non-linear relation between T, p and ρ.
The average temperature is defined by the thermostated regions temperatures $T \approx \frac{T_H+T_C}{2}$ and, if not differently specified, it is $T \approx 0.9\epsilon/k_B$. This value is high enough to keep systems far away from the gas-liquid coexistence region[72],

[4]Note that these properties are measured also in the thermostated regions.

[5]Note that if we consider Argon particles then Lennard-Jones parameters acquire the following values: $\sigma = 3.4 \times 10^{-10}$m, $m = 6.69 \times 10^{-26}$kg and $\epsilon = 1.65 \times 10^{-21}$J. Thus in physical units this temperature gradient becomes $\partial_x T \approx 1.6 \times 10^6$K/cm.

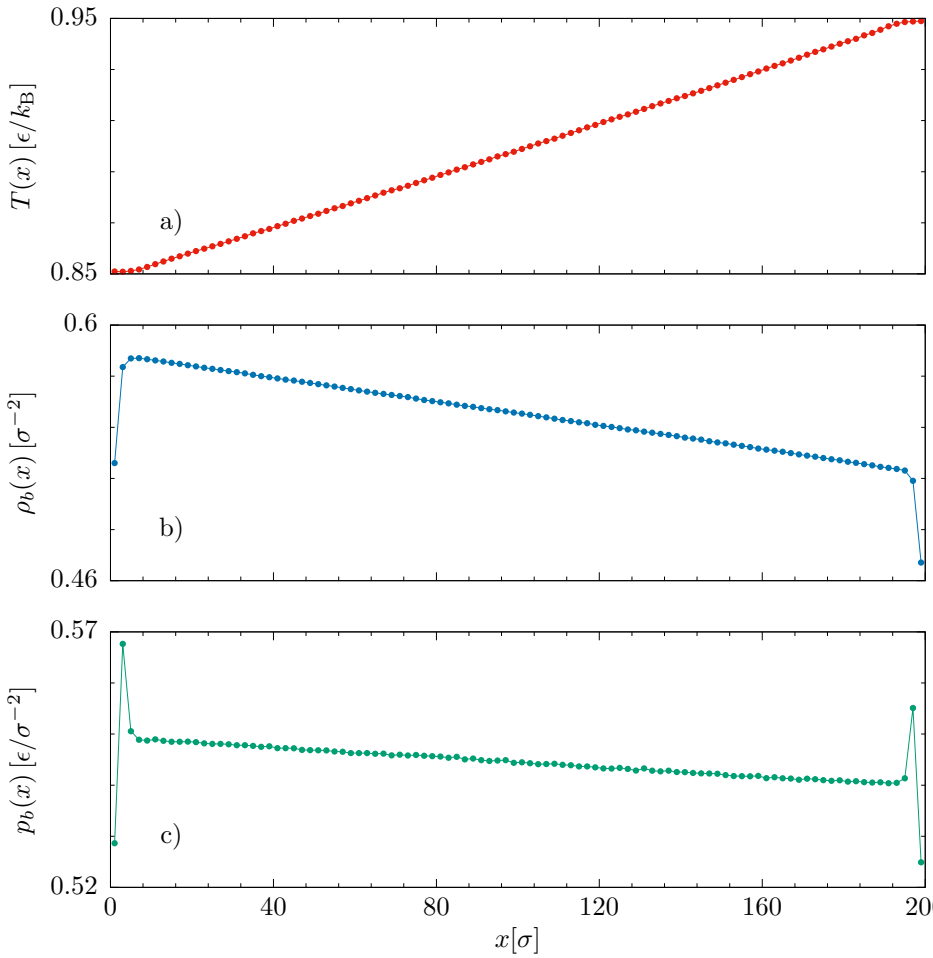

Figure 4.3: Linearity of the temperature (a, red dots), bulk density (b, blue dots) and pressure (c, green dots) profiles in the x direction, for a typical system.

regardless of density and box length L_x. At the same time it is low enough to avoid a damping effect on the external potentials[6], when present.
The most relevant observables which characterize thermo-osmosis in a closed pore are the velocity profile $v_x(z)$ and the bulk pressure gradient $\partial_x p$, which carries the same information of the pressure drop usually measured in experiments. In the following, we will provide results for a temperature gradient equal to $\partial_x T = 0.0005\epsilon/k_B\sigma$. Being in the linear regime, our numerical results can be extrapolated to smaller temperature differences. Moreover, bulk pressure gradients are obtained through linear fitting of profiles such as the one shown

[6]In the Boltzmann factor the external potential is multiplied by $\beta = \frac{1}{k_B T}$.

in panel c of Figure 4.3.

4.2 THE ROLE OF CONFINEMENTS ON THERMODYNAMIC PROPERTIES

In order to express in a clear way the results of this Section, they are divided on the basis of the confining walls. First we will present systems confined by the simplest surfaces, i. e. the purely reflective and diffusive walls. Then the reflective walls plus smooth potentials will be discussed. Finally a more physical confinement, made of Einstein solids, will be considered. The section ends with a discussion about the sign of the thermo-osmotic mass flow with respect to the temperature gradient. Note that, regardless of the particular confinement, all systems in this Section are characterized by a length in the x direction equal to $L_x = 180\sigma + 2R$, being R the length of the reservoir regions previously discussed. Instead, the height of these systems in the z direction is equal to $h = 30\sigma + 2W$, where W is the wall thickness and it is equal to 6σ for Einstein solids, 0 otherwise.

4.2.1 Purely reflective and diffusive walls

The simplest kind of confinement is a purely reflective wall, namely an external step potential, equal to zero in the fluid region and divergent outside. As shown in Chapter 2, in the ideal gas limit[7], i. e. at densities where the interparticle interactions are negligible and the pressure tensor is isotropic, both the static and the dynamic source terms vanish due to the peculiar form of the external potential which conserves both the energy and the x-component of the momentum after the collision of the fluid particles with the wall. For the same reason all the remaining contributions to the mass current vanish in the same limit. Therefore the theoretical approach suggests that a thermo-osmotic flow does not arise at low densities when the fluid is confined by purely reflective walls. We stress that the suppression of the static mechanism in rarefied conditions is due to the purely reflective walls which confine the fluid: Thermo-osmosis can be induced also at low density by including an additional attractive or repulsive tail to the hard wall confining potential, because in this way the static source term is not vanishing and we will later investigate this effect. However, at higher densities, the interaction between particles becomes relevant and in principle both the static source term and the dynamic contributions to the mass current are not vanishing, leading to a detectable effect.

[7]Note that it is mandatory to introduce a finite relaxation time to avoid divergences of the time integrals.

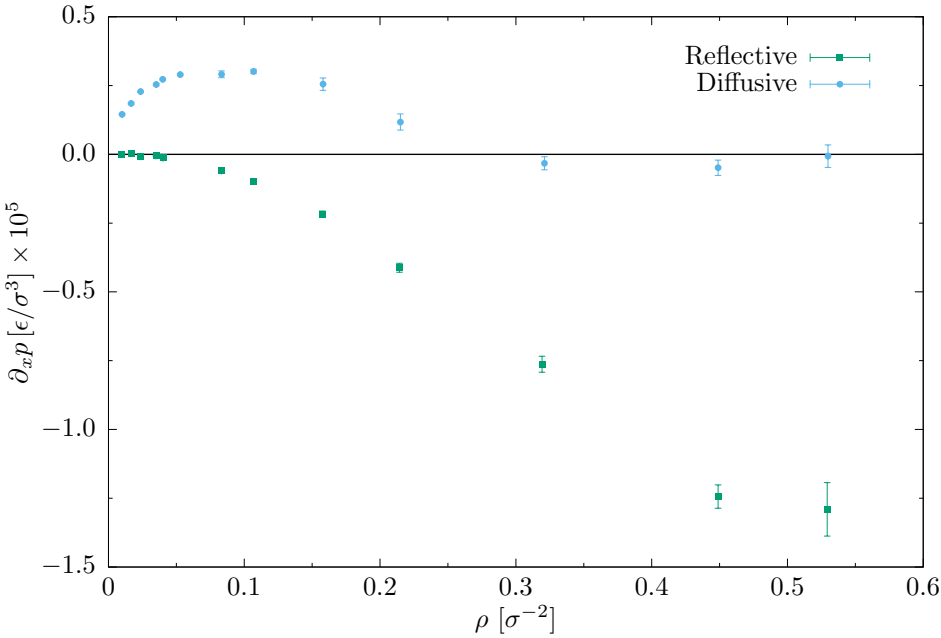

Figure 4.4: Bulk pressure gradient as a function of the bulk density for reflective (green squares) and diffusive (light blue dots) wall.

The data (squares) in Figure 4.4 show the bulk pressure gradient of a Lennard-Jones fluid confined by purely reflective walls as a function of the bulk density. At low densities the mass flux is extremely weak[8] in the bulk region and a significant thermo-osmotic flow only appears when the density is increased above $\rho \approx 0.075\sigma^{-2}$. The bulk pressure gradient is negative for all the values of the density studied: The direction of the thermo-osmotic slip is thus opposite to the temperature gradient[9]. The behavior shown in Figure 4.4 can be interpreted on the basis of the predictions of the linear response approach. The derivatives of the tangential pressure near the surface for a dilute and a dense system confined by a purely reflective wall are shown in Figure 4.5, panel c and d. At the lower density this weak static contribution drives particles near the surface towards the cold side of the system. Qualitatively the same consideration can be made also for the system at the higher density, but the magnitude of $\partial_x p_T(z)$ increases and thus also the bulk pressure gradient modulus. These

[8] In the most dilute systems statistical accuracy does not allow to discriminate the presence of a clear bulk pressure gradient, while from $\rho \approx 0.04\sigma^{-2}$ the mass flux is not totally vanishing: Indeed particles interactions are not completely negligible also at these densities.

[9] The backflow is parallel to the temperature gradient, thus the thermo-osmotic flow must be in the opposite direction.

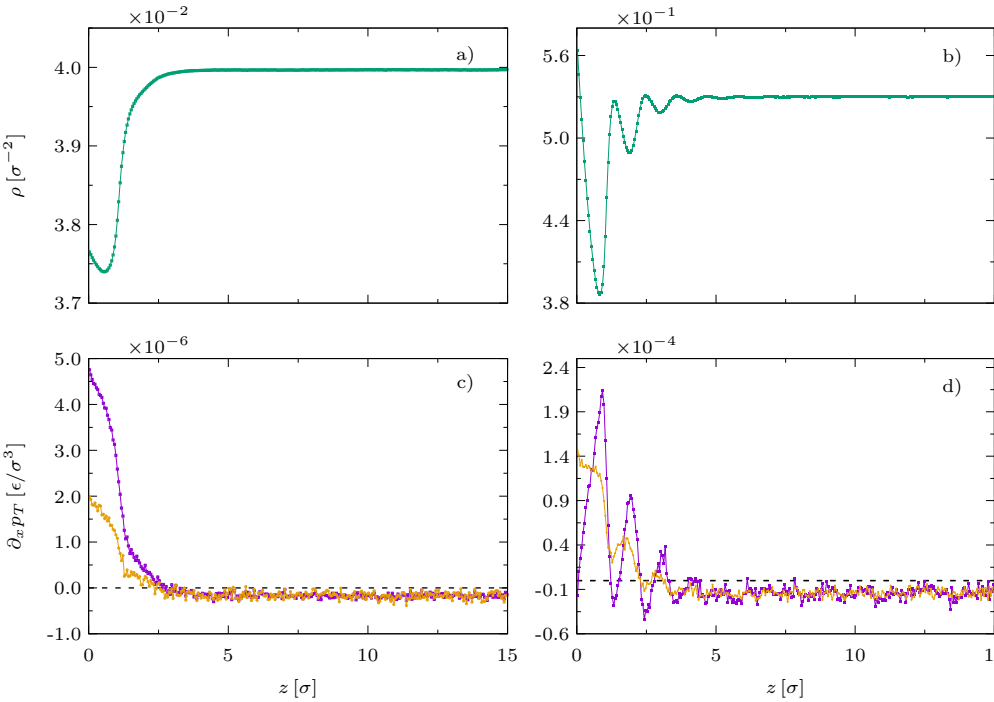

Figure 4.5: Green dots of panel a and b show the density profiles for systems confined by reflective walls, while panel c and d shows the corresponding derivative w.r.t. x of the tangential pressure (orange dots Harasima - violet dots Irving-Kirkwood) for a Lennard-Jones fluid confined by a hard wall at bulk densities $\approx 0.04\sigma^{-2}$ (panel a and c) and $\approx 0.55\sigma^{-2}$ (panel b and d).

data do not allow to make any consideration about the role of the dynamic mechanism, but the static one clearly acquires importance with density and drives particles towards the cold side of the system: This is in accordance with the trend and the sign of the bulk pressure gradient shown in Figure 4.4. Note that the derivative shown in panels c and d of Figure 4.5 are taken directly from the nonequilibrium simulations, differently from the ones shown in the previous Chapter. Moreover, in panels a and b of the Figure are shown also the density profiles and it is interesting to note that a trace of layering effect starts to appear at higher density.

The specular reflection of a particle's velocity after the collision with a smooth, perfectly flat, hard wall guarantees the exact conservation of the particle's momentum, without any exchange between the particle and the wall. However, as suggested by Maxwell[53], real surfaces are characterized by the presence of roughness, which can be modeled by small asperities with different height: These asperities entangle the impinging particles, which, after some collisions

in the cavities, return to the surrounding gas with a different momentum. This behavior can be modeled by the so called diffusively reflecting wall. The diffusive wall confines in a half-space the fluid exactly like a flat hard wall, but absorbs, with a given probability, the impinging particles and afterwards allows them to evaporate with a new momentum selected from the a Maxwell-Boltzmann distribution at the same temperature of the wall[53]. Our implementation of the diffusive wall is slightly different than Maxwell's original idea: The normal component of the impinging particle is specularly reflected after the collision, as in the case of a smooth hard wall, but the tangential component p^x is taken from a Maxwell-Boltzmann distribution at the local temperature $T(x)$ of the wall, defined by

$$T(x) = T_C - \frac{T_C - T_H}{L_x} x, \tag{4.1}$$

where x is the coordinate of the point of impact. The diffusive confining potential, employed for the first time in a molecular dynamics simulation many years ago[78] and recently applied to a nonequilibrium molecular dynamics simulation[82], implies that neither the particle's momentum nor the energy are conserved during the impact. Under these assumptions it can be shown that, according to the linear response approach, a current flow arises also in the dilute limit, because the dynamic source term and the dynamic contributions to the mass current are in general different from zero. In the simpler case of an open channel it is possible to obtain an analytical expression for the thermo-osmotic velocity, expressed in Equation 2.135, at very low densities, showing that the flow is parallel to the temperature gradient. The data (circles) in Figure 4.4 confirm these expectations, being $\partial_x p$ a positive quantity in rarefied systems. But, quite surprisingly, the bulk pressure gradient is not a monotonic function of the bulk density: After a linear increase at very low densities, the pressure gradient reaches a plateau at $\rho_b \approx 0.05\sigma^{-2}$ and, after a decrease it becomes negligible for densities larger than $0.3\sigma^{-2}$. This behavior is compatible with the understanding of the phenomenon provided by microscopic approach introduced above: While the dynamic mechanism is now important also in rarefied fluids, due to the particular particle-surface interaction, the static one is extremely weak at low densities also when the fluid is confined by a diffusive wall[10] and gains importance in dense systems. Moreover, as shown by data related to the purely reflective walls, the static mechanism drives particles towards the cold side of the system. Thus the dynamic and static mechanisms start to balance gradually out, as confirmed by the behavior of the bulk pressure gradient at high densities: When the system is confined by the diffusive wall particles in the rarefied regime are driven by the dynamic

[10]Because the pressure tensor is isotropic for an ideal gas. Moreover, even if also the static statistical properties in these two systems could in principle differs, the density profiles numerically computed are equivalent within uncertainty, suggesting that the static properties can be considered equivalent.

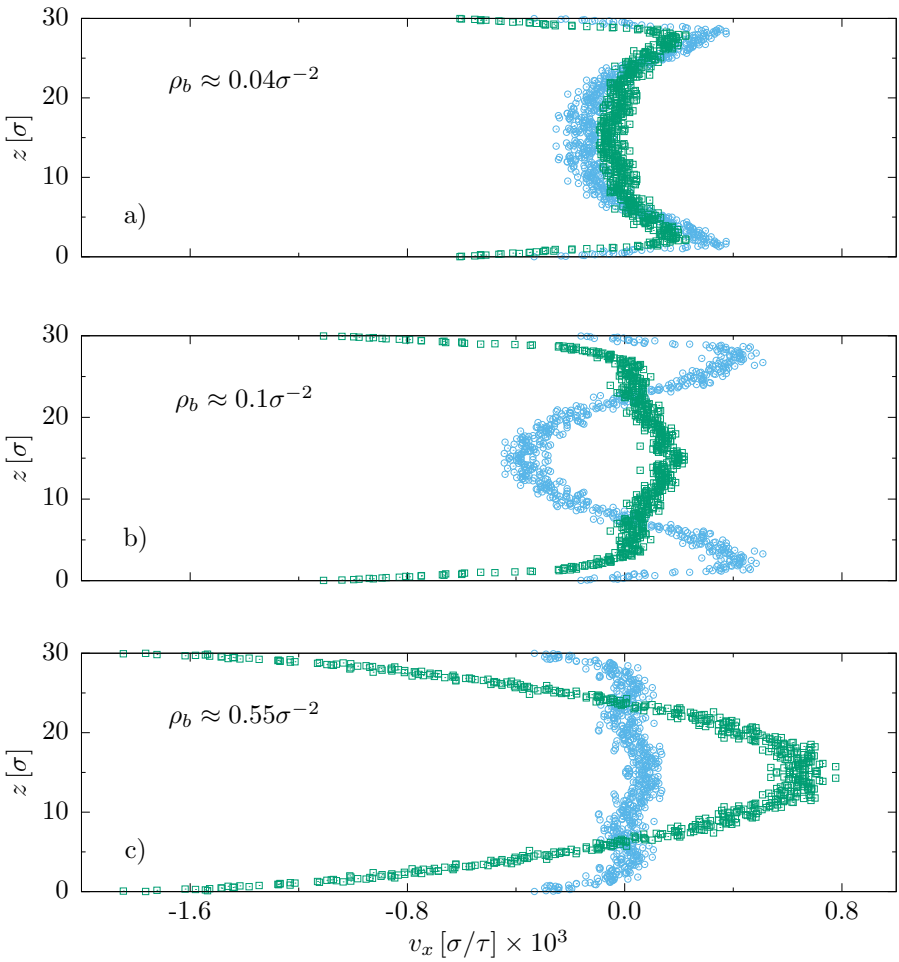

Figure 4.6: Velocity profile of the fluid along the nanochannel at different values of the bulk density. Green squares and light blue circles refer to reflective and diffusive confinements respectively.

mechanism through the hot side and a bulk pressure gradient develops, while increasing the density $\partial_x p$ tends to vanish because the dynamic mechanism is still relevant, also for this concentrated systems, but it is opposite to the static one. As interestring consequence of this result we can state that the approximations introduced in Chapter 2 for the dense regime, which lead to Derjaguin's result, are not always justified.

More insights about this picture can be obtained by looking at the velocity

profiles, shown in Figure 4.6[11]. Let us consider systems confined by reflective walls. In regime I (panel a) both dynamic and static mechanisms are feeble, but comparable: The velocity profile is negative near the confinements, but further it becomes positive. In regime II (panel b) the static source term acquires more importance and it completely dominates in regime III (panel c). The diffusive wall strongly enhances the dynamic mechanisms which pushes particles towards the hot side, to the extent that in the densest system the flow is extremely weakened. Furthermore in Chapter 2 we showed that the slip velocity for a three dimensional ideal gas in an open channel reads

$$v_\infty = \frac{3}{4}\frac{\eta}{\rho}\frac{\partial_x T}{T} \tag{4.2}$$

where $\eta = p\tau_c$, and it is possible to show that this result holds also for two-dimensional ideal gas, where the mean collision time τ_c can be expressed as

$$\begin{aligned} \tau_c &= \frac{m}{2\sigma\rho v_b} \\ &= \frac{\sqrt{\beta m^3}}{2\sqrt{2}\sigma\rho}, \end{aligned} \tag{4.3}$$

being v_b the ballistic velocity, leading to

$$v_\infty = \frac{3}{8\sqrt{2}}\sqrt{\frac{m}{\beta}}\frac{1}{\rho\sigma}\frac{\partial_x T}{T}. \tag{4.4}$$

If we now consider the conditions of the system reported in panel a of Figure 4.6, i. e. $\rho \approx 0.04\sigma^{-2}$, $T \approx 0.9\epsilon/k_\mathrm{B}$ and $\partial_x T = 0.0005\epsilon/k_\mathrm{B}\sigma$, the resulting slip velocity is $v_\infty \approx 3.5 \times 10^{-3}\sigma/\tau$. This result cannot be directly compared with any of the velocity values in the profile related to the diffusive wall of panel a of Figure 4.6, because of the different geometries and boundary conditions involved: In the closed channel a back flow takes place and the velocity profile is not characterized by no slip boundary conditions. Nevertheless, v_∞ is about one order of magnitude greater than the velocity positive peak in profile a of Figure 4.6, which is a reasonable result[12].

4.2.2 Reflective walls plus potentials

If an external potential is present, thermo-osmosis in rarefied systems can arise also due to the static source term. In the ideal gas limit the pressure

[11] It is important to note that here and in the following no-slip boundary conditions are not imposed. This is due to the fact that walls do not exert a force on the fluid particles in the x direction.

[12] Note that this gap is reduced if we considered the difference Δv between the velocity positive peak and the velocity at $z = 0$, in fact $\Delta v \approx 10^{-3}\sigma/\tau$.

tensor is isotropic everywhere, so both its normal and tangential components are defined by the hydrostatic equilibrium condition, which, in presence of a temperature gradient aligned to the tangential direction, can be written as

$$\partial_z p(z,x) = -\frac{\rho(z,x)}{m}\partial_z V(z), \tag{4.5}$$

where the local thermal equilibrium condition has been employed. Here $p(z,x)$ is the isotropic pressure and $V(z)$ is an external potential, constant along the tangential direction. If $V(z)$ vanishes in bulk, the pressure profile reads

$$p(z,x) = p(x)\mathrm{e}^{-\beta(x)V(z)}. \tag{4.6}$$

Thus the derivative of the tangential pressure can be expressed as

$$\partial_x p(z) = \Big[\partial_x p - pV(z)\partial_x\beta\Big]\mathrm{e}^{-\beta V(z)}, \tag{4.7}$$

being p and β the average bulk pressure and the inverse of the thermal energy of the system. Equation 4.7 shows that the static source term can arise also in ideal gases if an external potential $V(z)$ is present[13]. As a consequence, thermo-osmosis in diluted systems does not necessarily require the activation of the dynamic mechanism.
This condition can be numerically investigated confining fluid particles with reflective walls and a smooth external potential: Particle energy and momentum parallel to the surface are conserved during the collision against the wall, thus the dynamic source term does not arise, while $V(z)$ provides the static one according to Equation 4.7. Two kinds of external potentials are added to the purely reflective wall: A repulsive one (already introduced in Chapter 3)

$$V_r(z) = \begin{cases} k(z-z_r)^2 & 0 < z \leq z_r \\ 0 & z > z_r, \end{cases} \tag{4.8}$$

where $k = 0.1\epsilon/\sigma^2$ and $z_r = 5\sigma$, and a Lennard-Jones 9-3 one

$$V_a(z) = \begin{cases} \epsilon_{93}\left[\frac{2}{15}\left(\frac{\sigma_{93}}{z}\right)^9 - \left(\frac{\sigma_{93}}{z}\right)^3\right] & 0 < z \leq z_a \\ 0 & z > z_a, \end{cases} \tag{4.9}$$

where $\epsilon_{93} = 1\epsilon$, $\sigma_{93} = 1\sigma$ and $z_a = 10\sigma$. This potential is attractive everywhere, but for $z < \left(\frac{2}{5}\right)^{\frac{1}{6}}\sigma$ where it becomes highly repulsive. The same potentials confine the fluid near the upper wall at $z = 30\sigma$. Nonequilibrium simulations allow to directly compute $\partial_x p_T(z)$ and in rarefied systems there is a good agreement between simulation data and equation 4.7, as shown in figure 4.7

[13]Note that if an open channel is considered than $\partial_x p = 0$, and the sign of $\partial_x p(z)$ is fully determined by $V(z)$.

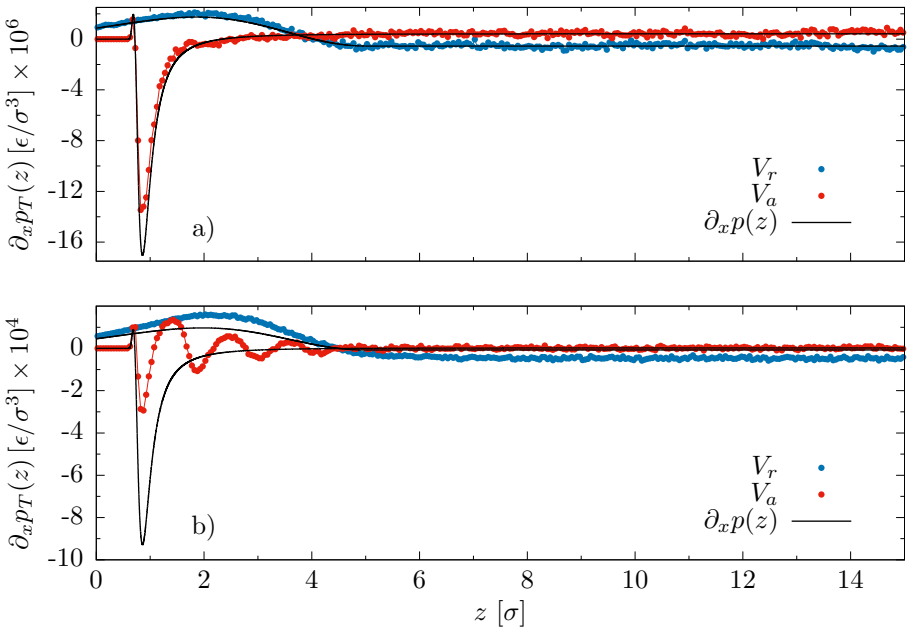

Figure 4.7: Pressure profiles derivatives for system confined by reflective walls plus potential. Black lines refer to the ideal gas estimation, while blu data and red data are simulation results (where $V_r(z)$ and $V_a(z)$ are respectively employed). Panel a refers to rarefied fluids ($\rho_b \approx 0.01$) while panel b to the dense ones ($\rho_b \approx 0.5$).

panel a. This means that at these densities the ideal gas approximation holds rather well and thus $\partial_x p(z)$ is really the only force responsible for thermo-osmosis. The agreement is lost if denser systems are considered, as shown in figure 4.7 panel b, where strong deviations from the ideal solution take place. Nonetheless, in presence of the repulsive external potential, the ideal and real behaviors are qualitatively similar, probably because of the low density near the surface induced by $V_r(z)$. Instead, the Lennard-Jones 9/3 potential gives rise to particles layering and a complex tangential pressure derivative profile arises, completely different to the ideal gas solution.

In these dense systems not only the pressure tensor is anisotropic, but the deviation from ideality implies also that dynamic mechanisms can possibly contribute to thermo-osmosis. Therefore, there is not a simple relation between the external potential and the thermo-osmotic flow direction. This information can be easily obtained through the bulk pressure gradients, presented in figure 4.8. The sign of the overall thermo-osmotic flow results to be independent of bulk density: It is against the thermal gradient for the repulsive potential $V_r(z)$, while it is parallel to it if $V(z) = V_a(z)$. The magnitude of the effect is instead strongly dependent on the bulk density. In diluted systems the value of $|\partial_x p|$ for the two potential is similar and increases approximately linearly with

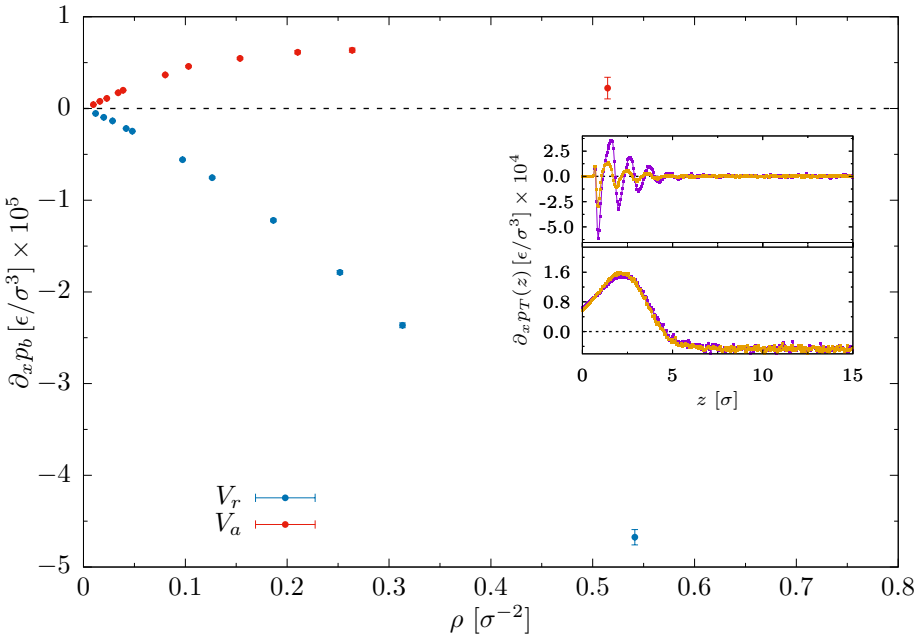

Figure 4.8: Bulk pressure gradients for systems at different densities confined by the attractive potential (red data) and the repulsive potential (blu data). Inset: $\partial_x p_T(z)$ computed with the Harasima (orange) and Irving-Kirkwood (violet) pressure tensors for the L-J potential (top panel) and the repulsive one (bottom panel).

ρ. Repulsive potentials lead it to grow also at the higher densities, while its trend is no longer monotonic in presence of the attractive one: This behavior is probably due to the complex shape of $\partial_x p_T(z)$ shown in figure 4.7 panel b. Even if the absolute value of the bulk pressure gradient is very similar for rarefied systems, the shape of the velocity profiles does not share the same property, as shown in figure 4.9, panel a. In both cases the velocity field develops within the scale of the potential, as expected[14], and it becomes essentially flat in the center of the system (actually, it is an extremely wide parabola). Most significant differences arise near the confining surfaces: Attractive potentials induce, as shown in the inset of figure 4.9, panel a, a negative peak velocity in the proximity of the surface, where $V_a(z)$ is positive. This peak essentially does not contribute to the mass flow, being there the density very low: The Lennard-Jones potential is highly repulsive near the surface, thus fluid particles rarely occupy this region. Indeed, for $z < \left(\frac{2}{5}\right)^{\frac{1}{6}} \sigma$, $V_a(z)$ becomes rapidly repulsive and at a given value of z particles do not occupy these region at all, as shown

[14]Indeed at these densities and with these kind of confinements only the static source term arises.

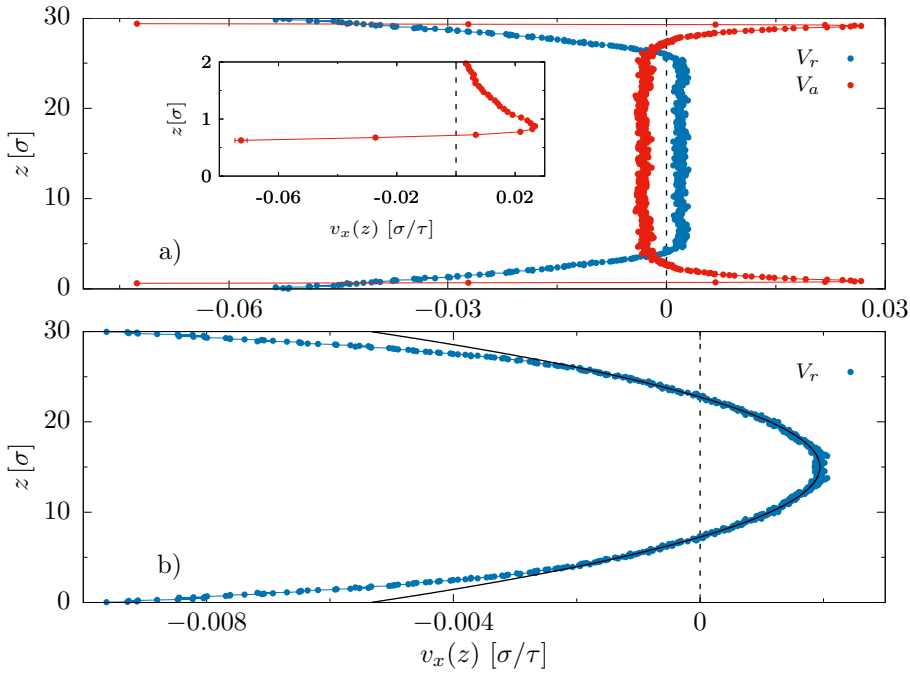

Figure 4.9: Velocity profiles in presence of the repulsive potential (blue data) and the Lennard-Jones one (red data). a) Diluted systems ($\rho_b \approx 0.01$). b) Dense system ($\rho_b \approx 0.5$). The inset in figure a shows a detail of the velocity profile near the confining surface supplemented the Lennard-Jones potential.

in the inset of panel a, Figure 4.9: The velocity field does not arise in the proximity of the confining surface, where there are no particles. Moreover it is interesting to note that at $z \approx \left(\frac{2}{5}\right)^{\frac{1}{6}} \sigma \approx 0.86\sigma$ there is a peak in the velocity profile. This suggests that thermo-osmosis is driven by the attractive force when $z > \left(\frac{2}{5}\right)^{\frac{1}{6}} \sigma$ and by the repulsive one for $z < \left(\frac{2}{5}\right)^{\frac{1}{6}} \sigma$: Thermo-osmosis seems to be a local phenomenon.

At higher densities it is difficult to compute the velocity profile for systems confined by the Lennard-Jones potential, because, interestingly, the velocity becomes extremely low. Also with the repulsive potential the fluid velocity decreases at higher density, as shown in figure 4.9, panel b, but accurate results can still be obtained. In this case, far from the walls the back flow velocity is clearly parabolic, in agreement with Poiseuille law. The deviation from the parabolic behavior takes place at about 5σ from the confining surfaces and this value is comparable with the range of $\partial_x p_T(z)$[15], suggesting that the thermo-osmotic flow in this dense system is originated by the static mechanism.

[15]We recall that $z_r = 5\sigma$.

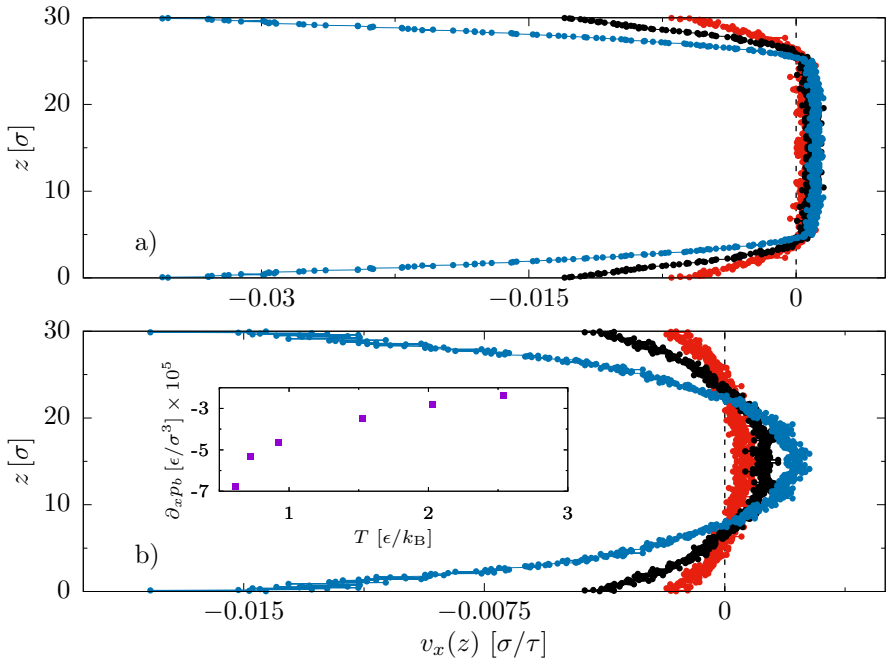

Figure 4.10: Velocity profiles for different values of the average temperature: Blue data, $T = 0.7\epsilon/k_B$; black data, $T = 01.5\epsilon/k_B$; red data, $T = 2.5\epsilon/k_B$ a) Diluted systems ($\rho_b \approx 0.03$). b) Dense system ($\rho_b \approx 0.55$). The inset in figure b shows the trend of the bulk pressure gradient with temperature for the denser system.

The effect of the average temperature

Let us now study the effect of the average temperature of the system on the velocity profiles. In Figure 4.10 panel a, diluted systems confined by the repulsive potential are considered for different average temperatures of the fluids. It is clear that an increase of the temperature leads to a weaker thermo-osmotic flow. A simple interpretation to this observation is that the inverse of the temperature, β, enters in the Boltzmann factor multiplying the external potential contribution, $V(z)$. Thus, we expect that the higher is the temperature, the lower is the effect of the external potential peculiarities on the fluid properties: $V(z)$ tends to behave like a reflective wall. The data presented previously show that the repulsive potential strongly enhances the thermo-osmotic flow, thus it is reasonable that the mass flux decreases with temperature. This scenario is confirmed also by data presented in the panel b of Figure 4.10, where the velocity profiles for dense systems, confined by the repulsive potential and kept at different average temperatures, are shown, but also from the inset, where the bulk pressure gradient as a function of the temperature is shown.

The most interesting consequence of these observations is that if a given potential induces a thermo-osmotic flow towards the hot side of the system (as

	$\epsilon_{93} = 1\epsilon$	$\epsilon_{93} = 0.6\epsilon$	Reflective Wall
$T\,[\epsilon/k_{\mathrm{B}}]$	$\partial_x p \times 10^6\,[\epsilon/\sigma^3]$	$\partial_x p \times 10^6\,[\epsilon/\sigma^3]$	$\partial_x p \times 10^6\,[\epsilon/\sigma^3]$
0.9	2.44 ± 0.20	-3.97 ± 0.49	-12.44 ± 0.42
2.5	1.19 ± 0.18	-0.71 ± 0.28	-1.27 ± 0.52

Table 4.1: Dependence on the average temperature T of the bulk pressure gradient for systems at $\rho \approx 0.45\sigma^{-2}$ and confined by reflective walls plus the potential $V_a(z)$ and purely reflective walls. Different values of the wall-particles interaction parameter ϵ_{wf} are taken into account: $\epsilon_{wf} = 1\epsilon$ and 0.6ϵ.

$V_a(z)$, for example), then a change of the mass flow direction is expected above a certain average temperature of the fluid. In order to verify this condition we performed a set of simulations of systems confined by the Lennard-Jones 9-3 potential and at a bulk density $\rho \approx 0.45\sigma^{-2}$. We considered two different average temperatures, $T \approx 0.9\epsilon/k_{\mathrm{B}}$ and $2.5\epsilon/k_{\mathrm{B}}$, and wall-fluid interaction parameters, $\epsilon_{93} = 1\epsilon$ and 0.6ϵ. The main results are reported in Table 4.1. When the potential is strongly attractive ($\epsilon_{93} = 1\epsilon$) the bulk pressure gradient is positive for the two value of T considered, even in if it decreases with a temperature increase. If the interaction parameter is decreased at $\epsilon_{93} = 0.6\epsilon$ the product $\beta\epsilon_{93}$ decreases as well, but also in this case there is not an inversion of the bulk pressure gradient sign in the considered temperature gap: The modulus of $\partial_x p$ still decreases with T, but now it results to be negative for both the considered average temperatures. This proves that, when attractive external potentials are involved, the product $\beta\epsilon_{93}$ plays an important role in the definition of the direction of the thermo-osmotic mass flow with respect to the temperature gradient. Probably the inversion of sign in this temperature gap can be observed for value of ϵ_{93} included between the two considered here. Moreover, data reported above confirm that reflective walls plus potential tend to behave like a purely reflective wall when the product $\beta V(z)$ is decreased, thus it is interesting to evaluate the effect of T on a system directly confined by this kind of wall. At this scope we simulated a system with a bulk density $\rho \approx 0.45\sigma^{-2}$ and $T = 2.5\epsilon/k_{\mathrm{B}}$ and the resulting bulk pressure gradient is reported in Table 4.1. Comparing this result with the value of $\partial_x p$ at $T \approx 0.9\epsilon/k_{\mathrm{B}}$ it is clear that the hotter is the system the weaker is the thermo-osmotic mass flow when fluids are confined by purely reflective walls. Thus the suggestion is that an increase of the average temperature generally leads to a weaker thermo-osmotic flow.

4.2.3 Physical surfaces

In real systems confining surfaces are made of particles, which interact and exchange momentum and energy with the fluid: Both dynamic and static mechanisms are activated, also at low density. In order to keep systems as simple

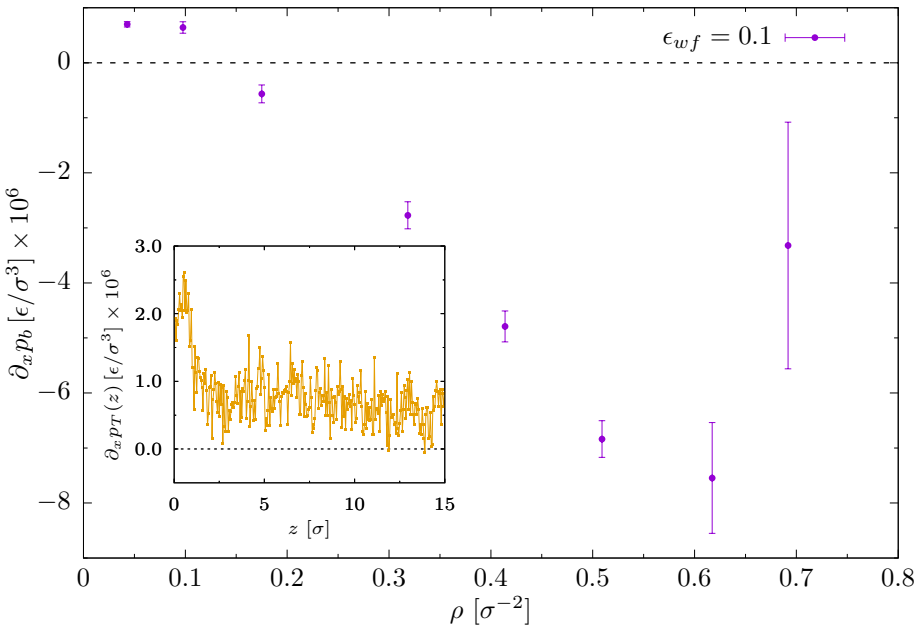

Figure 4.11: Purple dots show the bulk pressure gradients for systems at different bulk densities confined by Einstein walls with $\epsilon_{wf} = 0.1\epsilon$. Inset: Harasima tangential pressure derivative for the more dilute system.

as possible, we decided to investigate the effect of particle-wall interactions by the simplest model of a real confining surface: An Einstein wall, where particles are organized in a simple square lattice with density $0.9\sigma^{-2}$ and bound to their position by a harmonic potential with $k = 5000\epsilon/\sigma^2$. They interact with the fluid particles through the usual truncated ($r_c = 4.5\sigma$) and shifted 12-6 Lennard-Jones potential and the interaction parameters are $\epsilon_{wf} = 0.1\epsilon$ and $\sigma_{wf} = 1\sigma$. The sign of the overall thermo-osmotic mass flow can be deduced by figure 4.11, where bulk pressure gradients for systems at different bulk densities are reported. In the more rarefied systems the thermo-osmotic flow is aligned to the temperature gradient, while the derivative of the tangential pressure near the surface is positive, as shown for the more dilute system in the inset of Figure 4.11. This means that here the predominant mechanism is the dynamic one, and it promotes motion towards the hot side of the system. At higher densities, where the static mechanism gains importance, the overall flow becomes opposite to the thermal gradient.
Moreover, the trend of $|\partial_x p_b|$ with bulk density is not monotonic. This inversion of trend is characterized by a significant change in the shape of the tangential pressure derivative, shown in figure 4.12: The strong oscillations at the higher densities weakens the net effect of pressure on the flow, as shown also in the inset of the same figure: The velocity profile at the highest density essentially

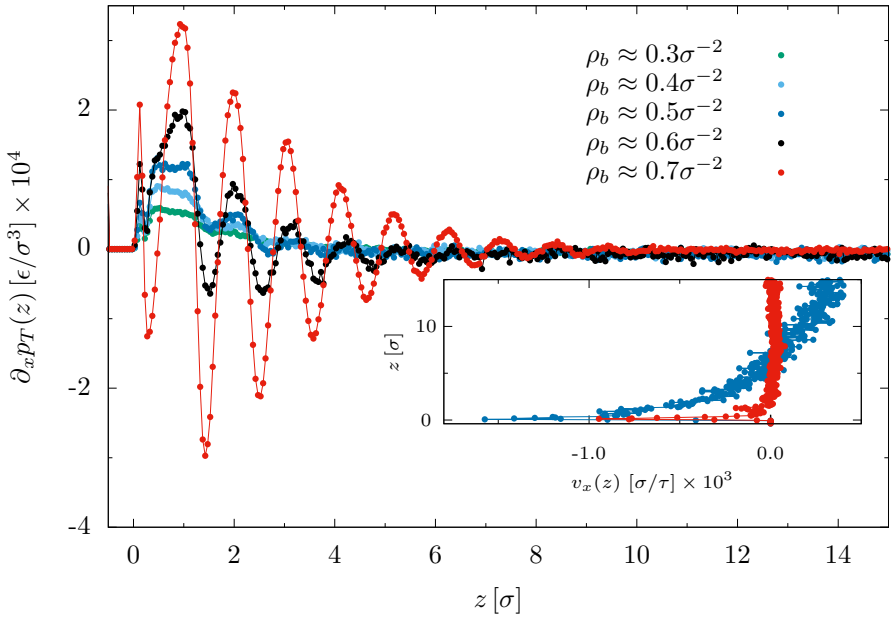

Figure 4.12: Harasima tangential pressure gradients for systems at different bulk densities, confined by particle walls. Inset: Velocity profiles for systems at $\rho_b \approx 0.5$ (blue data) and $\rho_b \approx 0.7$ (red data).

vanishes far from the surface, while a stronger effect is present in the system at $\rho \approx 0.5\sigma^{-2}$. The oscillations of $\partial_x p_T(z)$ are promoted by particles layering near the surface and this condition is enhanced by both attractive potentials and high densities. Indeed, they take place also in the highest bulk density considered for systems confined by reflective wall plus the 9-3 Lennard-Jones potential, but not in the systems confined by the purely repulsive interaction $V_r(z)$, as shown in the inset of Figure 4.8[16].
The important effect that these oscillations have on the contribution to the static source term expressed by the integral over z of $\partial_x p_T(z)$ can be observed in Figure 4.13. Data reported here are taken from the equilibrium simulations presented in Chapter 3 and refer to the Harasima pressure tensor. In panel a results related to systems in the same conditions of the ones presented in Figure 4.12 are presented, while in panel b a comparison between the integrals obtained in systems at $\rho \approx 0.7\sigma^{-2}$ and confined by Einstein walls

[16]Note also that in the system confined by the repulsive potential the results obtained with the IK (violet data) and the Ha (orange data) contours are very similar. This is due to the fact that near the surface, were the two pressure tensors should be different, the fluid density is very low. Instead, the Lennard-Jones potential induces a strong layering effect near the surface, thus the resulting IK and Ha tangential derivative are strongly different.

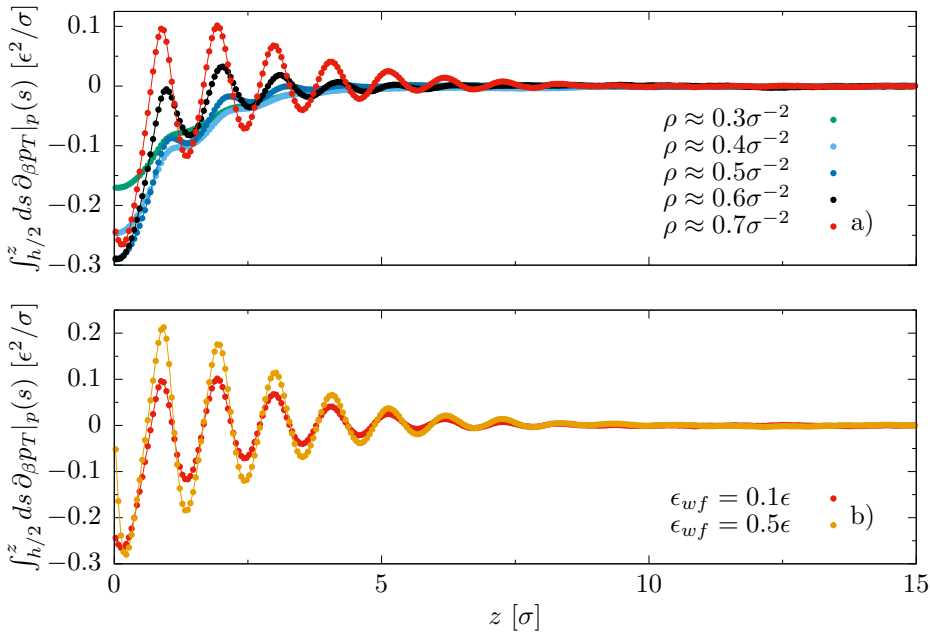

Figure 4.13: Contribution to the static source term given by the Harasima tangential pressure derivative for equilibrium systems confined by Einstein walls. In panel a different densities are considered and the solid-fluid interaction parameter is $\epsilon_{wf} = 0.1\epsilon$. In panel b the density is $\rho \approx 07\sigma^{-2}$ and two interaction parameters are considered, $\epsilon_{wf} = 0.1\epsilon$ and $\epsilon_{wf} = 0.5\epsilon$.

with $\epsilon_{wf} = 0.1\epsilon$ and $\epsilon_{wf} = 0.5\epsilon$ is shown. As shown in Chapter 3, probably, the full static source term, i. e. including the further contribution previously discussed, results to be smoother, but however profiles shown in panel a of Figure 4.13 suggest that the overall effect of the static contribution to the thermo-osmotic mechanism is weakened by particle layering. Panel b shows that this weakening is stronger with the more attractive wall, being the layering more effective.

4.2.4 Some considerations about the sign of the mass flow

A quantitative comparison of the phenomenon arising with the different confining surfaces considered here is not particularly informative, because much depends on the details of the walls. Despite this, some interesting considerations about the sign of the thermo-osmotic flow can be made. Considering the results of the Einstein wall and the diffusive one, the dynamic mechanism drives flux towards the hot side of the system, a result in agreement with the ideal gas limit. Instead, the effect of external potentials seems to be strongly related to the mass excess close to the surface, a quantity known as mass adsorbtion and

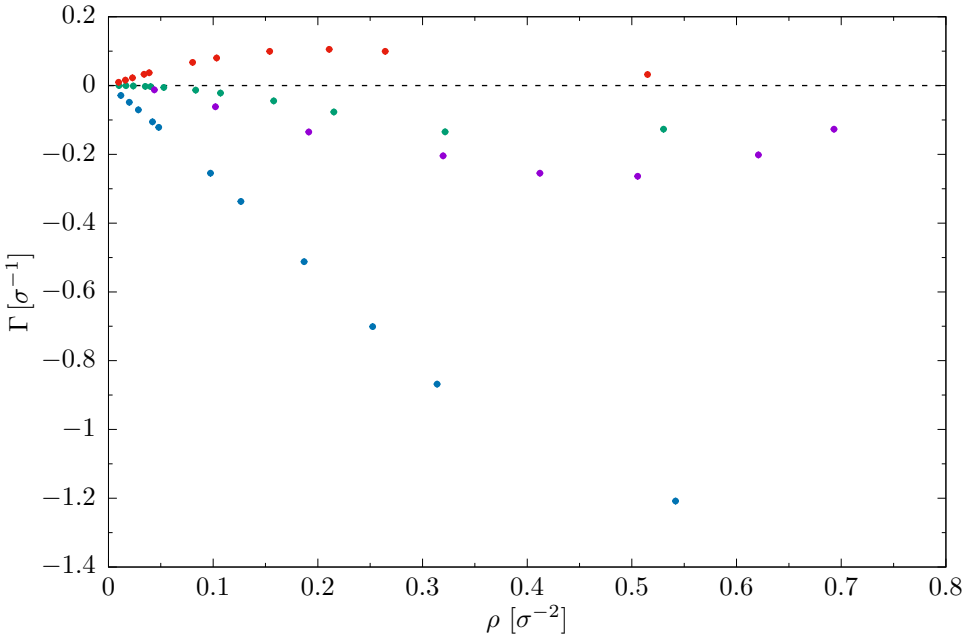

Figure 4.14: Mass excess at different bulk densities and confinements. Green dots refer to reflective walls confinement, purple ones to the Einstein wall surface and the red and blue ones to systems confined by $V_z()$ and $V_r(z)$ respectively.

defined as (see for example Ref. [24])

$$\Gamma = \int_0^{\frac{h}{2}} dz \Big[\rho(z) - \rho\Big], \tag{4.10}$$

where the density profile $\rho(z)$ is evaluated at $x = L_x/2$. Figure 4.14 highlights a strong correlation, both in sign and modulus, between the mass adsorbtion and the bulk pressure gradient shown in Figures 4.4, 4.8 and 4.11 for different confining surfaces. This numerical evidence suggests a simple rule of thumb: Particles accumulation near the surface lead to a thermo-osmotic flow aligned to the temperature gradient, while it is reversed if depletion takes place. Moreover, as previously discussed, particle layering weakens the effect. As a consequence, repulsive potentials enhance a mass flux against the temperature gradient, while attractive potentials favor a particle current towards the hot side.
In order to better investigate this suggestion we decided to consider a "trap" potential $V_t(z)$, which is defined as a combination of the previously introduced ones:

$$V_t(z) = V_a(z) + V_r(z), \tag{4.11}$$

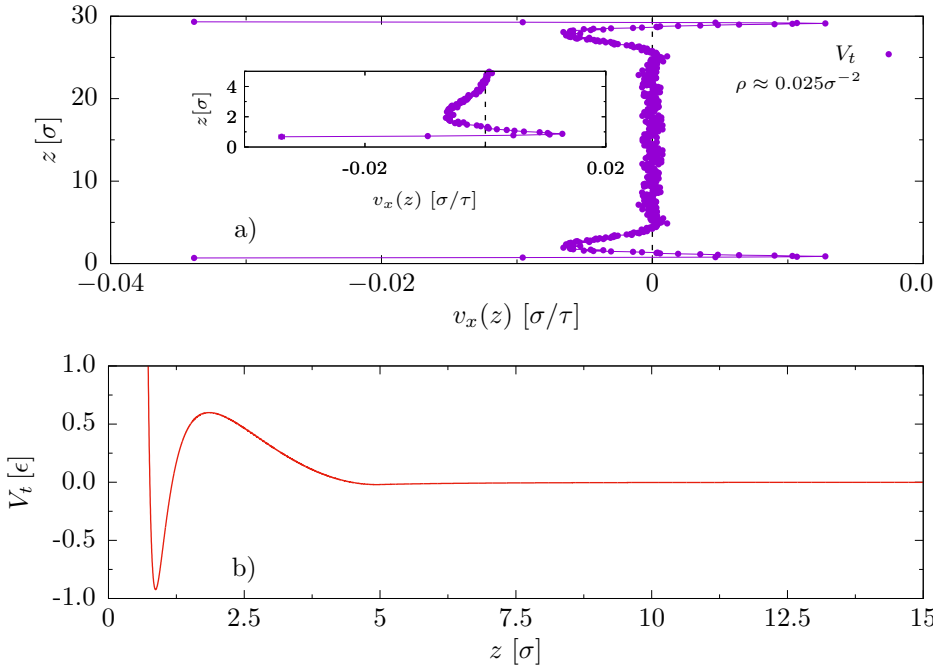

Figure 4.15: a) velocity profile obtained in a rarefied system confined by the trap potential shown in panel b. The inset shows a detail of the velocity profile in the proximity of the wall.

where here $k = 0.1\epsilon/\sigma^2$, $\epsilon_{93} = 2.5\epsilon$, $\sigma_{93} = 1\sigma$, $z_r = 5\sigma$ and $z_a = 10\sigma$. The form of this potential is shown in Figure 4.15, panel b. We simulated a rarefied fluid ($\rho \approx 0.025\sigma^{-2}$) confined by $V_t(z)$. Due to the low density of this gas and the nature of this confinement, dynamic effects are not expected to be relevant, and the resulting velocity profile, shown in Figure 4.15, is mainly due to the static contribution induced by the trap potential. The shape of the velocity field is very similar to the one of $V_t(z)$, but what is more interesting is the relation between mass excess and bulk pressure gradient: In this system the mass excess and the bulk pressure gradient are respectively $\Gamma \approx -3.61 \times 10^{-2}\sigma^{-1}$ and $\partial_x p \approx -1.55 \pm 0.7 \times 10^{-7}\epsilon\sigma^{-3}$, while in the systems with a similar density but confined by reflective walls plus the Lennard-Jones 9-3 potential and the repulsive potential the corresponding results are respectively $\Gamma^a \approx 2.34 \times 10^{-2}\sigma^{-1}$, $\partial_x p^a \approx 1.10 \pm 0.02 \times 10^{-6}\epsilon\sigma^{-3}$ and $\Gamma^r \approx -7.06 \times 10^{-2}\sigma^{-1}$, $\partial_x p^r \approx -1.35 \pm 0.02 \times 10^{-6}\epsilon\sigma^{-3}$, instead, when a purely reflective wall is considered both the source terms are negligible at these densities, and $\Gamma^{rw} \approx -1.1 \times 10^{-3}\sigma^{-1}$, $\partial_x p^{rw} \approx -9 \pm 2 \times 10^{-8}\epsilon\sigma^{-3}$. Therefore, also this simulation performed with the trap potential suggests the important role of the mass adsorption in the definition of the sign of thermo-osmotic mass flow with respect to the temperature gradient direction when the static source term prevails: A surface that induces a particle depletion leads to a

flow towards the cold side, while particle accumulation promotes a mass flux in the opposite direction.

4.3 ASYMPTOTIC BEHAVIOR IN CLOSED CHANNELS

In the last Section of Chapter 2 the theory of thermo-osmosis in a closed channel has been developed and analytical expressions, valid in large systems ($h \gg \sigma$), for the fluid velocity in the middle of the channel

$$v(z)|_{z=\frac{h}{2}} = \frac{\omega}{\rho h} - \frac{\partial_x p}{24\beta^2\eta}h^2 \tag{4.12}$$

and the bulk pressure gradient

$$\partial_x p_b = \rho\frac{\gamma(h) - \gamma_{oc}}{\beta^2}\partial_x\beta \tag{4.13}$$

have been derived. Being ω a constant, independent of h, equation 4.12 suggests that $\partial_x p_b \sim h^{-n}$, with $n \geq 2$, because otherwise $v(z)|_{z=\frac{h}{2}}$ would diverge when $h \to \infty$. On general grounds, no further analytical considerations can be made with respect to $\partial_x p$ or $v(z)|_{z=\frac{h}{2}}$: It is not possible to derive the dependence of γ on h from the equations. Nevertheless, knowing the scaling behavior of $\partial_x p_b$ with h is important, because of the relevance of this quantity in experimental measures. Also the bulk velocity $v(z)|_{z=\frac{h}{2}}$ can be a useful parameter in the implementation of hydrodynamic computations of thermo-osmotic flows in large and complex systems. Thus it is interesting to employ molecular dynamics simulations in order to get some more insights about these quantities and their asymptotic behavior with h.

4.3.1 Scaling law of the bulk pressure gradient with the height of the channel

All the systems are characterized by the same bulk density $\rho_b \approx 0.55\sigma^{-2}$ and confinements, i.e. reflective walls at $x = 0$ and $x = L_x$ and reflective walls plus the repulsive potential $V_r(z)$ at $z = 0$ and $z = h$, but differ for the heights h, ranging from $h = 30\sigma$ up to $h = 700\sigma$. In the first set of simulations the length of channels is $L_x = 200\sigma$ for each value of h and the behavior of the bulk pressure gradient $\partial_x p$ with the system height is obtained, as shown in figure 4.16. The black line results from the fit of the data relative to the systems with largest values of h with the curve $f(h) = \frac{a}{h^2}$, where $a = 0.3429 \pm 0.0054\epsilon/\sigma$. This fit is characterized by a p-value of the χ^2 distribution equal to 0.9708, and this suggests that the bulk pressure gradient asymptotically behaves as

$$\partial_x p \sim h^{-2}\,, \tag{4.14}$$

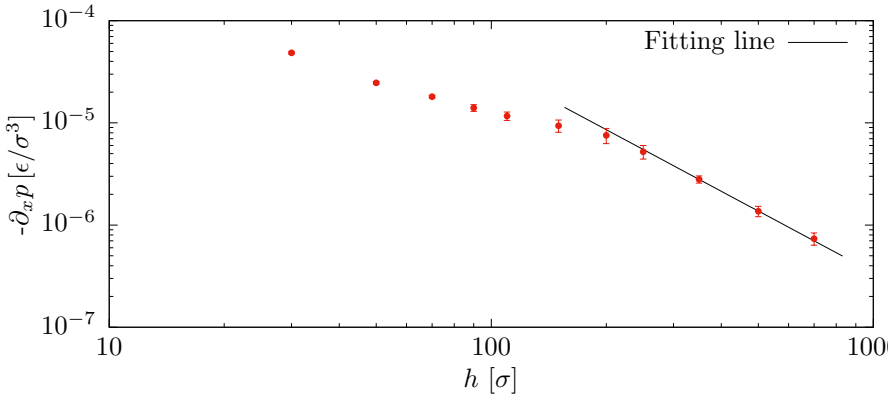

Figure 4.16: Behavior of the bulk pressure gradient (red dots) $\partial_x p$ with the system height h. The black curve represents the fitting line.

leading to a finite value of $v(z)|_{z=\frac{h}{2}}$ according to Equation 4.12.
It is thus possible to give an estimate of a reliable value of $\partial_x p$ in experimental systems. Real systems are three-dimensional while our estimates are based on two-dimensional simulations. On the basis of the simple slab geometry of the problem, we can guess that our scaling holds also in three dimensions and that the quantitative conversion between dimensional quantities can be obtained by use of the natural length unit of the problem: The particle diameter σ. This gives $p_{3D} = p_{2D}/\sigma$. Consequently we can express the bulk pressure gradient in large 3D slits as $\partial_x p = \frac{a}{\sigma h^2}$. Now, considering fluid argon[17] and applying the proper conversion from Lennard-Jones units to real units we can estimate the pressure drop in a wide channel of height h and where the temperature difference between its extremities is ΔT as: $\Delta P \approx 2.8 \times 10^7 \frac{\Delta T}{h^2}$, where pressure is expressed in Pascal, temperature in Kelvin and height in nanometers. This relation suggests that the bulk pressure gradient should be experimentally detectable, even if its magnitude strongly depends on the confining surface.

4.3.2 Asymptotic velocity field

Data in Figure 4.16, together with Equation 4.13, reveal also another important feature of large systems: The asymptotic value of the bulk velocity

[17] Characterized by the following Lennard-Jones parameters: $\sigma = 3.4 \times 10^{-10}$m, $m = 6.69 \times 10^{-26}$kg and $\epsilon = 1.65 \times 10^{-21}$J

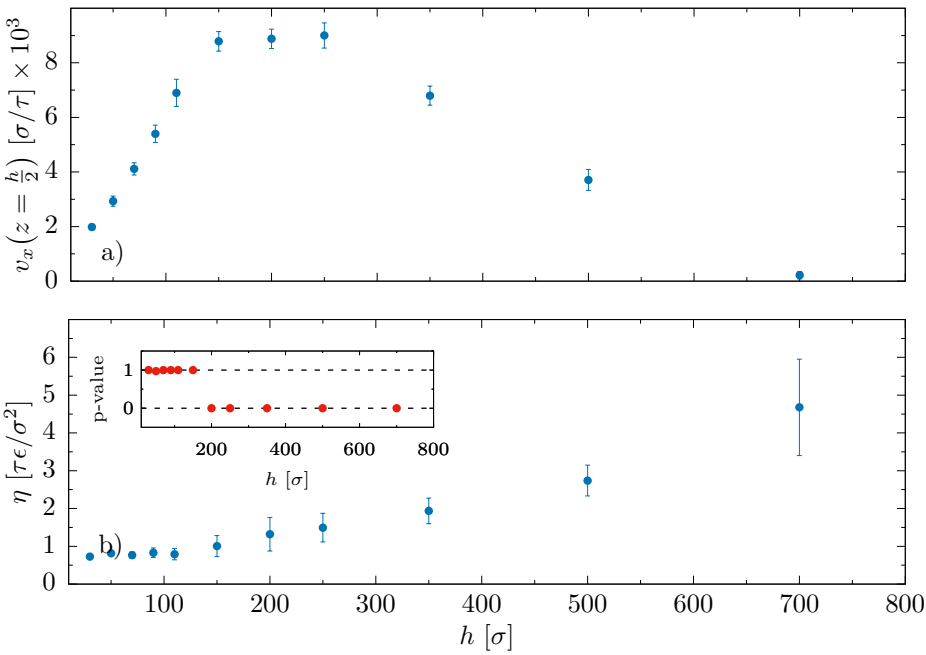

Figure 4.17: a): Behavior of $v(z)|_{z=\frac{h}{2}}$ with h. b): Behavior of viscosity with h; inset: p-value of the corresponding parabolic fits.

$v(z)|_{z=\frac{h}{2}}$ does not depend on h, being

$$\begin{aligned} v(z)|_{z=\frac{h}{2}} &= -\frac{\partial_x p}{24\eta} h^2 \\ &= -\frac{a}{24\eta}\,. \end{aligned} \tag{4.15}$$

Equation 4.15 is useful, because it defines a simple relation between the bulk pressure gradient, in principle experimentally measurable, and the bulk velocity. Prediction of this Equation can be directly verified through the velocity profiles computed in the simulations: For $h \gg \sigma$ the velocity in the center of the channel, $v(z)|_{z=\frac{h}{2}}$, should reach a plateau value at $-a/24\eta$. Note that the bulk viscosity can be directly estimated from a parabolic fit of the velocity profile, according to Poiseuille law.
Unfortunately the expected scaling 4.15 is not observed in the simulations, as shown in panel a of Figure 4.17: In the systems with larger h $v(z)|_{z=\frac{h}{2}}$ decreases with h. The reason of this discrepancy between data and theory can be found in panel b of Figure 4.17, where fluid bulk viscosity η is reported for the different heights. Beeing η a bulk property it should not depend on

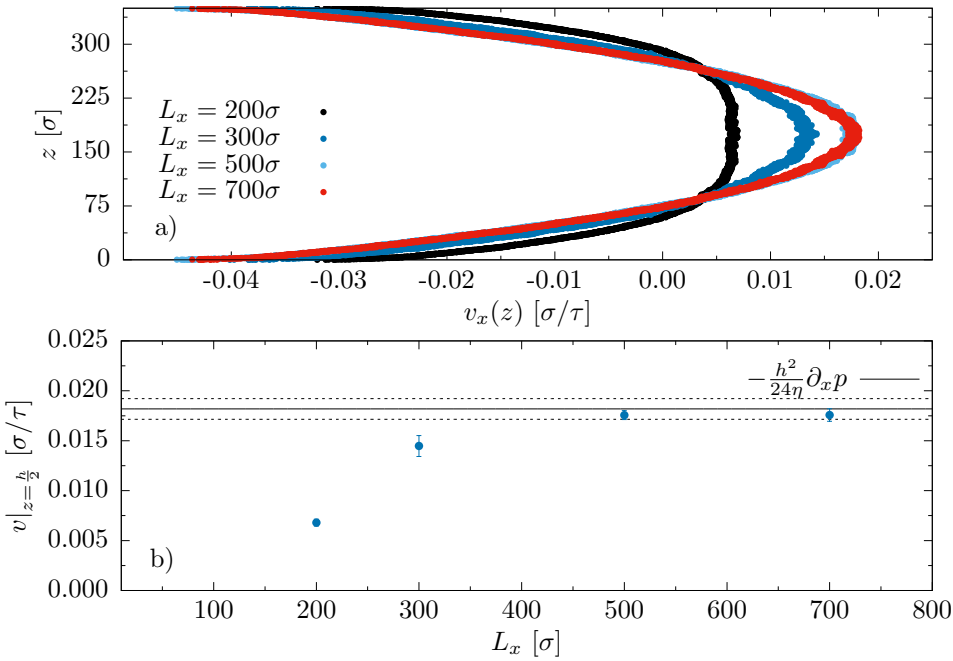

Figure 4.18: a): Velocity profiles for channels of height $h = 350\sigma$ and different lengths L_x. b): Comparison between the prediction of Equation 4.15 and the simulated data reffered to $v(z)|_{z=\frac{h}{2}}$.

the height of the channel[18], but this expectation is confirmed only in the smallest systems. The p-values of the parabolic fits performed to estimate η are reported in the inset of the Figure and it show a sudden drop at $h = 200\sigma$ suggesting that velocity profiles are characterized by a parabolic shape only for the smallest systems, where η results to be independent on h. This means that Poiseuille law is violated for the widest channels, thus it cannot be employed to compute the bulk viscosity.

The physical reason for this occurrence must be sought in the adopted geometry of the system: Data suggest that when the ratio $\frac{h}{L_x} \widetilde{>} 1$ the system length L_x is not big enough to allow a full development of the velocity profile. Consequently the Poiseuille law is no more applicable and the computation of the viscosity through the parabolic fit fails.

The only way to test this hypothesis is simulating systems characterized by the same height but with different lengths L_x and looking at the corresponding velocity profiles. The chosen height is $h = 350\sigma$, being it big enough to guarantee the asymptotic behavior of $\partial_x p$, and four lengths are considered:

[18]To be more precise, being the system closed the viscosity coefficient could in principle acquire some dependence on the height h of the channel, but, according also to results exposed in Chapter 3, we expect this dependence, if existing, to be weak.

$L_x = 200\sigma$, 300σ, 500σ and 700σ. It is important to underline that the resulting bulk pressure gradients are, within the statistical uncertainty, equivalent in these systems. This means that data (and relative considerations) presented in Figure 4.16 are not affected from the value of the ratio $\frac{h}{L_x}$: The bulk pressure gradient scaling law and Equation 4.15 maintain their validity.
The resulting velocity profiles are shown in Figure 4.18, panel a, and the effect of the channel length is clear: Increasing L_x the shapes of the profiles change up to $L_x = 500\sigma$, where the bulk parabolic behavior is recovered and the velocity profiles become independent on the channel length. This change in the velocity profile shapes is reflected also in the value of $v(z)|_{z=\frac{h}{2}}$, as shown in panel b of Figure 4.18: For the two longest channels it can be considered equal and in excellent agreement with the asymptotic value predicted $-a/24\eta$. Note that the value of viscosity obtained by the parabolic fits is $\eta = 0.78554 \pm 0.04448\tau\epsilon/\sigma^2$. It follows that the deviation of data in Figure 4.17 from the plateau value is due only to the the ratio $\frac{h}{L_x}$ and a numerical proof of the validity of Equation 4.15 is provided. Thus, the asymptotic value of the velocity in the center of the channel for this system is equal to $v(z)|_{z=\frac{h}{2}} = 0.01819 \pm 0.00104\sigma/\tau$. We can now express this result in real units referred to argon and, considering a temperature gradient of 100K/cm, we obtain $v(z)|_{z=\frac{h}{2}} \approx 160\mu$m/s.

5

Conclusions and perspectives

Thermo-osmosis has been studied since its discovery in 1873. Despite this, a deep understanding of this phenomenon was lacking, as testified by the discrepancy in its description in gaseous and liquid states. In rarefied fluid kinetic theory was employed, and the particle-surface interaction was recognized as the key point in the development of thermal creep. Instead, thermo-osmosis in liquid state was studied by means of the linear nonequlibrium thermodynamics and the anisotropy of the pressure tensor emerged as the driving force. In Chapter 2 we developed a microscopic theory of this phenomenon, based on the linear response theory generalized to inhomogenous environments. This approach is exact within the limits of validity of linear response theory, i. e. for small gradients in the fields. The emerging scenario results to be quite complex: Two distinct driving mechanisms are recognized, related to both static and dynamic equilibrium properties of the confined fluid. The resulting equations for the velocity field are valid in the whole phase diagram of fluid: Indeed, when the proper approximations are adopted, our approach applied to an infinite open channel is able to reproduce the result obtained by Maxwell [53] for the dilute regime while in the liquid state it leads to an expression for the slip velocity in good agreement with Derjaguin's one [16]. Due to its generality, this description of thermo-osmosis can be generalized to the description of other phenomena where temperature gradients induce particles motion, such as thermophoresis and thermodiffusion.

Moreover, although our expressions contain the tangential pressure near a wall, which is not uniquely defined on microscopic grounds, the physical quantities turn out to be independent of the adopted definition of the pressure

tensor. This feature, absent in the approximate result by Derjaguin, emerges due to the presence of a further contribution which depends on a particular static correlation function. This solves the problem posed in Ref. [32, 33]. This theoretical prediction has been numerically verified through equilibrium molecular dynamics simulations, presented in Chapter 3: We showed that the static source terms computed adopting the Irving-Kirkwood and the Harasima pressure tensors are equal within statistical uncertainty, despite the evident differences between the pressure tensors computed accordingly to the two prescriptions.

In the same Chapter we tackled also the debated question of transport coefficients in two-dimensional systems: Theoretical arguments, developed mainly in the Seventies, suggest that dynamic autocorrelation functions of non-conserved quantity decay in time as t^{-1} and consequently their time integrals, which define the corresponding transport coefficients, diverge. This picture was questioned by a series of numerical works, which showed that, at least in certain thermodynamic conditions and particle-particle interaction potentials, transport coefficients in two-dimensional fluid can be defined through Green-Kubo integrals. We did not attempt to solve this complex question, but just to understand if at least the viscosity coefficient can be defined in Lennard-Jones two-dimensional fluids in the thermodynamic conditions of interest. Therefore, we performed equilibrium molecular dynamics simulations in order to compute the spatially integrated shear component of the pressure tensor dynamic autocorrelation function. Our results rely mainly on the time integral of this quantity and they suggest the existence of the viscosity coefficient in the systems of our interest.

These considerations are important, because due to the emerging complexity of thermo-omosis, we decided to study this phenomenon in Chapter 4 through nonequilibrium molecular dynamics simulations, but, in order to save computational time, we considered two-dimensional fluids. The first nonequilibrium simulations specifically devised to the study thermo-osmosis were performed by Fu *et al.* [29]. They considered a clever three-dimensional geometry in order to simulate an infinite open-channel, computing the mass flow. These simulations were able to check the validity of Derjaguin's expression for the slip velocity and found that some correction should be included in order to take into account hydrodynamic effects induced by the surface. Our simulations were instead performed on closed-channel configurations. In this way the resulting velocity profiles are characterized by a genuine Poiseuille backflow, induced by the bulk pressure gradient originating in the closed channel because of the mass conservation principle. Thus, the closed-channel configuration introduces the physical effect of a bulk pressure gradient, which can be useful in order to devise future experiments of thermo-osmosis, especially in the liquid state. Moreover we examined, by the use of numerical simulations in wide channels, the scaling if the bulk pressure gradient with the width h of the channel: The resulting h^{-2} behavior implies an asymptotic velocity in the middle of the channel independent of h. Note that a channel width of the order of few

hundreds of molecular diameters is enough to reach the asymptotic behavior. In physical units, this correspond to a channel width of the order of tens of nanometers. These results can be also exploited for the implementation of proper boundary conditions in hydrodynamic computations for the study thermo-osmosis in more complex systems.
Beyond the study of this asymptotic behavior, our simulations were devised also in order to verify the relative importance of the two mechanisms emerging from our theory. To this aim, we considered a wide range of fluid densities and temperatures, and a few different confining surfaces. In particular it emerged that, as predicted by our approach, in the rarefied limit it is possible to activate both the static and the dynamic mechanisms according to the properties of the confining surfaces: The first through the presence of an external smooth potential while the second employing diffusive walls and both of them if Einstein walls are considered. Moreover, it is possible also to suppress both of these mechanisms when pure reflective walls are considered. When denser systems are considered, interesting observations can be made. Indeed the static mechanism appears to be quite similar for a reflective and a diffusive wall. Despite this, the bulk pressure gradient and the velocity profiles in the systems with these two kind of confinements are deeply different: This means that the diffusive wall introduces strong dynamic effects also in liquid systems. Moreover, the dynamic mechanism enhances the fluid motion towards the hot side of the channel also in the dense fluid. When systems are confined by a reflective wall plus the repulsive potential the velocity profiles deviate from the Poiseuille parabolic shape only within $z \approx z_r$ far from the surface, being z_r the range of the confining potential. This result strongly suggests that here the static mechanism is predominant, being z_r the relevant length scale in the velocity profile. The effect of the attractive potential at high density is weakened by particles layering, as also happens in systems confined by Einstein walls. In fact particle layering decreases the contribution of the static source term.
Furthermore, the large amount of data allowed to establish an empirical relation between the sign of the thermo-osmotic mass flow and the surface adsorbtion when the static source term dominates: When the confining surface induces a particle depletion, the flow is directed towards the cold side of the system, while it is reversed if particle accumulation takes place. In order to strengthen the reliability of this relation between mass excess and sign of the flow we simulated a rarefied fluid confined by a trap potential. Here the relevant mechanism is the static one, and despite the complex shape of the confining potential the relation between mass adsorption and sign of the flow is still valid.
Finally, the average temperature of the system plays an important role on the effects of the confining potential on the fluid motion: The higher is the temperature, the lower is the effect of the shape of the external potentials, approaching the limiting behavior of the purely reflective wall as the temperature increases. Therefore, we showed that a thermo-osmotic mass flow directed

towards the hot side of the system can be reversed by decreasing the ratio $V(z)/T$.
These numerical results confirm the complexity of thermo-osmosis, but they are also helpful in order to rationalize the role played by the two underlying mechanisms and could be employed as guide to design future experiments on this phenomenon.

Appendix A

ALGORITHM TO COMPUTE CONSERVED QUANTITIES DYNAMIC AUTOCORRELATION FUNCTIONS

In Chapter 3 we presented a general algorithm to numerically compute spatial-integrated dynamic correlation functions $\tilde{\mathcal{C}}$. In particular, if homogeneous systems are considered, it results that

$$\tilde{\mathcal{C}}(t) = \frac{\Delta^4}{A} \left\langle \mathcal{I}_t^1 \, \mathcal{I}^2 \right\rangle_0 , \tag{A.1}$$

being

$$\mathcal{I} = \sum_i \tilde{\mathcal{O}}_i \, . \tag{A.2}$$

Now let us assume that $\tilde{\mathcal{O}}_i^1$ and $\tilde{\mathcal{O}}_i^2$ refer to a globally conserved quantity, such as a particles momentum component in a NVE ensemble, then it immediately follows that

$$\mathcal{I}_t = 0 \tag{A.3}$$

for each t, and so also the corresponding $\tilde{\mathcal{C}}(t)$ is equal to zero. But the spatial-integrated dynamic autocorrelation function $\int \mathrm{d}\boldsymbol{r} \int \mathrm{d}\boldsymbol{r}' \left\langle j^\alpha(\boldsymbol{r}, t) j^\alpha(\boldsymbol{r}') \right\rangle_0$ is not a vanishing quantity: For example, for $t = 0$ it is easy to show that $\frac{1}{A} \int \mathrm{d}\boldsymbol{r} \int \mathrm{d}\boldsymbol{r}' \left\langle j^\alpha(\boldsymbol{r}, t = 0) j^\alpha(\boldsymbol{r}') \right\rangle_0 = \rho/\beta$.
The reason of this discrepancy lies in the fact that dynamical correlation functions are numerically computed in a microcanonical ensemble, so that genuine particles trajectories are tracked, and not in a, for example, canonical one. Thus, in order to obtain the correct result we must find a way to maintain a NVE ensemble but also to break the momentum conservation of the system. These two requirements are contradictory, but we can try to fulfill them dividing the NVE system in Ω subsystems, characterized by the same number of particles randomly chosen: Particles that belong to a given subsystem ω can exchange momentum both with particles of the same subsystem and with the ones of the others $\Omega - 1$. It follows that each subsystem does not conserve the momentum, and so $\mathcal{I}_{t\omega} \neq 0$. Now, we can express the spatial-integrated

dynamic correlation function as

$$\tilde{\mathcal{C}}(t) = \frac{\Delta^4}{A}\left[\sum_{\omega}\langle\mathcal{I}_{\omega}\mathcal{I}_{t\omega}\rangle_0 + \sum_{\omega\neq\gamma}\langle\mathcal{I}_{\omega}\mathcal{I}_{t\gamma}\rangle_0\right] . \tag{A.4}$$

Let us now assume that the self-subsystem contributions are statistically equal, thus

$$\tilde{\mathcal{C}}(t) = \frac{\Delta^4}{A}\left[\Omega\,\langle\mathcal{I}_{\omega}\mathcal{I}_{t\omega}\rangle_0 + \Omega\sum_{\gamma(\neq\omega)}\langle\mathcal{I}_{\omega}\mathcal{I}_{t\gamma}\rangle_0\right] . \tag{A.5}$$

If we assume also that the contributions expressed in the second term are statistically equivalent for every ω and γ, then we can write

$$\tilde{\mathcal{C}}(t) = \frac{\Delta^4}{A}\left[\Omega\,\langle\mathcal{I}_{\omega}\mathcal{I}_{t\omega}\rangle_0 + \Omega\,(\Omega-1)\,\langle\mathcal{I}_{\omega}\mathcal{I}_{t\gamma}\rangle_0\right] , \tag{A.6}$$

with $\omega \neq \gamma$.
It is important to underline that the assumption which leads from Equation A.5 to Equation A.6 is not formally justified. Moreover Ω must be greater than 2, otherwise $\mathcal{I}_{t\gamma} = -\mathcal{I}_{t\omega}$ and so $\tilde{\mathcal{C}} = 0$ for each t.

Appendix B

BUSSI-DONADIO-PARRINELLO THERMOSTAT

The simulation of NVT ensembles requires the control of the temperature of the systems. Rescaling particles velocities is the simplest way to obtain this result, being the temperature a measure of the kinetic energy of the system. Therefore, we can control the temperature simply rescaling, with a given frequency, particles velocities by a factor α

$$\alpha = \sqrt{\frac{\bar{K}}{K}}\,, \tag{B.1}$$

being K the kinetic energy of the system at the considered time step and $\bar{K}$ the desired one.
The authors developed a different way to compute the rescaling factor α, in order to enforce a canonical distribution for the kinetic energy. They do not force the kinetic energy to be exactly equal to $\bar{K}$, instead they select a target value K_t with a stochastic procedure aimed at obtaining the desired NVT ensemble. Thus the velocity-rescaling factor becomes

$$\alpha = \sqrt{\frac{K_t}{K}}\,, \tag{B.2}$$

where K_t could be sampled by the canonical equilibrium distribution for the kinetic energy:

$$\bar{P}(K_t)\mathrm{d}K_t \propto K_t^{\frac{N_f}{2}-1}\mathrm{e}^{\beta K_t}\mathrm{d}K_t\,, \tag{B.3}$$

where N_f are the degrees of freedom of the system. Thus, a simple way to obtain a NVT ensemble would be to extract every M time steps a value of K_t, compute the corresponding factor α and apply it, and then run a NVE dynamics for the following M time steps. In this way the ensemble would be canonical, but this method would disturb considerably the velocities of the particles: Each time the rescaling is applied, the moduli of the velocities will exhibit a fast fluctuation with relative magnitude $1/\sqrt{N_f}$, and so also the particles trajectories would be less genuine in time. Thus the authors developed a smoother approach accordingly to which the value K_t is not randomly chosen by the distribution expressed in Equation B.3, but instead it

is based on the previous value of K: At each time step an auxiliary continuous stochastic dynamics is considered to compute the value of K_t, assuming K as initial condition. This value of K_t is then used to compute α and particles velocities are rescaled. The choice of the stochastic dynamics has some degree of arbitrariness, the only constraint being that it has to leave the canonical distribution in Equation B.3 invariant. Thanks to the Fokker-Planck equation it is possible to express this auxiliary continuous stochastic dynamics as

$$\mathrm{d}K = (\bar{K} - K)\frac{\mathrm{d}t}{\tau} + 2\sqrt{\frac{K\bar{K}}{N_f}}\frac{\mathrm{d}W}{\sqrt{\tau}}\,, \tag{B.4}$$

where τ is an arbitrary parameter which determines the time scale of the thermostat and $\mathrm{d}W$ is a Wiener noise.
Thus this thermostat samples the canonical ensemble and, thanks to its elaborate method to compute α, the particles trajectories are not heavily influenced by the temperature control.
More details can be found in Ref. [11].

Note that this thermostat does not perform a time integration but only modifies velocities. Instead, in our simulations a NVE dynamics is achieved through the velocity-Verlet integrator [81].

References

[1] Alder, B. J., and Wainwright, T. E. Decay of the Velocity Autocorrelation Function. *Physical Review Letters 18* (1967), 988.

[2] Alder, B. J., and Wainwright, T. E. Decay of the Velocity Autocorrelation Function. *Physical Review A 1* (1970), 18.

[3] Aubert, M. Thermo-osmose. *Annales de chimie et de physique 26* (1912), 145.

[4] Balescu, R. *Equilibrium and nonequilibrium statistical mechanics*. John Wiley & Sons, 1975.

[5] Barragán, V. M., and Kjelstrup, S. Thermo-osmosis in Membrane Systems: A Review. *Journal of Non-Equilibrium Thermodynamics 42* (2017), 217.

[6] Bauss, M., and Lovett, R. *Physical Review Letters 65* (1990), 1781.

[7] Bauss, M., and Lovett, R. *Physical Review A 44* (1991), 1211.

[8] Bond, S. D., and Leimkuhler, B. J. Stabilized Integration of Hamiltonian Systems with Hard-Sphere Inequality Constraints. *SIAM Journal on Scientific Computing 30* (2007), 134–147.

[9] Bregulla, A. P., Würger, A., Günther, K., Mertig, M., and Cichos, F. Thermo-Osmotic Flow in Thin Films. *Physical Review Letters 116* (2016), 188303.

[10] Brush, S. G., and Everitt, C. W. F. Maxwell, Osborne Reynolds, and the Radiometer. *Historical Studies in the Physical Sciences 1* (1969), 105–125.

[11] Bussi, G., Donadio, D., and Parrinello, M. Canonical sampling through velocity rescaling. *Journal of Chemical Physics 126* (2007), 014110.

[12] Chrétien, D., Bénit, P., Ha, H.-H., Keipert, S., El-Khoury, R., Chang, Y.-T., Jastroch, M., Jacobs, H. T., Rustin, P., and Rak, M. Mitochondria are physiologically maintained at close to 50 C. *PLOS Biology 16* (2018), 1–17.

[13] Crookes, W. XIII. On repulsion resulting from radiation. Parts III. & IV. *Philosophical Transactions of the Royal Society of London 166* (1876), 325–376.

[14] Cuche, A., Canaguier-Durand, A., Devaux, E., Hutchison, J. A., Genet, C., and Ebbesen, T. W. Sorting Nanoparticles with Intertwined Plasmonic and Thermo-Hydrodynamical Forces. *Nano Letters 13* (2013), 4230–4235.

[15] Derjaguin, B. V., Churaev, N. V., and Muller, V. M. *Surface Forces in Transport Phenomena*. Springer, Boston, 1987.

[16] Derjaguin, B. V., and Sidorenkov, G. P. Thermoosmosis at ordinary temperatures and its analogy with the thermomechanical effect in helium II. *Doklady Akademii Nauk SSSR 32* (1941), 622–626.

[17] Donkò, Z., Goree, J., Hartmann, P., and Liu, B. Time-correlation functions and transport coefficients of two-dimensional Yukawa liquids. *Physical Review E 79* (2009), 026401.

[18] Dorfman, J. R., and Cohen, E. G. D. Velocity-Correlation Function in Two and Three Dimensions: Low Density. *Physical Review A 6* (1972), 776.

[19] Dufour, L. *Archives des Sciences physiques et naturelles, Genève 45* (1872), 9–12.

[20] Dufour, L. Ueber die Diffusion der Gase durch poröse Wände und die sie begleitenden Temperaturveränderungen. *Annalen der Physik 224* (1873), 490–492.

[21] Ercole, L., Marcolongo, A., Umari, P., and Baroni, S. *Journal of Low Temperature Physics 185* (2016), 79.

[22] Ernst, M. H., Hauge, E. H., and van Leeuwen, J. M. J. Asymptotic Time Behavior of Correlation Functions. *Physical Review Letters 25* (1970), 1254.

[23] Evans, D. J., and Morris, G. P. Nonequilibrium Molecular-Dynamics Simulation of Couette Flow in Two-Dimensional Fluids. *Physical Review Letters 19* (1983), 1776.

[24] Evans, R., and Parry, A. O. Liquids at interfaces: what can a theorist contribute? *Journal of Physics: Condensed Matter 2* (1990), 15–32.

[25] Farago, O. A simple statistical-mechanical interpretation of Onsager reciprocal relations and Derjaguin theory of thermo-osmosis. *The European Physical Journal E 42* (2019), 136.

[26] Feddersen, W. V. On thermodiffusion of gases. *Philosophical Magazine Series 5 46* (1873), 55–62.

[27] Feng, Y., Goree, J., and Liu, B. Longitudinal viscosity of two-dimensional Yukawa liquids. *Physical Review E 87* (2013), 013106.

[28] Ferrario, M., Fiorino, A., and G., C. Long-time tails in two-dimensional fluids by molecular dynamics. *Physica A 240* (1997), 268–276.

[29] Fu, L., Merabia, S., and Joly, L. What Controls Thermo-osmosis? Molecular Simulations Show the Critical Role of Interfacial Hydrodynamics. *Physical Review Letters 119* (2017), 214501.

[30] Fu, L., Merabia, S., and Joly, L. Understanding Fast and Robust Thermo-Osmotic Flows through Carbon Nanotube Membranes: Thermodynamics Meets Hydrodynamics. *The Journal of Physical Chemistry Letters 9* (2018), 2086–2092.

[31] Galliéro, G., Colombani, J., Duguay, B., Caltagirone, J. P., and Montel, F. Evaluation de la thermodiffusion en milieu poreux nanométrique intégré par dynamique moléculaire hors équilibre directe. *Entropie* (2002), 98–102.

[32] Ganti, R., Liu, Y., and Frenkel, D. Molecular Simulation of Thermo-osmotic Slip. *Physical Review Letters 119* (2017), 038002.

[33] Ganti, R., Liu, Y., and Frenkel, D. Hamiltonian Transformation to Compute Thermo-osmotic Forces. *Physical Review Letters 121* (2018), 068002.

[34] Gravina, D., Ciccotti, G., and L., H. B. Linear and nonlinear viscous flow in two-dimensional fluids. *Physical Review E 52* (1995), 6123.

[35] Haase, R., and Steinert, C. Thermoosmose in Flüssigkeiten. *Zeitschrift für Physikalische Chemie 21* (1959), 570.

[36] Hansen, Jean-Pierre and McDonald, Ian R. *Theory of Simple Liquids*, fourth ed. Academic Press, 2013.

[37] Haralson, Z., and Goree, J. Overestimation of Viscosity by the Green-Kubo Method in a Dusty Plasma Experiment. *Physical Review Letters 118* (2017), 195001.

[38] Harasima, A. Molecular Theory of Surface Tension. *Advances in Chemical Physics 1* (1958), 203–237.

[39] Hood, L. M., Evans, D. J., and Cui, S. T. Number Dependence of Viscosity in Two Dimensional Fluids. *Molecular Simulation 9* (1992), 307–310.

[40] Hoover, G. W., and Posch, H. A. Shear viscosity via global control of spatiotemporal chaos in two-dimensional isoenergetic dense fluids. *Physical Review E 51* (1995), 273.

[41] Hutchison, H. P., Nixon, I. S., and Denbigh, K. G. The thermo-osmosis of liquids through porous materials. *Discussions of the Faraday Society 3* (1948), 86.

[42] Irving, J. H., and Kirkwood, J. G. The Statistical Mechanical Theory of Transport Processes. IV. The Equations of Hydrodynamics. *The Journal of Chemical Physics 18* (1950), 817–829.

[43] Isobe, M. Long-time tail of the velocity autocorrelation function in a two-dimensional moderately dense hard-disk fluid. *Physical Review E 77* (2008), 021201.

[44] Kennard, E. *Kinetic theory of gases: with an introduction to statistical mechanics*. McGraw-Hill, 1938.

[45] Kirkwood, J. G., and Buff, F. P. The Statistical Mechanical Theory of Surface Tension. *The Journal of Chemical Physics 17* (1949), 338–343.

[46] Landau, L., and G., P. *Physik Z. Sowjetunion 5* (1934), 172.

[47] Landau, L., and Lifshitz, E. *Fluid Mechanics*, second ed. Pergamon, 1987.

[48] Lee, J., Laoui, T., and Karnik, R. Nanofluidic transport governed by the liquid/vapour interface. *Nature Nanotechnology 9* (2014).

[49] Lippmann, G. Endosmose entre deux liquides de même composition chimique et de températures différentes. *Comptes rendus de l'Académie des sciences 145* (1907), 104–105.

[50] Liu, B., and Goree, J. Shear Viscosity of Two-Dimensional Yukawa System in the Liquid State. *Physical Review Letters 94* (2005), 185002.

[51] Logan, B. E., and Elimelech, M. Membrane-based processes for sustainable power generation using water. *Nature 488* (2012), 313–319.

[52] Ludwig, C. *Diffusion zwischen ungleich erwärmten Orten gleich zusammengesetzter Lösung*. 1856.

[53] Maxwell, J. C. VII. On stresses in rarified gases arising from inequalities of temperature. *Philosophical Transactions of the Royal Society of London 170* (1879), 231–256.

[54] Mori, H. A Quantum-statistical Theory of Transport Processes. *Journal of the Physical Society of Japan 11* (1956), 1029–1044.

[55] Mori, H. Statistical-Mechanical Theory of Transport in Fluids. *Physical Review 112* (1958), 1829–1842.

[56] Morris, G. P., and Evans, D. J. Viscoelasticity in two dimensions. *Physical Review A 32* (1985), 2425.

[57] Nosenko, V., and Goree, J. Shear Flows and Shear Viscosity in a Two-Dimensional Yukawa System (Dusty Plasmas). *Physical Review Letters 93* (2004), 155004.

[58] Ono, S. and Kondo, S. *Structure of Liquids.* Springer, 1960.

[59] Onsager, L. Reciprocal Relations in Irreversible Processes. I. *Physical Review 37* (1931), 405–426.

[60] Pagliuca, N., Bencivenga, U., Mita, D. G., Perna, G., and Gaeta, F. Isothermal and non-isothermal water transport in porous membranes. II. the steady state. *Jornal of Membranes Science 33* (1987), 1–25.

[61] Pagliuca, N., Mita, D. G., and Gaeta, F. Isothermal and non-isothermal water transport in porous membranes. I. the power balance. *Jornal of Membranes Science 14* (1983), 31–57.

[62] Papadopoulos, D. H., and Rosner, D. E. Enclosure gas flows driven by non-isothermal walls. *Physics of Fluids 7* (1995), 2335.

[63] Parola, A., and Piazza, R. Particle thermophoresis in liquids. *The European Physical Journal E 15* (2004), 255–263.

[64] Piazza, R., and Parola, A. Thermophoresis in colloidal suspensions. *Journal of Physics: Condensed Matter 20* (2008), 153102.

[65] Plimpton, S. Fast Parallel Algorithms for Short-Range Molecular Dynamics. *Journal of Computational Physics 117* (1995), 1–19.

[66] Pomeau, Y. Low-Frequency Behavior of Transport Coefficients in Fluids. *Physical Review A 5* (1972), 2569.

[67] Proesmans, K., and Frenkel, D. Comparing theory and simulation for thermo-osmosis. *The Journal of Chemical Physics 151* (2019), 124109.

[68] Rowlinson, J. S. *Physical Review A 67* (1991), 406.

[69] Rowlinson, J. S. Thermodynamics of inhomogeneous systems. *The Journal of Chemical Thermodynamics 25* (1993), 449–461.

[70] Schofield, P., and Henderson, J. R. Statistical Mechanics of Inhomogeneous Fluids. *Proceedings of the Royal Society of London A: Mathematical, Physical and Engineering Sciences 379* (1982), 231–246.

[71] Schuster, A. II. On the nature of the force producing the motion of a body exposed to rays of heat and light. *Proceedings of the Royal Society of London 24* (1876), 391–392.

[72] Smit, B., and Frenkel, D. Vapor-liquid equilibria of the two-dimensional Lennard-Jones fluid(s). *Journal of Chemical Physics 94*.

[73] Sone, Y. Flows Induced by Temperature Fields in a Rarefied Gas and their Ghost Effect on the Behavior of a Gas in the Continuum Limit. *Annual Review of Fluid Mechanics 32* (2000), 779–811.

[74] Sone, Y., and Yoshimoto, M. Demonstration of a rarefied gas flow induced near the edge of a uniformly heated plate. *Physics of Fluids 9* (1997), 3530–3534.

[75] Soret, C. Sur l'état d'équilibre que prend au point de vue de sa concentration une dissolution saline primitivement homohéne dont deux parties sont portées à des températures différentes. *Archives des Sciences physiques et naturelles, Genève 2* (1879), 48–64.

[76] Soret, C. Influence de la température sur la distribution des sels dans leurs solutions. *Comptes Rendus Hebdomadaires des Séances de l'Académie des Sciences 91* (1880), 289–291.

[77] Soret, C. Sur l'état d'équilibre que prend au point de vue de sa concentration une dissolution saline primitivement homohéne dont deux parties sont portées à des températures différentes. *Annales de Chimie et de Physique 22* (1881), 293–297.

[78] Suh, S. H., and MacElroy, J. "Molecular dynamics simulation of hindered diffusion in microcapillaries. *Molecular Physics* (1986), 445–473.

[79] Tyndall, J. On Haze and Dust. *Nature 1* (1870).

[80] Vanossi, A., Manini, N., Urbakh, M., Zapperi, S., and Tosatti, E. Colloquium: Modeling friction: From nanoscale to mesoscale. *Review of Modern Physics 85* (Apr 2013), 529–552.

[81] Verlet, L. Computer "Experiments" on Classical Fluids. I. Thermodynamical Properties of Lennard-Jones Molecules. *Physical Review 159* (1967), 98–103.

[82] Wold, I., and Hafskjold, B. Nonequilibrium Molecular Dynamics Simulations of Coupled Heat and Mass Transport in Binary Fluid Mixtures in Pores. *International Journal of Thermophysics 20* (1999), 847.

[83] Würger, A. Thermal non-equilibrium transport in colloids. *Reports on Progress in Physics* (2010), 126601.

[84] Zheng, F. Thermophoresis of spherical and non-spherical particles: a review of theories and experiments. *Advances in Colloid and Interface Science 97* (2002), 255 – 278.